Microscale CFD Evaluation of PCS Impacts on Air Quality
Deliverable 6.2 iSCAPE project

iSCAPE

Microscale CFD Evaluation of PCS Impacts on Air Quality

D6.2

February 2019

This project has received funding from the European Union's Horizon 2020 research and innovation programme under grant agreement No 689954.

Project Acronym and Name	iSCAPE - Improving the Smart Control of Air Pollution in Europe	
Grant Agreement Number	689954	
Document Type	Report	
Document version & WP No.	V0.3	WP6
Document Title	Microscale CFD Evaluation of PCS Impacts on Air Quality	
Main authors	Abhijith Kooloth Valappil, Hamid Omidvarborna, Thor-Bjørn Ottosen, Sachit Mahajan, Prashant Kumar (UoS), John Gallagher, Bidroha Basu, Francesco Pilla, Aonghus McNabola, Brian Broderick (TCD), Beatrice Pulvirenti, Silvana Di Sabatino, Federico Prandini, Sara Baldazzi, Erika Brattich, Francesco Barbano (UNIBO), Achim Drebs (FMI)	
Partner in charge	University of Surrey (UoS)	
Contributing partners	University of Bologna (UNIBO), University College Dublin (UCD), University of Surrey (UoS)	
Release date	February 2019	

Document Control Page			
Short Description	*The purpose of this report is to document findings from CFD simulation studies on the detailed effects of selected PCSs on neighborhood air quality in three different iSCAPE cities (Bologna, Dublin and Guildford). This deliverable is an output of Task 6.2 of the iSCAPE project.*		
Review status	**Action**	**Person**	**Date**
	Quality Check	*Coordination Team*	
	Internal Review	*Muhammad Adnan* *Jörg Peter Schmitt*	21 Feb 2019
Distribution	Public		

Revision history			
Version	**Date**	**Modified by**	**Comments**
V0.1	12-02-2019	Abhijith Kooloth Valappil, Hamid Omidvarborna, Thor-Bjørn Ottosen, Sachit Mahajan, Prashant Kumar (UoS), John Gallagher, Bidroha Basu, Francesco Pilla, Aonghus McNabola, Brian Broderick (TCD), Beatrice Pulvirenti, Silvana Di Sabatino, Federico Prandini, Sara Baldazzi, Erika Brattich, Francesco Barbano (UNIBO)	Draft version, submitted for review
V0.2	20-02-2019	Muhammad Adnan Jörg Peter Schmitt	Received the internal reviewers' comments.
V0.3	25-02-2019	Abhijith K.V., Hamid Omidvarborna, Bidroha Basu, Beatrice Pulvirenti, Silvana Di Sabatino, Erika Brattich	Addressing the reviewers' comments.

Statement of originality:

This deliverable contains original unpublished work except where clearly indicated otherwise. Acknowledgement of previously published material and of the work of others has been made through appropriate citation, quotation or both.

Table of Contents

List of Tables

List of Figures

List of Abbreviations

ARPAE	Emilia Romagna Environmental Protection Agency
BTEX	Benzene, Toluene, Ethylbenzene and Xylene
CFD	Computational Fluid Dynamics
CO	Carbon Monoxide
CO_2	Carbon Dioxide
DCC	Dublin City Council
EEA	European Environment Agency
EMEP	European Monitoring and Evaluation Programme
ER	Emissions Rate
GI	Green Infrastructure
GIS	Geographical Information System
I/O	Inlet/Outlet
IR	Infrared
iSCAPE	Improving the Smart Control of Air Pollution in Europe
ISL	Inertial Sub-Layer
LAD	Leaf Area Density
LAI	Leaf Area Index
LBW	Low Boundary Wall
LES	Large Eddy Simulation
NO	Nitrogen Monoxide
NO_x	Nitrogen oxides
O_3	Ozone
PM	Particulate Matter
PCS	Passive Control Solution
RANS	Reynolds-averaged Navier-Stokes
SCATS	Sydney Coordinated Adaptive Traffic System
SIMPLE	Semi-Implicit Method for Pressure Linked Equation
TI	Traffic Intersection
TKE	Turbulent Kinetic Energy
UCL	Urban Canopy Layer
UDF	User-Defined Function
UHI	Urban Heat Island

UTC	Coordinated Universal Time
WMO	World Meteorological Organization
WP	Work Package

Executive Summary

Air pollution continues to be a global concern among the scientific communities due to its impacts on human health, the environment and climate change. Due to the specific urban landscape and climatic characteristics in European cities, passive control solution (PCS) has been selected for analysis by Improving the Smart Control of Air Pollution in Europe (iSCAPE) project. PCSs include low boundary walls (LBWs), trees and hedges, green walls and green roofs, photocatalytic coatings, green urban spaces and road geometry interventions. The effect of trees, green roofs and green façades in the real urban environment on pollutant concentration at street level has been carried out in Bologna. The Guildford living lab focuses on hedges in open-road environments unlike other cites simulating street canyon conditions. The Dublin study focused on determining the effectiveness of LBW passive control structure to reduce personal exposure to vehicular pollutants. The iSCAPE project aims at altering the dispersion mechanism, enhancing the deposition process and chemically breaking down the air pollutants in order to reduce their concentration levels at target receptors by using PCSs. Although practical implementation of PCSs needs to be supported financially, the application of inexpensive tools, such as computer programming is always demanded.

A detailed analysis of two street canyons (with and without trees) in Bologna has been considered in two days cycles, covering the summer and winter seasons. The results show that planting trees within street canyons without trees (aspect ratio > 1 and traffic intersections) give more uniform distribution, but pollutant concentration levels could be higher than expected in some zones. On the contrary, non-uniform distribution in space pollutant concentrations, especially near the intersections within street canyons without trees have been observed. Additionally, the application of green roofs and green façades modifies the flow field at street level and the pollutant near the building walls. The study in Guilford showed that the hedges along the street work as a barrier for the pedestrians as validated by the experimental results. The hedge grows increases wind speed at the breathing level (1-2 meters) forcing pollutants to move along the road. The calibrated CFD model for wind speed/direction and NO emission in Dublin was used to determine the effect of implementing a LBW in pollutant concentrations on the footpaths. The model included LBWs along both sides of the canyon with gaps for road junctions and bus stops. Both reduction and increase in pollutant concentrations on the footpaths in parallel and perpendicular wind models have been reported.

The purpose of this deliverable (D6.2) is to document findings from simulation studies on the detail effects of PCSs on neighbourhood air quality in three different iSCAPE cities (Bologna, Guildford and Dublin). The development and testing of new PCSs and their effects on local air pollution and climate have been assessed through the computational fluid dynamic (CFD) simulations (task 6.2 of the work package, WP, number 6). Field measurement data collected as a part of the iSCAPE project (WP5) is used for validation of the model simulations. The output of this deliverable addresses simulating effects of infrastructural solutions on air quality at neighbourhood levels that are discussed in WP6.2.

1 Introduction

This section defines the background and contextual information under which task 6.2 of the iSCAPE project is found out within the objective of WP6. D6.2 is paired with monitoring campaigns at the test sites (WP5). The methodological frameworks outlined for achieving the objectives of iSCAPE project in the WP6 are:

- To quantify the effects of the infrastructural PCSs in terms of air pollutant levels and climate change using the most up-to-date numerical approach.
- To evaluate the efficacy of PCS interventions in target cities in the mid/long term. To support numerical simulation requirements to assist other WPs requirement (e.g. WP3 and WP4).

This deliverable assesses the benefits in terms of air pollution and climate variables resulting from the deployment of PCSs interventions through microscale CFD simulation. The outcome of D6.2 (task 6.2) will be also fed to task 6.3 by investigating the effect of proposed infrastructure solution at city scale on both air quality and urban heat island (UHI).

Protecting human health and the environment from air pollution still remains a challenge and requires a comprehensive understanding of meteorological factors as well as pollutant transport (Gallagher et al., 2015). Due to urbanization and population growth in recent years, implementation of PCS methods has been suggested to alter regular dispersion patterns and to mitigate air pollution in the built environment (McNabola, 2010). PCSs include trees, hedges and vegetation, green walls and green urban spaces, which reduce personal exposure by changing air flow patterns. Changes in the concentration of air pollutants in the presence of PCS (urban vegetation) were reviewed by Janhäll (2015). The study revealed the importance of urban vegetation in the improvement of ambient air quality. It also highlighted that adding large trees in trafficked street canyons increases concentration levels of local air pollutants, while a relatively dense and/or porous vegetation close to sources can improve air quality by enhancing deposition. More recently, Abhijith and Kumar (2019) evaluated different green infrastructure (GI) types (hedges, trees, and a combination of hedges and trees) in close-road and away-road environments and under along-road (parallel to the road), cross-road (perpendicular to the road, from the road to GI) and cross-vegetation (opposite to cross-road) wind conditions. As shown in Fig. 1, the use of hedges or a combination of hedges/trees, therefore, emerged as favourable options for the reduction of pollutant concentrations behind vegetation (Abhijith and Kumar, 2019).

Evaluation of PCS methods through experimental and numerical studies have demonstrated the complexities of the system (Gallagher et al., 2015). For example, a set of modelling studies has been carried out showing the impact of PCSs on the dispersion of air pollutants mainly from traffic sources (McNabola et al., 2009; Gallagher et al., 2011; Gallagher et al., 2012). McNabola et al. (2009) implemented CFD models to understand the impact of Low Boundary Wall (LBW) on the dispersion of air pollutants in street canyons. The study showed that the presence of LBWs at the urban street canyons could reduce the pedestrian exposure by up to 40% (perpendicular wind directions) and up to 75% (parallel wind directions). The magnitude of the exposure reduction was a function of street geometry, location of walls, location of traffic emissions, wind speed and wind direction. To investigate the effectiveness of parked cars in urban street canyons, a numerical model by Gallagher et al. (2011) showed 35% and 49% reduction in human exposure to air pollutants in perpendicular wind conditions on the leeward and windward footpaths, respectively. In the case of parallel winds and parallel parking, 33% pollutant reduction on both

leeward and windward footpaths was observed. In similar numerical studies, the potential of LBWs (Gallagher et al., 2012; Wang et al., 2017), parked cars (Gallagher and Lago, 2019), and roadside hedges (Gromke et al., 2016) as PCSs in personal exposure reduction were further elaborated. A CFD simulation study (considering trees and parked cars as PCSs) in a street canyon was carried out by Abhijith and Gokhale (2015). Different configurations of both trees and parked cars were considered. In terms of various combinations, high porosity and low stand density, medium-sized trees with parallel and perpendicular orientation of car parking systems resulted in the best PCS approach for the reduction of human exposure. In summary, the outcome of these numerical studies highlighted the potential benefits of CFD to predict the amount of exposure individuals are receiving.

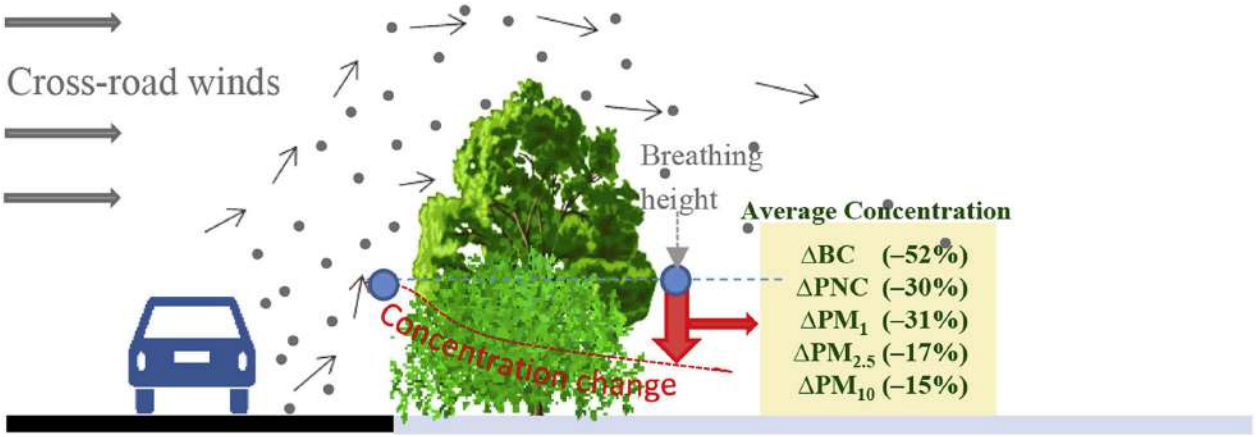

Figure 1: Percentage reduction in pollutant concentrations by using PCSs (Abhijith and Kumar, 2019).

The review of previous studies emphasised that although different PCS measurements and/or modelling approaches have been adopted, the evaluation of PCS impacts on air quality is not well investigated. There are different PCS configurations that can be examined and validated through various CFD modelling approaches. In addition, the effectiveness of the PCS methods in alternating the air pollution dispersion mechanism in the built environment depends on both local geometrical and meteorological conditions (Kumar et al., 2014, Kumar et al., 2015). Therefore, detailed studies on the application of different PCS methods should be conducted to validate the modelling outcomes with the real measurement data (WP5).

D6.2 focuses on high resolution modelling using a CFD type of approach. The CFD study can be performed with Fluent and Open Foam or similar well-recognised CFD codes. Specifically, this deliverable emphasis on the effect of incoming flow conditions (wind speed, direction and turbulence levels) and solar radiation on the streets. Hence, several infrastructural options are investigated to comprehend their effects on the heat-exchange, the mass transfer (oxygen, carbon dioxide or CO_2 and humidity) and/or ventilation. Major emissions and meteorological data have been used as input for the CFD modelling. The numerical results are validated with measured data obtained from WP5. In addition, the effect of PCSs on local air quality prior and after interventions have been considered by creating hypothetical scenarios. Further, the effect of vegetation, green roofs, green walls and photocatalytic coatings in specific neighbourhoods in the cities have been assessed.

Following Table provides an overview of the different CFD simulations performed in the four iSCAPE cities and presented in the rest of the report.

City	Type of PCS/intervention	Research objectives
Bologna	Trees	Identify the key mechanism of ventilation in street canyons with real morphology and real environmental conditions; Effects of trees on ventilation and thermal comfort in urban street canyons
Bologna	Green roofs and green facades	Effects of green roofs on ventilation and pollutant distribution in the street canyons
Dublin	LBWs	Effects of LBW on ventilation in urban street canyons
Guildford	Different hedges and trees	Effects of GI on ventilation in urban street canyons

Table 1: Overview of CFD numerical simulations carried out within Task 6.2 of the iSCAPE project and presented in this report.

Depending upon the field campaigns investigating various PCS (as a part of D5.2 Air pollution and meteorology report), trees, green roofs, green walls and photocatalytic coatings in street canyon environment are studied by UNiBO, hedges in open-road conditions by UoS, and UCD modelled LBW. The output of this deliverable will be used as a showcase, which will provide a set of recommendations for other city's neighbourhoods as well. Moreover, alternative scenarios will also be made in order to gather a comprehensive overview of the possible mitigation solutions.

In this report, the effects of various atmospheric stratification conditions on specific targets have been addressed by several simulations. This deliverable will furnish the science-based assessment of the PCSs. The output of D6.2 as well as the recommendations drawn from the analysed data will be used as a showcase of the project and will be put into context for other cities' neighbourhood. In addition, the outputs will be used for WP7 and WP8 to formulate solid policy options for future interventions in the reduction of air pollution in European cities.

2 Methodology

Field measurement campaigns assessing effectiveness of various PCS were conducted as a part of deliverable D5.2 in some pilot cities, namely Bologna, Dublin and Guildford. In particular, while the impact of some PCSs in street canyon environments was investigated by UNIBO and UCD, UoS investigated instead open road environments. Specifically, the modifications on ventilation and resulting air quality concentrations induced by the presence of trees, green roofs, green walls and photocatalytic coatings in street canyon environment was studied by UNIBO. On the other hand, monitoring campaigns at UCD focused on LBW in a typical street canyon. Finally, UoS investigated air pollution modification of hedges in open road environments. The following sections provide details of these measurement campaign and the details of numerical set up and simulation methodology adopted by each living lab.

2.1 Bologna

The Bologna Living Lab focuses on GI in urban street canyons. An urban street canyon is a place where the street is flanked by buildings on both sides creating a canyon-like experiment. In general, the most important geometrical detail about a street canyon is the ratio of the canyon height (H) to canyon width (W), H/W, defined as the aspect ratio. The effect of a street canyon on local ventilation and resulting air quality can greatly differ in different canyon geometries.

As a part of D3.3 ('*Report on footprint of Passive Control Systems*'[1]) and D5.2 ('*Air quality and meteorology monitoring report*'[2]), the instrumental setup of the intensive field campaigns conducted in two parallel urban street canyons in Bologna in summer 2017 and winter 2018 to analyse the effect of trees on ventilation and air quality was presented. The outcomes of this experimental study were submitted as a part of D5.2 while recent findings will be included in the updated version of D5.2.

In the following, we present the results of microscale CFD simulations conducted in the two neighbourhoods investigated within the two intensive field campaigns.

2.1.1 Site description

The computational study of the effect of PCSs on pollutant concentration at street level in Bologna has been focused on the study of the influence of trees in the real urban environment, by studying two neighbourhood areas around two street canyons, one without trees (Marconi street canyon) and one with trees (Laura Bassi street canyon). As reported in D3.3 ('*Report on footprint of PCS*') and D5.2 ('*Air pollution and meteorology report*'), two intensive experimental campaigns were carried out in those two street canyons, with the objective to evaluate the effectiveness of trees in modifying flow dispersion impacting on air pollution, and in ameliorating the urban thermal comfort.

[1] Report on footprint of passive control systems
[2] The report will be published in the iSCAPE results webpage.

Figure 2: Overview of Bologna city centre.

Furthermore, the effect of photocatalytic paintings and green walls have also been investigated. As reported in D3.8 ('Report on neighbourhood level interventions'), in this case, a neighbourhood area in Bologna, the "Lazzaretto" campus of the University of Bologna, chosen to conduct an intensive experimental campaign to analyse the effectiveness of street canyons in real street canyons. In this report, simulation results obtained in the area of the intervention in a scenario where green roofs were implemented are detailed, while results of CFD modelling with photocatalytic coatings are reported extensively in D3.6 ('Report on photocatalytic coating'). In this section, the three neighbourhoods areas chosen for the CFD modelling of the various PCSs simulated in Bologna are described.

Marconi street – No trees street canyon

As reported in D3.3 and D5.2, Marconi street is an affluent inner-city area of central Bologna (Italy), located within the city center. In this area, there are a few major streets (Marconi street, Riva Reno street, Ugo Bassi street), with smaller alleys between the major streets. Marconi street is characterized by a high packing density of the buildings (Kanda, 2006) and has a street canyon configuration with an aspect ratio H/W=1.65 (Fig. 2). It is one of the most polluted sites in the town, with an average NO2 concentration of 94 μg m^{-3} in 2014, according to the ARPAE (Emilia Romagna Environmental Protection Agency) measurements (as from the urban air quality station located in San Felice street). An overview of the study area is shown in Fig. 3. Marconi street is a four lanes limited traffic car zone, characterized by a considerable transit of buses (almost all bus lanes pass from this street). It is characterized by the presence of portici (arcades), which are not modelled in these simulations, and therefore also by high pedestrian traffic. Marconi street is almost completely free from trees and GIs, apart from the first part of the street. The street orientation compared to North-South direction is 20°. Riva di Reno street, in East-West direction in Fig. 3, is a two lanes road characterized by intense cars and buses traffic (Prandini et al., 2018).

Figure 3: Overview of Marconi street and surrounding area (left) and Marconi street canyon view (right).

Laura Bassi street – Street canyon with trees

Laura Bassi Veratti (from now on referred as Laura Bassi) street is an affluent in the neighbour of the city, located outside the city center. It is characterized by a few major streets (Emilia Ponente street, Mezzofanti street, Murri street), with smaller alleys between the major streets. Laura Bassi street has a canyon configuration with an aspect ratio H/W=0.7. An overview of the study area is shown in Fig. 4. Laura Bassi street is in a residential zone with a low packing building density, due to the presence of terraced houses with a private garden. For this reason, this area has a high density of trees (Fig. 5). The street is characterized by car and bike traffic and lower bus traffic than Marconi street. The street orientation compared to the North-South coordinate is 25°.

As shown in Fig. 4, trees in the canyon are arranged on two rows bordering the road. Platanus acerifolia is the species with the largest presence along the street. Platanus acerifolia is a large deciduous tree growing in average 20–30 m, with a trunk circumference up to 3 m. The leaves are thick and stiff-textured, broad, palmately lobed, superficially maple-like, the leaf blade 10–20 cm long and 12–25 cm broad, with a petiole 3–10 cm long.

Tree crowns in via Laura Bassi reach 15-20 m in high, while the logs are approximately 4 to 6 m tall. Trees in the street are so close to each other to form two single compact rows for the most part of the canyon length.

Figure 4: Overview of Laura Bassi street and surrounding area (left) and Laura Bassi street canyon view (right).

Lazzaretto site

Lazzaretto site is in the neighbor of the city, located outside the city center. It is characterized by a major street (Terracini street), with smaller alleys on the East side. These streets are within a University Campus, with a low packing building density. An overview of the study area is shown in Fig. 6. The campus is characterized by streets with low traffic, but the streets around the campus are characterized by high car traffic. Two street canyons (called A and B) within the campus have been considered, with aspect ratios H/W(A)=1.7 and H/W(B)=0.9. The street canyons orientation with respect to the North-South coordinate is 145°.

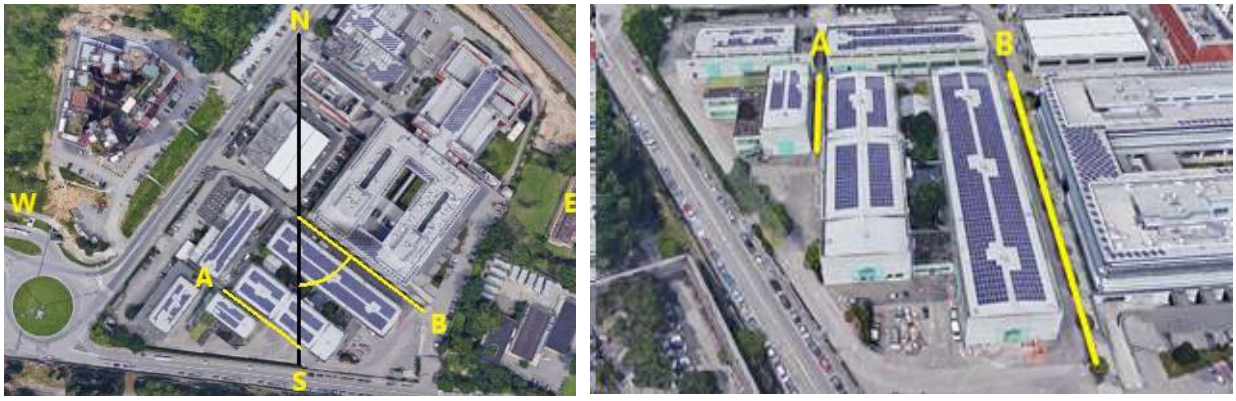

Figure 5: Overview of Lazzaretto site and surrounding area (left) and the two street canyons (right).

2.1.2 Field measurements and instrumentation

The boundary and initial conditions set in the simulations derive from experimental data obtained during the two field campaigns performed in Marconi St. and Laura Bassi St.: the first one conducted on August 2017 and the second one on February 2018 (D5.2). The third set of data obtained during a field campaign performed during August 2018 has been used for setting boundary conditions for the simulations on the Lazzaretto site (D3.8).

Meteorological data were obtained from measurements by two stations in different locations of the city: the first one is a synoptic meteorological station located at the top of Asinelli's tower (96 m above ground), the highest building of the city and the second one is an urban meteorological station placed on the roof of ARPAE's headquarter (27 m above ground; Silvani meteorological station).

At the inflow boundary, vertical profiles for mean velocity U (Eq. 2.1), turbulence kinetic energy *k* (Eq. 2.2) and turbulence dissipation rate ε of the neutrally stratified atmospheric boundary layer (Eq. 2.3) have been imposed, according to Di Sabatino et al. (2007):

$$U(z) = \frac{u_*}{k} ln\left(\frac{z-d}{z_0}\right) \quad (1)$$

$$k(z) = \frac{u_*^2}{\sqrt{C_\mu}}\left(1 - \frac{z}{\delta}\right) \quad (2)$$

$$\varepsilon(z) = \frac{u_*^3}{k(z+z_0)}\left(1 - \frac{z}{\delta}\right) \quad (3)$$

with *z* the vertical position above the ground, z_0 the roughness length representative for the terrain windward the computational domain, u_* the friction velocity, k=0.42 the van Karman constant, C_μ=0.09 and δ the height of the computational domain.

The inflow wind profile has been calculated solving a two equations system using data from the two meteorological stations (Asinelli and Silvani), in order to obtain the friction velocity u_* and the roughness length z_0 for every different wind condition. The displacement height d has been set to 11 m for Marconi street and 5.67 m for Laura Bassi street, equal to 1/3 of the street canyon medium height. This approach highlights the relationship between wind direction and urban geometry.

The street canyon façade temperatures were provided from the measurements taken during two thermographic campaigns, thoroughly described in D5.2. In brief, two Infrared (IR) cameras were used to take photographs of asphalts and building façades every two hours for a period of 24 hours from 12 am on 22 August 2017 to 12 am on 23 August 2017 and from 12 am on 8 February 2018 to 12 am on 9 February 2018. All the results in this and in the following sections refer to local time.

In particular, the building façades temperature was measured on 6 buildings along Marconi street and 6 along Laura Bassi street chosen for the characteristics of the wall emissivity, with 3 building for each side of the street canyons. The position of the buildings is shown in Fig. 6. In Marconi street, the buildings 1, 2 and 9 are on the East side and 4,5 and 7 are on the west side, while 3 and 8 are the positions where the street temperatures have been measured. In Laura Bassi street, the buildings 5, 6 and 9 are on the East side and 1,2 and 3 are on the West side, while 4 and 8 are the positions where the asphalt temperatures have been measured.

Figure 6: Positions of the building chosen for IR temperature measurements.

During the summer simulations for Marconi street, due to the variation of temperature with height, the thermographic images have been processed to obtain an average temperature value every 3 m of height on the façades. The values have been interpolated to obtain a function for every building surface facing the street canyon. This approach allows to consider the shading effect due to the presence of the other buildings and the high temperature gradients observed on the building façades in summer.

The temperature of the other building surfaces in Marconi and Laura Bassi streets has been calculated by averaging the mean temperature of the street canyon façades measured by the IR camera. As stated above, IR cameras measured also the ground temperature and the values obtained from the thermographic images was set into the simulations.

The measurements of temperature provided by the monitoring stations were analysed to create air temperature profiles. During the day, the temperatures do not present a significant variation with height, therefore constant vertical profiles have been set. Instead, during the night of the summer case, thermal inversion occurred at a height of about 100 m; therefore, the temperature profiles present a constant increase (about 2°C/100 m) until the temperature inversion quota and then a constant decrease 0.7°C/100 m).

Table 2 shows the values obtained from measurements and used for the velocity boundary conditions for the 13 cases studied in summer (both for Marconi street and for Laura Bassi street).

Day	UTC - Local time	Wind direction (°) and wind velocity (m s^{-1})	u_* (m s^{-1})	z_0 (m)
22/08/2017	10-12	127°-4.5	0.44	1.3
22/08/2017	12-14	93°-4.4	0.54	3.0
22/08/2017	14-16	91°-4.5	0.15	0.01
22/08/2017	16-18	107°-6.3	0.37	0.1
22/08/2017	18-20	138°-5.8	0.71	3.0
22/08/2017	20-22	151°-4.2	0.64	5.7
23/08/2017	22-0	190°-2.9	0.49	7.5
23/08/2017	0-2	215°-5	0.74	5.2
23/08/2017	2-4	257°-4.8	0.59	3.0
23/08/2017	4-6	239°-1.8	0.25	4.2
23/08/2017	6-8	221°-0.6	0.26	5.2
23/08/2017	8-10	92°-3.5	0.17	0.02
23/08/2017	10-12	76°-3.3	0.15	0.01

Table 2: Wind data used for setting the boundary conditions in the summer cases.

Input traffic emissions data were derived from the traffic counts available from counting stations using inductive loops technology in the two street canyons with a 5-min time resolution provided by ARPAE. In particular, emissions were derived converting traffic counts into traffic counts per vehicle type (fuel type, vehicle type, and EURO technology). First of all, the number of buses passing in the two street canyons were derived from bus schedules in Bologna (available from the regional transport company on the web at https://www.tper.it/o). The local fleet composition was then extracted from the regional inventory of circulating vehicles (also available on the web as open data from the Italian Car Club (http://www.aci.it/laci/studi-e-ricerche/dati-e-statistiche/open-data.html) and was used to disaggregate the difference between the traffic counts and the number of buses into traffic counts per vehicle type using the extracted local fleet composition. Pollutant emission rates were then estimated using European Monitoring and Evaluation Programme/European Environment Agency (EMEP/EEA) air pollutant emissions for each vehicle category (EEA, 2017). Concentration measurements provided by ARPAE's mobile stations and meteorological measurements obtained from middle level (about half of the canyon height) and top level (building roof) stations were used to validate the numerical model.

Table 2 shows the values obtained from IR measurements and used for the temperature boundary conditions for the 13 cases studied in summer for Marconi street.

Day	UTC - Local time	Tair (°C)	T4 (°C)	T5 (°C)	T7 (°C)	T2 (°C)	T1 (°C)	T9 (°C)	Tstreet (°C)
22/08/2017	10-12	25.07	35.59	33.61	33.61	27.58	26.21	28.14	26.38

22/08/2017	12-14	26.00	29.34	28.38	28.38	27.37	26.84	28.57	40.19
22/08/2017	14-16	26.65	30.31	28.55	28.55	38.05	35.30	41.45	32.37
22/08/2017	16-18	25.82	29.20	27.52	27.52	35.85	35.23	34.03	29.63
22/08/2017	18-20	23.85	23.68	24.80	24.80	27.38	27.50	27.72	26.43
22/08/2017	20-22	22.83	23.86	22.96	22.96	24.44	24.64	24.79	24.42
23/08/2017	22-0	20.61	22.80	22.43	22.43	23.25	22.75	23.71	23.29
23/08/2017	0-2	19.64	22.35	21.54	21.54	22.86	22.16	22.94	22.51
23/08/2017	2-4	19.71	21.95	20.99	20.99	22.18	21.35	21.78	21.65
23/08/2017	4-6	18.30	21.05	20.57	20.57	21.67	20.69	21.12	21.16
23/08/2017	6-8	20.31	22.91	22.43	22.43	23.13	21.77	23.03	22.66
23/08/2017	8-10	24.91	29.77	28.64	28.64	26.88	25.20	26.88	29.19
23/08/2017	10-12	27.45	37.97	35.28	35.28	29.22	27.79	29.42	37.64

Table 3: Temperature data used for setting the temperature boundary conditions in the Marconi St. summer cases.

Table 3 shows the values obtained from IR measurements and used for the temperature boundary conditions for the 13 cases studied in summer for Laura Bassi street.

Day	UTC - Local time	Tair (°C)	T4 (°C)	T5 (°C)	T7 (°C)	T2 (°C)	T1 (°C)	T9 (°C)	Tstreet (°C)
22/08/2017	10-12	25.07	34.0	32.9	34.1	27.6	27.4	28.0	28.95
22/08/2017	12-14	26.00	31.0	30.7	32.5	28.0	28.3	28.8	44.3
22/08/2017	14-16	26.65	30.0	29.6	30.3	30.0	29.2	29.0	36.9
22/08/2017	16-18	25.82	29.4	28.7	27.8	27.1	27.4	28.7	31.8
22/08/2017	18-20	23.85	27.3	26.6	26.	23.8	23.8	27.1	28.35
22/08/2017	20-22	22.83	24.6	24.4	24.5	24.3	24.5	25.9	26.35
23/08/2017	22-0	20.61	23.3	22.8	23.5	23.6	23.9	24.2	25.3
23/08/2017	0-2	19.79	22.5	22.7	22.2	19.85	21.9	23.4	24.0
23/08/2017	2-4	19.8	21.3	21.4	21.3	18.4	21.27	22.6	23.1
23/08/2017	4-6	18.9	20.5	20.5	20.5	17.8	20.3	21.9	22.3
23/08/2017	6-8	19.0	20.0	20.1	20.1	18.2	20.5	22.0	22.5
23/08/2017	8-10	23.6	24.9	23.1	28.8	23.5	23.2	25.1	26.25
23/08/2017	10-12	26.7	37.97	35.3	35.3	29.2	27.8	29.4	37.6

Table 4: Temperature data used for setting the temperature boundary conditions in Laura Bassi St. summer cases.

Table 4 shows the values obtained from measurements and used for the velocity boundary conditions for the 13 cases studied in winter (both for Marconi street and for Laura Bassi street).

Day	UTC - Local time	Wind direction (°) and wind velocity (m s^{-1})	u_* (m s^{-1})	z_0 (m)
08/02/2018	11-12	75° – 1.5	0.52	5.2
08/02/2018	13-14	79° – 2.1	0.42	1.7
08/02/2018	15-16	86°– 2.0	0.44	3.3
08/02/2018	17-18	88°– 2.0	0.52	5.2
08/02/2018	19-20	101° – 1.6	0.52	5.2
08/02/2018	21-22	96° - 3.2	0.64	6.5
09/02/2018	23-0	100° - 7.3	0.79	1.0
09/02/2018	1-2	99° - 7	1.01	4.9
09/02/2018	3-4	103° – 2.6	0.74	8.2
09/02/2018	5-6	107° – 2.3	0.59	5.2
09/02/2018	7-8	103° – 1.5	0.54	5.96
09/02/2018	9-10	104° – 2.1	0.64	6.5
09/02/2018	11-12	94° – 0.1	0.49	5.9

Table 5: Wind data used for setting the boundary conditions in the winter cases.

Table 5 shows the values obtained from IR measurements and used for the temperature boundary conditions for the 13 cases studied in winter for Marconi street.

Day	UTC - Local time	Tair (°C)	T1 (°C)	T2 (°C)	T3 (°C)	T4 (°C)	T5 (°C)	T6 (°C)	Tstreet (°C)
08/02/2018	11-12	7.45	13.95	11.46	11.46	9.75	7.46	9.55	9.10
08/02/2018	13-14	9.15	11.89	10.91	10.91	12.15	9.98	12.20	9.80
08/02/2018	15-16	9.50	10.52	10.72	10.72	11.81	10.42	10.76	7.50
08/02/2018	17-18	9.05	9.45	9.81	9.81	9.63	9.08	9.64	6.70
08/02/2018	19-20	8.00	7.24	8.41	8.41	7.59	6.99	7.33	3.65
08/02/2018	21-22	6.50	6.39	7.67	7.67	6.78	5.97	6.55	3.10
09/02/2018	23-0	7.30	7.18	8.13	8.13	7.10	6.72	6.99	2.70
09/02/2018	1-2	7.15	7.36	7.95	7.95	7.32	6.72	6.95	4.45
09/02/2018	3-4	7.05	6.98	7.76	7.76	7.31	6.71	6.82	4.70
09/02/2018	5-6	5.95	6.45	7.22	7.22	6.54	6.17	6.27	3.95
09/02/2018	7-8	5.30	5.11	6.70	6.70	5.54	4.57	5.23	2.03
09/02/2018	9-10	7.10	6.91	7.86	7.86	7.34	5.95	7.17	3.55
09/02/2018	11-12	10.05	16.18	14.47	14.47	11.46	8.57	10.59	5.60

Table 6: Temperature data used for setting the boundary conditions in the Marconi St. winter cases.

Table 6 shows the values obtained from IR measurements and used for the temperature boundary conditions for the 13 cases studied in winter for Laura Bassi street.

Day	UTC-Local time	Tair (°C)	T1 (°C)	T2 (°C)	T3 (°C)	T4 (°C)	T5 (°C)	T6 (°C)	Tstreet (°C)
08/02/2018	11-12	6.96	13.5	13.5	13.2	11.7	9.4	9.3	12.05
08/02/2018	13-14	9.03	13.5	13.3	13.5	10.9	10.9	9.7	13.6
08/02/2018	15-16	9.28	12.6	11.7	10.9	10.9	9.4	10	8.75
08/02/2018	17-18	8.92	8.3	8.5	8.5	7	7.8	8.4	6.75
08/02/2018	19-20	8.18	7.5	7.6	7	6.2	7.6	7.6	5.5
08/02/2018	21-22	6.77	7.2	7.4	5.3	4.8	5.4	7.8	4.6
09/02/2018	23-0	6.86	7.3	8.5	7.5	6.1	8.2	7.9	6.3
09/02/2018	1-2	7.15	5.6	8.5	8.5	6.3	8.2	8.4	6.3
09/02/2018	3-4	7.05	6.7	8.4	8.4	6.5	7.9	7.7	6.5
09/02/2018	5-6	5.77	5.4	8.4	7.7	4.3	6.8	8.4	5.25
09/02/2018	7-8	5.59	8	6.5	7.3	4.8	6	7.2	5.0
09/02/2018	9-10	6.79	12.3	12.2	9.5	8.3	7.8	9.6	6.5
09/02/2018	11-12	9.79	13.7	13.5	13.2	9.2	9.6	10.9	12.0

Table 7: Temperature data used for setting the boundary conditions in the Laura Bassi St. winter cases.

Table 7 shows the values obtained from measurements and used for the velocity boundary conditions for the 3 cases studied in summer cases at Lazzaretto.

Day	UTC-Local time	Wind direction (°)	u_* (m s^{-1})	z_0 (m)
17/08/2018	2-4	223°	0.21	6.57
17/08/2018	14-16	8°	0.21	6.57

Table 8: Wind data used for setting the boundary conditions in the Lazzaretto site cases.

Table 8 shows the values obtained from measurements and used for the temperature boundary conditions for the 3 cases studied in summer at Lazzaretto.

Day	UTC - Local time	Tair (°C)	T1 (°C)	T2 (°C)	T3 (°C)	T4 (°C)	T5 (°C)	T6 (°C)
17/08/2018	10-12	21	32	31.75	30.1	26.03	29.43	26.87
17/08/2018	12-14	31.1	45.95	36.9	36.3	49.53	34.85	32.45

Table 9: Temperature data used for setting the boundary conditions in the Lazzaretto site cases.

Wind data from the Asinelli meteorological station located around 2 km east of the monitoring sites for the year 2017 (obtained by the Regional Authority ARPAE weather station) are reported in Fig. 7. In 2017, the recorded average wind speed was 4.3 m s^{-1} and the prevalent wind direction

was south-west. These data have a frequency of 30 min with a wind accuracy of 10°. Data show that the two days chosen for representing the diurnal cycles are consistent with the average values; in fact, although Bologna is mostly affected by winds from the south-west, there is also residual but intense components from the east, and winds impinging on the city are mainly characterized by low speeds (less than 4 m s^{-1}) (D6.1), as in the two days considered here.

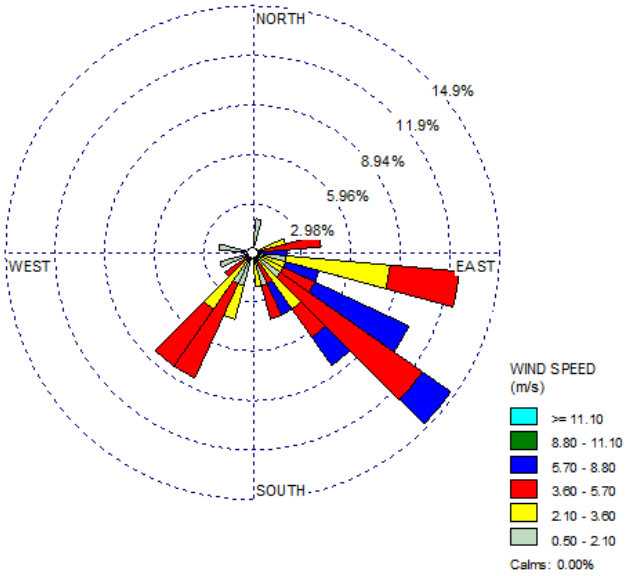

Figure 7: Typical wind rose for Bologna city centre using 2017 hourly data.

The set of instrumentations deployed as part of the intensive field experimental campaigns, thoroughly described in D3.3 and D5.2 and used for the validation of the numerical results presented in this report, can be summarised as follows:

- Ground station:
  - Sonic anemometer (Windmaster, Gill)
  - Thermohygrometer (HC2S3-L, Campbell Scientific)
  - Nitrogen oxides (NO_x), ozone (O_3), carbon monoxide (CO), BTEX (Teledyne Instruments) and particulate matter or PMx (Fai Instruments) concentration sensors
- Balcony station (at 8 m high for Marconi street, 9 m for Laura Bassi street):
  - Sonic anemometer (Windmaster, Gill)
  - Thermohygrometer (HC2S3-L, Campbell Scientific)
- Rooftop station (at 25 m high for Marconi street, 15 m for Laura Bassi street):
  - Sonic anemometer (uSonic-3, Metek) coupled with LI-COR (LI-COR 7500 RS)
  - Net radiometer (CNR4, Kipp & Zonen)

As described in D5.2, this instrumentation setup provided air pollutant concentrations with 1-min time resolution, and measurements of meteorological and turbulence parameters, namely air temperature, velocity components and turbulence, at 1 min and 50 ms and time resolution,

respectively; 1-h averages of those measurements were used for validating the CFD simulations results. The instrumental setup used for the validation of the CFD simulations at the Lazzaretto site (provided in D3.6), presented thoroughly in D3.8, can be summarized as follows:

- Ground station:
  - Sonic anemometer (Windmaster, Gill)
  - Thermohygrometer (HC2S3-L, Campbell Scientific)
  - NOx, O_3, CO (Teledyne Instruments) and PMx (Fai Instruments) concentration sensors
- Rooftop station (at 8 m high for Marconi street, 9 m for Laura Bassi street):
  - Sonic anemometer (Windmaster, Gill)
  - Thermohygrometer (HC2S3-L, Campbell Scientific)
  - Net radiometer (CNR4, Kipp & Zonen)

Similar to the two campaigns in the two urban street canyons in Bologna, this instrumentation setup provided air pollutant concentrations with 1-min time resolution, and measurements of meteorological and turbulence parameters, namely air temperature, velocity components and turbulence, at 1 min and 50 ms and time resolution, respectively; again, 1-h averages of those measurements were used for validating the CFD simulations results.

2.1.3 Numerical setup and simulations

Equations and models

The CFD code CD-adapco STAR-CCM+ 12.02.10 has been employed to solve the steady-state Reynolds-averaged Navier–Stokes (RANS) equations with realizable k-ε turbulence model. The buoyancy thermal effects have been considered in this work.

The transport equations for kinetic energy k and the turbulent dissipation rate ε are:

$$\frac{\partial}{\partial t}(\rho k) + \nabla \cdot (\rho k u) = \nabla \cdot \left[\left(\mu + \frac{\mu_t}{\sigma_k}\right)\nabla k\right] + P_k - \rho(\varepsilon - \varepsilon_0) + S_k \quad (4)$$

and

$$\frac{\partial}{\partial t}(\rho \varepsilon) + \nabla \cdot (\rho \varepsilon u) = \nabla \cdot \left[\left(\mu + \frac{\mu_t}{\sigma_\varepsilon}\right)\nabla \varepsilon\right] + \frac{1}{T_\varepsilon} C_{\varepsilon 1} P_\varepsilon - C_{\varepsilon 2} f_2 \rho \left(\frac{\varepsilon}{T_\varepsilon} - \frac{\varepsilon_0}{T_0}\right) + S_\varepsilon \quad (5)$$

Where
u is the average velocity, μ is air dynamic viscosity, σ_k, σ_ε, $C_{\varepsilon 1}$, and $C_{\varepsilon 2}$ are model coefficients, P_k and P_ε are production terms, whose formulation depend on the k-ε model variant, f_2 is a damping function that mimics the decrease of turbulent mixing near the walls, enforcing realisability, S_k and S_ε are used specific source terms, ε_0 is the ambient turbulent dissipation rate value in the source terms, T_ε is the large-eddy time scale, T_0 the specific time-scale related to ambient turbulent source term. Mean flow, turbulence, energy and dispersion equations were discretized using a second order schemes and the Semi-Implicit Method for Pressure Linked Equation (SIMPLE) scheme was used for pressure-velocity coupling.

Heat transfer model

The buoyancy forces have been considered under the Oberbeck-Boussinesq approximation, i.e. in Navier-Stokes equation the mass density is constant in all the terms with exception of in the gravitational body force term. The local momentum balance equation then gives:

$$\rho\left(\frac{\partial u_i}{\partial t}+u_j\frac{\partial u_i}{\partial x_j}\right)=\rho g_i-\frac{\partial p}{\partial x_i}+\frac{\partial \tau_{ij}}{\partial x_j} \quad (6)$$

where, the density ρ is assumed to be a function of temperature and pressure in accordance with the ideal gas law:

$$\rho(T,p)=\frac{p}{RT} \quad (7)$$

Where R is the specific gas constant, $R=\frac{R_0}{M}$, with R_0=8314.4621 (J kmol K^{-1}) and M is the gas molecular weight.

Species transport model

In this work, CO has been used as tracer pollutant for Marconi and Laura Bassi simulations, while NO has been used as pollutant for the simulations conducted at the Lazzaretto site.

In turbulent flows, STAR-CCM+ computes the mass diffusion as:

$$J=-\left(\rho D+\frac{\mu_t}{Sc_t}\right)\nabla c \quad (8)$$

where D is the molecular diffusion coefficient for the pollutant in the mixture, $\mu_t=\rho\left(\frac{C_\mu k^2}{\varepsilon}\right)$is the turbulent viscosity, Y is the mass fraction of the pollutant, ρ is the mixture density.

$Sc_t=\frac{\mu_t}{\rho D_t}=0.7$ is the turbulent Schmidt number, where D_t is the turbulent diffusivity.

The pollutant sources have been simulated by separating volumes of section 0.5 m x 0.5 m. Four linear sources have been created in Marconi street canyon: two simulating the car traffic and two simulating the public bus traffic. In Riva di Reno street and Laura Bassi street two linear sources for each canyon have been modelled to represent the car traffic emissions. The emissions rate (ER) was set using emissions previously derived with the methodology outlined above and by splitting the values equally into the linear sources.

Modelling momentum sink induced by vegetation

The representation of vegetation in the simulations is crucial to capture its effects on wind flow in urban areas. In this work, trees have been modelled as sources and sinks of momentum, heat, turbulence kinetic energy and turbulent dissipation rate. As done by other recent works on urban CFD vegetation (Jeanjean et al., 2017), the inertial drag has been parameterized in terms of leaf area density or LAD (m^2 m^{-3}) of the vegetation to describe the interactions between foliage and atmosphere, by means of a momentum sink term (Su_j) in momentum equations (one for each velocity component) as:

$$S_{U_j}=-\rho LAD C_d U u_j \ \text{(Pa m}^{-1}\text{)} \quad (9)$$

where ρ is the air density (kg m^{-3}), u_j is the j wind velocity component (m s^{-1}), U is the average wind speed (m s^{-1}) and C_d is the sectional drag for vegetation (dimensionless). The sectional drag is a constant related to aerodynamic features of vegetation. In this work we assume C_d =0.2, while the value of LAD for Platanus acerifolia has been taken as 1.8 (m^2 m^{-3}), according to the value found in literature for Acer platanoides (Klingberg et al., 2015). Fig. 8 shows that the leaves and the crown shapes of the two species are very similar.

Modelling of turbulence modifications by vegetation

The vegetation also modifies the mean flow motion into wake turbulence. Then, this process is usually parametrized as source and sink terms of turbulent kinetic energy or TKE (k) and turbulent dissipation rate (ε) as follows:

$$S_k = \rho LADC_d\left(\beta_p U^3 - \beta_d Uk\right) \quad \text{(kg m}^{-1}\text{ s}^{-3}\text{)} \quad (10)$$

$$S_\varepsilon = \rho LADC_d\left(C_{\varepsilon 4}\beta_p \frac{\varepsilon}{k} U^3 - C_{\varepsilon 5}\beta_d U\varepsilon\right) \quad \text{(kg m}^{-1}\text{ s}^{-4}\text{)} \quad (11)$$

where $0 \leq \beta_p \leq 1$ is the fraction of mean kinetic energy converted into TKE by means of drag, β_d is the dimensionless coefficient for the short-circuiting of the turbulence cascade; $C_{\varepsilon 4}$ and $C_{\varepsilon 5}$ are model constants. Several values of these parameters can be found in the literature; in this work we have used $\beta_p=1$, $\beta_d=4$ and $C_{\varepsilon 4}=C_{\varepsilon 4}=1.5$, according with Buccolieri et al. (2018) and Amorim et al. (2013).

Figure 8: Leaves shape for platanus acerifolia (left, top) and for acer platanoides (right, top); shape of the tree for platanus acerifolia (left, bottom) and for acer platanoides (right, bottom) (Rushforth, (1999)). Trees of Britain and Europe, Harper Collins).

Modelling of pollutant removal due to vegetation

The pollutant flux S_d (g m^{-2} s^{-1}) is calculated as the product of the dry deposition velocity V_d (cm s^{-1}) and pollutant concentration c (g m^{-3}):

$$S_d = -LADV_d c \quad (12)$$

Dry deposition velocity is calculated as the inverse of the sum of resistances to pollutant transport:

$$V_d = (R_a + R_b + R_c)^{-1} \quad (13)$$

Where R_a is the resistance to air flow in the crown, R_b is the resistance through the boundary layer adjacent to canopy surfaces resistance and R_c represents the chemical and biological absorption capacity of the canopy surfaces.

Modelling of transpirational cooling due to vegetation

The transpiration cooling of vegetation has been recently included in thermal CFD simulations to evaluate the impact on temperature. In order to account for the effect of vegetation on air temperature, Gromke et al. (2015) employed a volumetric cooling power P_c (W m^{-3}) per unit volume vegetation as a function of LAD. The same approach is used in this work.

The basic principle is that when air flows through vegetation it gets cooled by transpiration mainly from the leaf surfaces. The heat H (J) required to change the temperature of an object can be calculated according to (Incropera et al., 2011):

$$H = mc_p\Delta T \tag{14}$$

with c_p the specific heat capacity (J K^{-1} kg^{-1}), m (kg) the mass of the object and ΔT the change in temperature (K). Since the volumetric cooling power P_c is understood as the transfer of heat per time t (s) and volume V (m^3), the equation can be rearranged to:

$$\frac{H'}{V} = P_c = c_p\Delta T\frac{1}{V} \rightarrow \Delta T = P_cV\frac{1}{m'}\frac{1}{c_p} \tag{15}$$

with H the heat transfer rate (W) and $\dot{m}$ the mass flow rate (kg s^{-1}).

The right part of the last equation states that the change in temperature ΔT when air flows through vegetation is proportional to the cooling power P_c and the volume of the vegetation V and inversely proportional to the air mass flow $\dot{m}$ through the vegetation volume and the specific heat capacity c_p of air. The equation is based on the simplified assumption that the heat and mass transfer at the leaf surface is not a function of the flow regime and the corresponding heat transfer coefficient. The same model has been recently applied by Moradpour et al. (2017). Gromke et al. (2015) and Moradpour et al. (2017) found the best agreement with experimental air temperature in different validation studies for a volumetric cooling power of 250 W m^{-3} per unit of LAD.

Discretization methods and meshes

Different meshes with the same constructive approach have been created for the two different street canyons.

Marconi street (no trees street canyon)

The computational domain has a size of 1288 m x 920 m x 368 m (L x W x H). The domain dimensions are multiple of the base size of the mesh equal to 11.5 m. The height of the tallest building of the street canyon (H = 46 m) has been chosen as reference dimension.

The computational domain was built with its boundaries placed 15H away from the modelled area. The top of the computational domain was set to 368 m, which corresponds to 8H. The dimensions of outer domain give an appropriate mesh size for the required flow detail and run time. The computational domain has been built using unstructured elements with a finer resolution close to the ground and the walls within the neighbourhood scale. Several tests have been performed to verify grid size independence with increasing mesh numbers. The smallest dimension of the elements, in the region near the heated walls, is 0.25 m in the direction normal to the wall and 0.5

m in the other directions. Figure 9 shows the computational domain (left) and some details of the mesh (right). The pollutant sources were modelled as linear volumes on the ground of the street. The dimensions of the source section are 0.5 m x 0.5 m, while the length coincide with the length of the street canyon. In Marconi street, four linear sources have been created, two for car traffic and two for bus traffic; in Riva di Reno street, two linear sources for car traffic have been created. For every source, the base grid dimension is of 0.1 m. The ER was set using those obtained with the methodology outlined above by splitting the value equally into the linear sources.

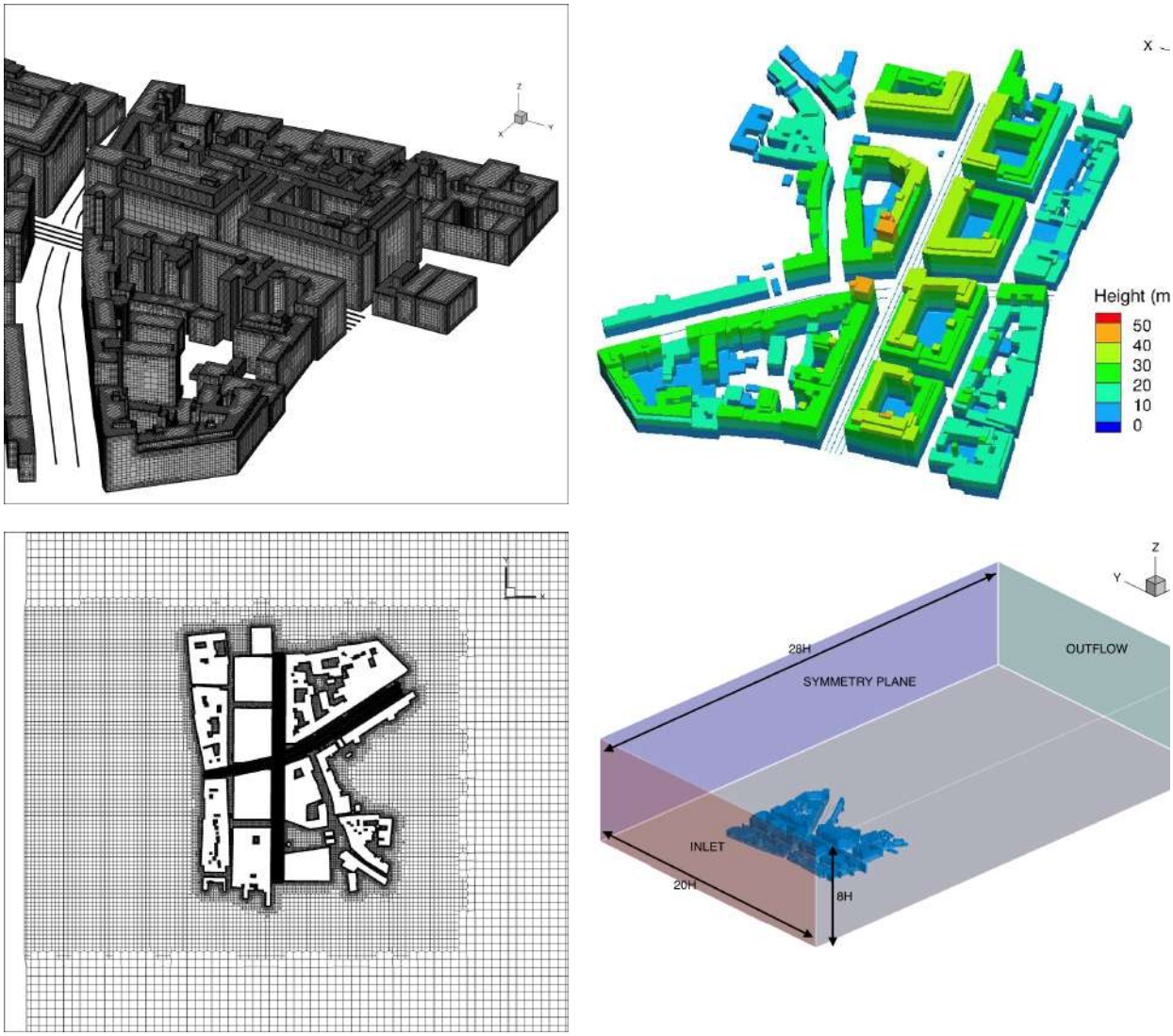

Figure 9: Marconi street. Mesh on the building surfaces (left top), elevation of the buildings (right, top), top view of the mesh (left, bottom) and the computational domain (right, bottom).

Within the domain, two regions with different grid resolution were generated: one in the area surrounding the buildings and in the area approaching the city with a dimension of 5.75 m, and the other one comprehending Marconi street canyon and with a cell size of 1.4375 m. Several refinements have been done on the building surfaces in order to have a close representation of

the real geometry, especially on the building edges. The final number of the computational cells used for Marconi street is about 12 million cells. Symmetry boundary condition has been assigned to the lateral sides and the domain top, a velocity inlet condition was set to the inlet boundary and a pressure outlet condition to the outflow boundary. A no-slip boundary condition was applied at the ground and at the building surfaces.

2.1.3.1.1 Laura Bassi street - Street canyon with trees

Given that maximum reported height in the domain is a building of 28 m height (H), the base size for the mesh was set to 2H due to the considerable size of the computational domain. As done for Marconi street, two refinement boxes have been created in the proximity of the geometry. The bigger box has a characteristic dimension of H/2 while the finest one has a characteristic dimension of H/8. The surfaces of the more than 450 buildings of small dimensions present in the geometry have been modelled with a grid base size smaller than H/16. In Laura Bassi street canyon also trees have been modelled: on sight measurements were used to approximate the tree crown dimensions while the trunks were not modelled. The base mesh dimension for trees was assumed to be 1 m. Figure 10 shows some details of the mesh. In Laura Bassi street two pollutant sources have been created to simulate car and bus traffic, whose base dimension was set to 0.1 m. The computational domain has a size of 3080 m x 2800 m x 280 m (L x W x H).

Within the domain, two regions with different grid resolution were generated: one in the area surrounding the buildings and in the area approaching the city with a dimension of 7 m, while the other comprehends the Laura Bassi street canyon and has a cell size of 1.75 m. Several refinements have been done on the building surfaces in order to have a close representation of the real geometry, especially on the building edges.

The pollutant source has been simulated by separating volumes with section of 0.5 m x 0.5 m and length equal to the street canyon length. In this case, two linear sources have been modelled to represent the traffic emissions. The emissions rate was set as detailed above, i.e. by splitting the value obtained from the traffic counts equally into the linear sources. The base size of the linear sources is 0.1 m and the smaller cells have a dimension of 0.05 m. The ER was set using those obtained with the methodology outlined above by splitting the value equally into the linear sources.

Only trees alongside the street have been modelled in this work. Since trees in the street are close to each other to form single compact rows for the most part of the canyon length, they have been modelled as single compact blocks. The tree logs have not been modelled. The dimensions of the tree blocks have been set after on-field measurements sessions. The base mesh size is equal to 1 m, while the smallest tree cell is 0.1 m. Symmetry boundary conditions have been assigned to the lateral sides and the domain top, a velocity inlet condition was set to the inlet boundary and a pressure outlet condition to the outflow boundary. A no-slip boundary condition was applied at the ground and at the building surfaces.

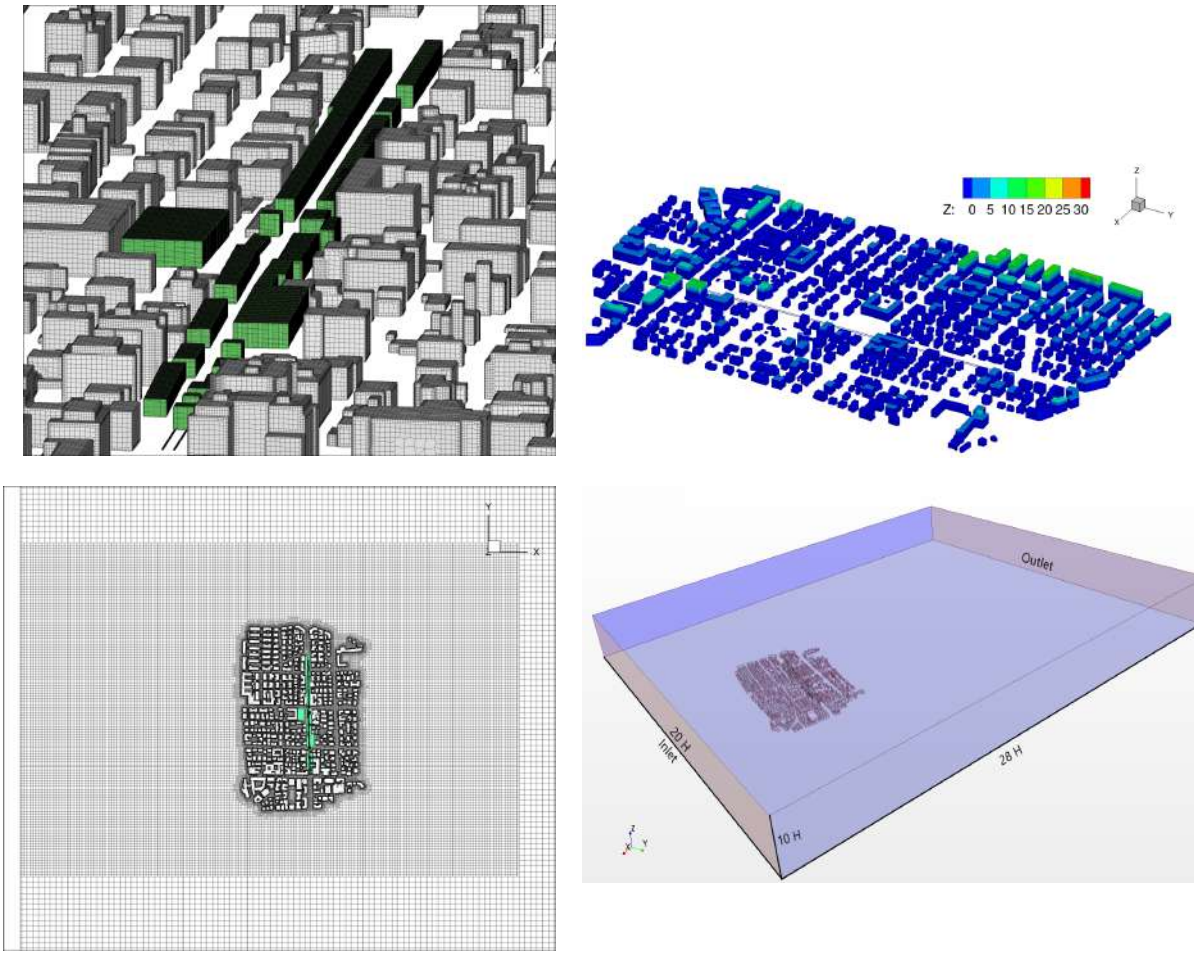

Figure 10: Laura Bassi street. Mesh on the building surfaces (left top), elevation of the buildings (right, top), top view of the mesh (left, bottom) and the computational domain (right, bottom).

2.1.3.1.2 Lazzaretto site

The computational domain has a size of 652 m x 375 m x 130 m (L x W x H). The domain dimensions are multiple of the height of the tallest street canyon H = 11.5 m, that has been chosen as reference dimension.

Within the domain, two regions with different grid resolution were generated: one in the area surrounding the buildings and in the area approaching the site with a dimension of 2.4 m, the other comprehending the site with a cell size of 0.18 m (as shown by Fig. 11, bottom left). Symmetry boundary conditions have been assigned to the lateral sides and the domain top, a velocity inlet condition was set to the inlet boundary and a pressure outlet condition to the outflow boundary. A no-slip boundary condition was applied at the ground and at the building surfaces.

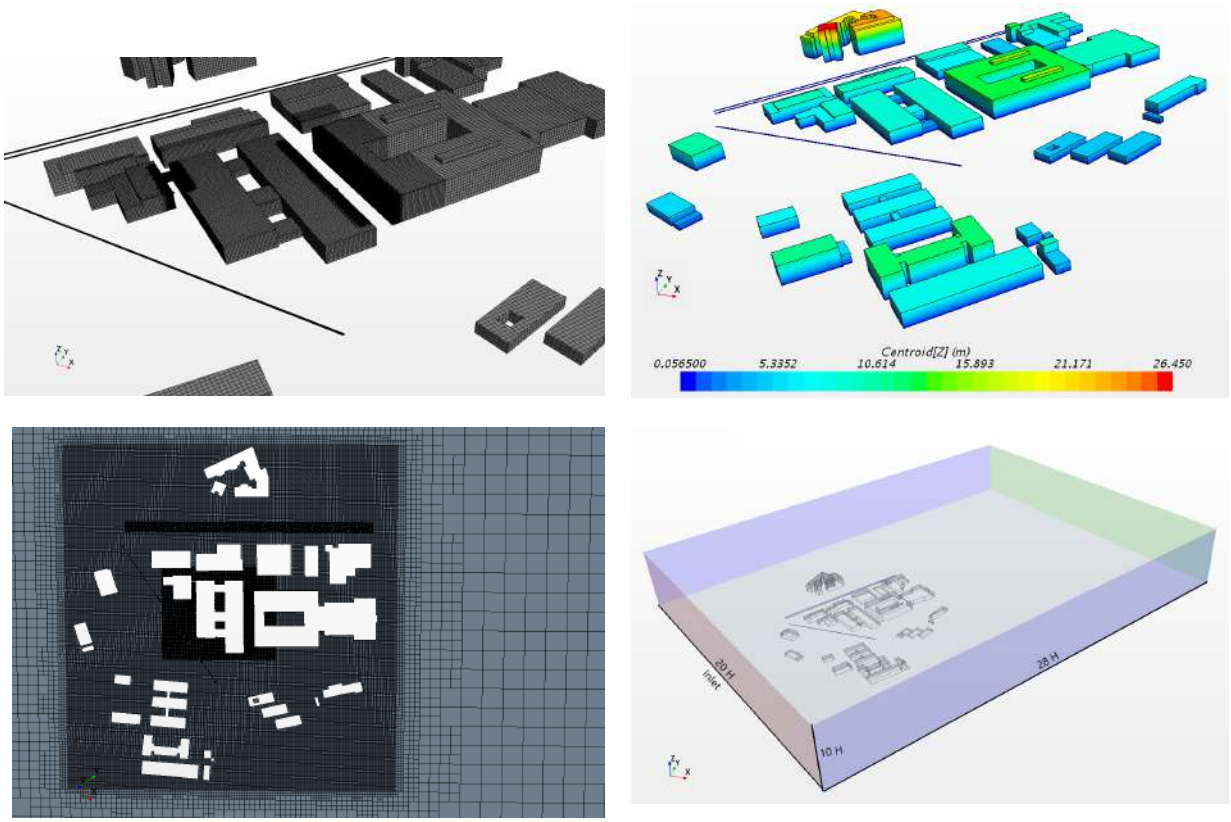

Figure 11: Lazzaretto site. Mesh on the building surfaces (left top), elevation of the buildings (right, top), top view of the mesh (left, bottom) and the computational domain (right, bottom).

Grid sensitivity tests

A set of preliminary sensitivity tests have been performed, both for choosing the dimensions of the boxes used for refinements and for choosing the dimensions of the elements near the building walls. As shown in Figs. 9-11, the mesh is built by three zones, each of them characterized by structured elements with homogeneous dimensions. The first zone is the external domain, with the coarsest elements, containing a box with elements with a medium size and another box surrounding the area and the street canyons, containing the finest elements. An example of the three zones is shown in Fig. 12.

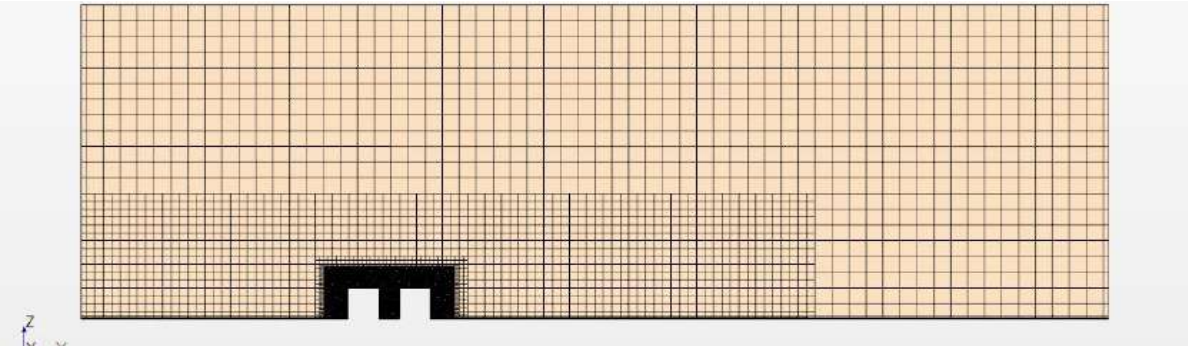

Figure 12: Example of mesh zones.

A geometry with a canyon with the same dimensions of Marconi street has been used as a base geometry for the first part of the sensitivity tests. Table 9 shows the dimensions of the box containing the finest elements, the size of the elements and the total number of cells N_{cells} in the computational domain. Six refinements have been compared, in the range N_{cells}=[0.302 – 6.181] millions of elements.

Grid name and index	Box dim	s_{min}	Number of cells (millions)
Very coarse - 5	$2\sqrt{2}H$	2.917	0.302
Coarse - 4	$2H$	2.062	0.528
Medium - 3	$2H/\sqrt{2}$	1.458	1.083
Fine - 2	H	1.031	2.550
Very fine - 1	$H/\sqrt{2}$	0.729	6.181
Ultra-fine - G	$H/2\sqrt{2}$	0.516	15.904

Table 10: Some of the grids used for the sensitivity tests.

Fig. 13 shows the normalized root mean square deviation obtained from a vertical line in the middle of the canyon, defined by

$$NRMSE_g = \sqrt{\frac{\Sigma_p\left(\frac{x_{g,p}-x_{G,p}}{x_G}\right)^2}{N_p}} \quad (16)$$

where *x* is the variable used for the comparison, *g* is the grid number, *p* is the point along a probe line where the comparison is made, N_p is the number of points in the probe line. Fig. 13 shows that the convergence is achieved for velocity, CO concentration and temperature results.

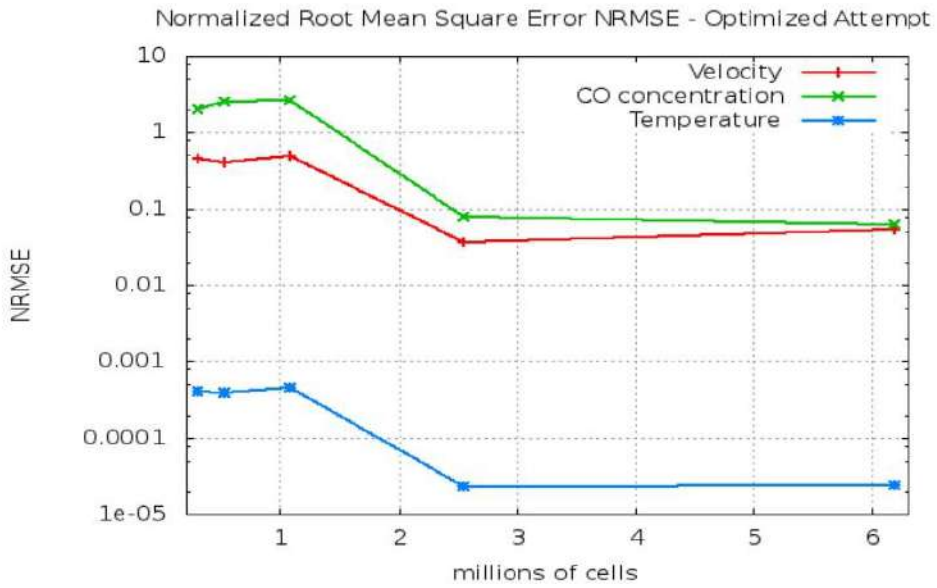

Figure 13: Convergence tests for velocity, CO concentration and temperature in the CFD simulations for Marconi street canyon.

2.1.4 Investigated PCS scenarios

In this section, the cases analysed are briefly described and the validation of the simulations is shown. For the street canyon without trees (Marconi street), 26 cases have been studied, 13 cases for the summer diurnal cycle and 13 cases for the winter diurnal cycle. The boundary conditions described in Section 2.1.2 by Tables 1, 2 and 4, 5 have been used. As the wind direction is different for each case, a geometry has been built for each case, in order to have the wind entering in the domain perpendicular to the inlet section. Then, for Marconi street, 26 geometries have been built.

For the street canyon with trees, 26 cases have been studied, representative of summer and winter diurnal cycles. The boundary conditions described in Section 2.1.2 by Tables 1, 3 and 4, 6 have been used. A geometry has been built for each case, in order to have the wind entering in the domain perpendicular to the inlet section. Then, for Laura Bassi street, 26 geometries have been built.

Validation of the simulations – Street canyon without trees

The simulations have been validated by comparing hourly values as obtained from the numerical simulations with the measurements performed during the two experimental campaigns described in Section 2.1.2 and thoroughly described in D5.2.

Fig. 14 shows the comparison between the simulations and the experimental measurements for Marconi street, during the summer campaign. As described in D5.2, instrumentation for measuring CO concentrations was located on the top of the ARPAE van, while temperature, velocity and TKE were measured over a balcony 8 m high and 1 m distant from the building wall.

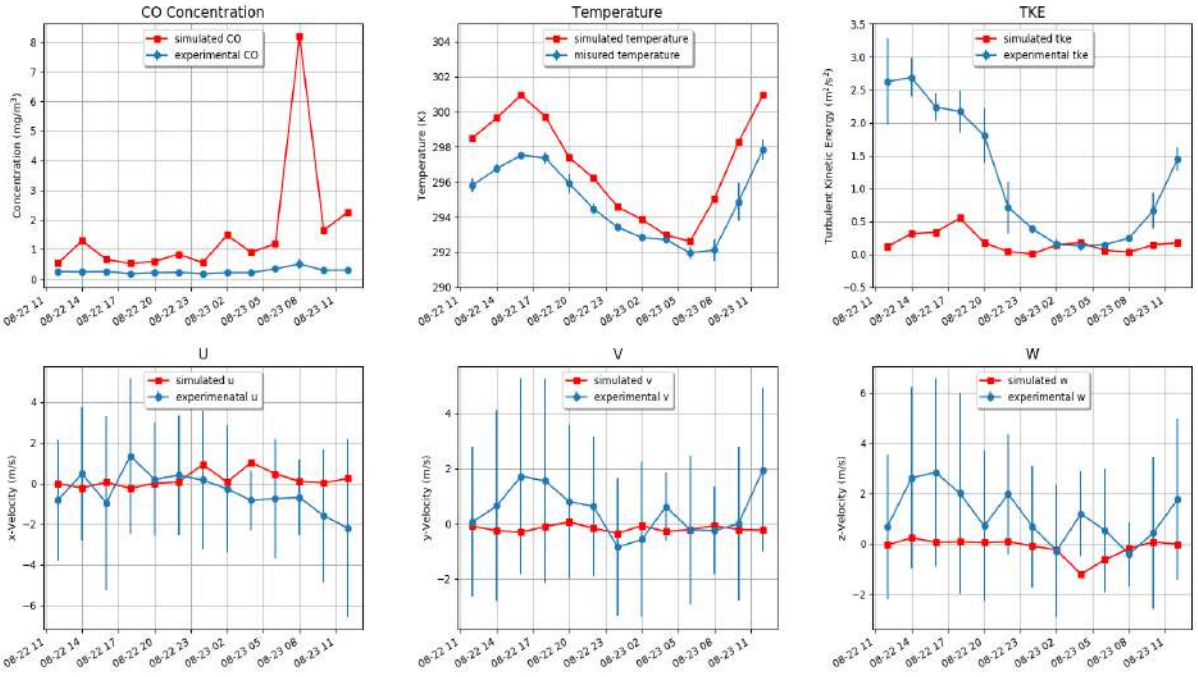

Figure 14: Marconi street, summer. Comparison between numerical results (red) and experimental results (blue).

Fig. 14 shows that CO concentrations (top line, first from left) obtained from numerical simulations are overestimated, as numerical values are between 2 and 10 times bigger than measured ones. In particular, the concentration value obtained in one case (case 23/08/2017 at 8 am) largely overestimates the measured one. The vertical distribution of CO obtained for this case is shown in Fig. 15.

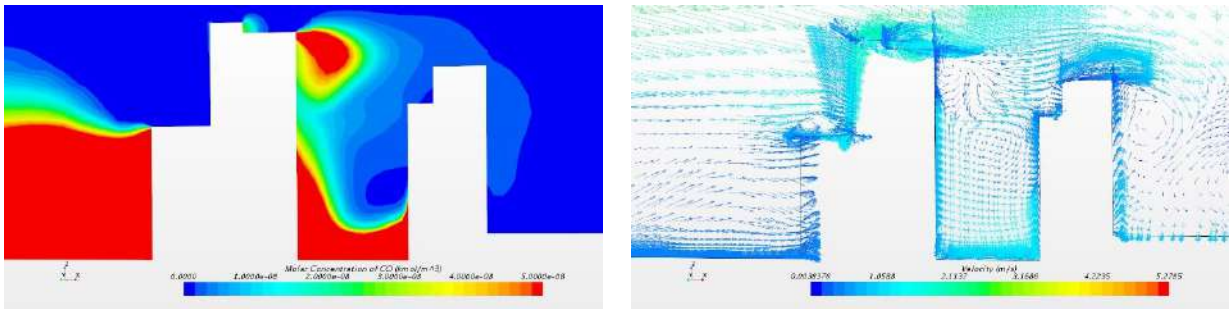

Figure 15: Marconi street, summer case: 23/08/2017, 8:00 am. CO concentration contours (left) and air velocity vectors (right).

Fig. 15 shows that at that time, a clockwise vortex was present on the upper part of the canyon. This vortex is not perfectly perpendicular to the canyon and causes CO removal in the upper part of the canyon and a strong velocity and concentration gradient at a height close to the height where the top of ARPAE van was located. That means that in this case, the dimension of the vortex obtained by simulations is underestimated and the real one was bigger, i.e. in the real case the CO gradient was below the ARPAE van station. To confirm this, one can observe that at that time the components of velocity measured on the balcony, i.e. at a higher level, are in agreement with measurements. Fig. 15 shows that at pedestrian level there could be higher concentrations with respect to those measured by the ARPAE van at a height of around 3 m.

The comparison between air temperatures obtained by numerical simulations and experiments (Fig. 15, top line, middle) shows that the temperatures are 1-3 degrees higher than experiments in all the simulations. This is caused by the fact that the temperature boundary conditions are obtained by averaging on highly non-uniform temperatures on the building façades, caused by the sun shadows (as shown by Fig. 16).

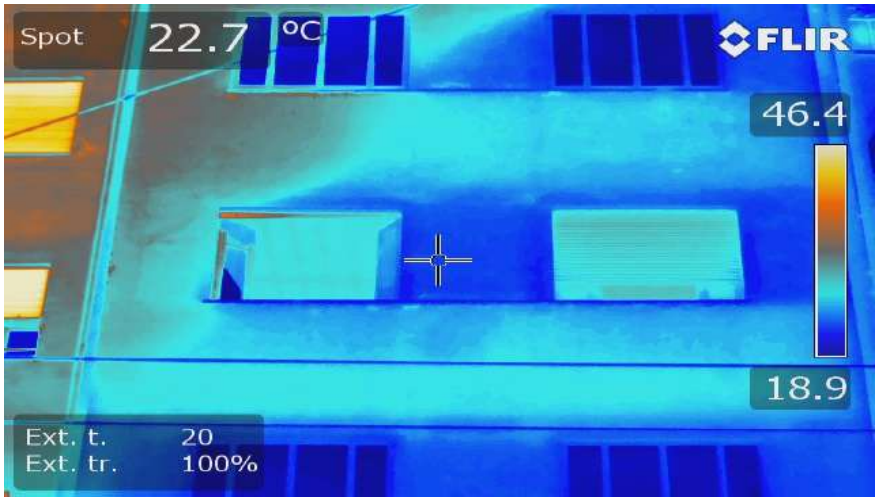

Figure 16: IR thermographic image of one façade of one building along Marconi street at 8:00 of 23/08/2017.

Finally, Fig. 15 shows that although numerical TKE is underestimated by simulations, numerical velocity components agree with experiments.

Fig. 17 shows the comparison between the simulations and the experimental measurements for Marconi street, for the winter cases. For CO concentrations, the values obtained in four cases strongly overestimate the measured one, in particular for the 08/02/2018 at 18:00 and 22:00 and the 09/02/2018 at 8:00 and 10:00 cases. The vertical distribution of CO obtained for these cases and the vector maps are shown in Fig. 18 (left and right respectively). Fig. 18 shows that for all the cases considered a vortex was present on the upper part of the canyon, causing CO removal in the upper part of the canyon and a strong velocity and concentration gradient in the region at the middle of the canyon. The comparison between air temperatures obtained by numerical simulations and experiments (Fig. 17, top line, middle) shows that the temperatures are 1-3 degrees lower than experiments. Finally, Fig. 17 shows that numerical TKE is in a very good agreement with experiments, with the exception of the night cases (on 09/02/2018 at 0:00 and 2:00 am). For these cases, the numerical velocity components do not agree with experiments during (the W component i.e. the vertical component).

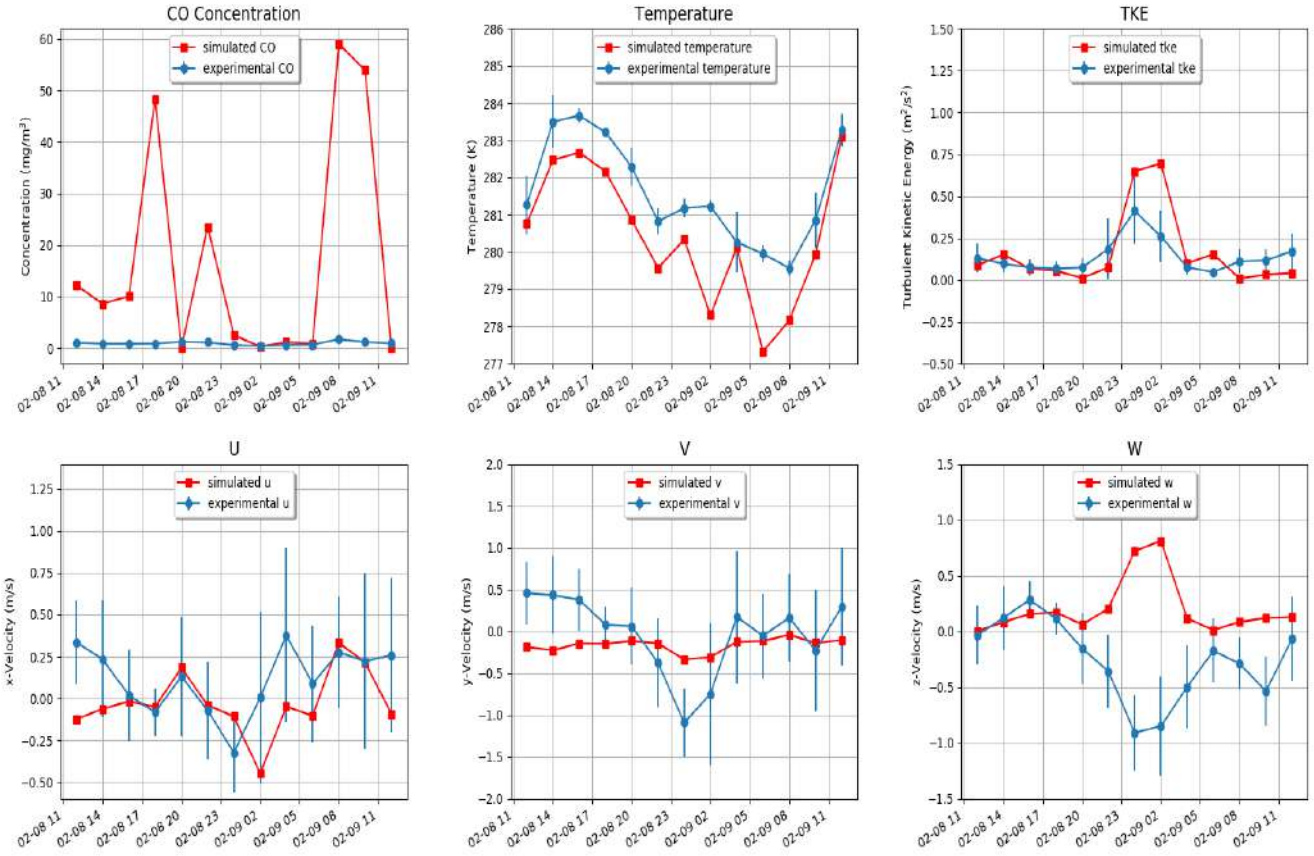

Figure 17: Marconi street, winter. Comparison between numerical results (red) and experimental results (blue).

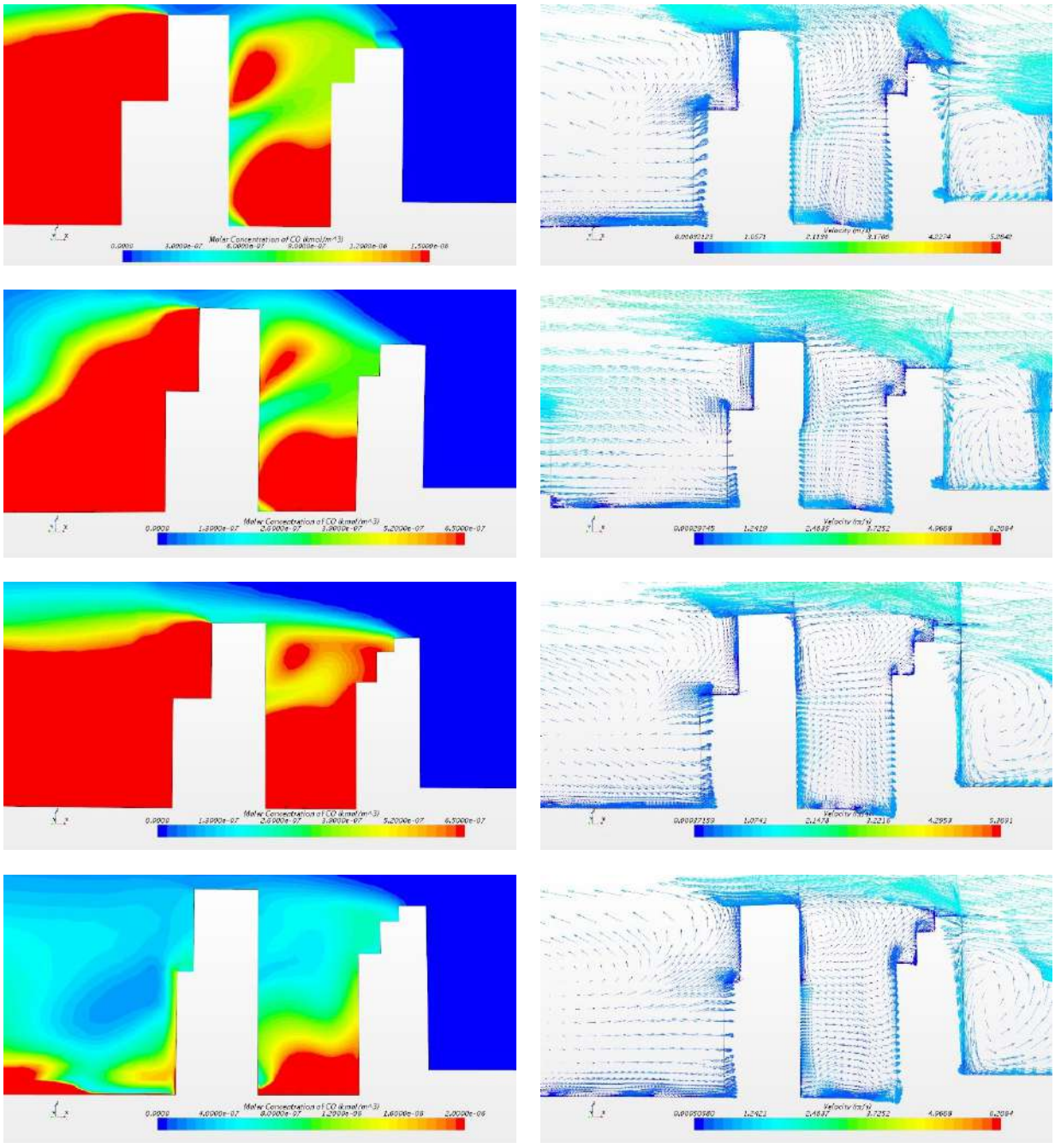

Figure 18: Marconi street, winter cases (from top to bottom): 08/02/2018, 18:00 and 22:00, 09/02/2018, 8:00 and 10:00. CO concentration contours (left) and air velocity vectors (right).

Validation of the simulations – Street canyon with trees

The simulations regarding the canyon with trees have been validated by comparing hourly values as obtained from the numerical simulations with the measurements performed during the two experimental campaigns described in Section 4.1.2 and thoroughly described in D5.2.

Fig. 19 shows the comparison between the simulations and the experimental measurements for Laura Bassi street, during the summer campaign. As described in D5.2, instrumentation for measuring CO concentrations was located on the top of the ARPAE van, while temperature, velocity and TKE were measured over a balcony 9 m high and 1 m distant from the building wall. The measurement stations are described in D5.2. Fig. 19 shows that CO concentrations (top line, first from left) obtained from numerical simulations are overestimated, as numerical values are more than 10 times bigger than measured ones. In particular, the concentration value obtained between 12 and 20 (on 22/08/2017) are more than 10 times the measured one. The distribution of CO on a vertical plane obtained for the case 22/08/2017 at 18:00 is shown in Fig. 20.

The figure shows that, under the tree crowns, a high gradient of CO concentration is obtained. Here it is to note that the ARPAE van probe was placed in that position. We therefore speculate that the pollutant concentration measurements under the trees are very critical. During the night, reduced differences are observed between CO concentrations obtained by CFD simulations and measurements. The temperature obtained by simulations are around 10°C less than those measured in the same position.

This could be explained by an overestimation of the volumetric cooling power assigned to the tree crowns (250 W m^{-3} per LAD unit). Unfortunately, being this cut-edge research, not many works on the subject of no many works heat transfer between trees and environment are available in the literature, and as such further research would be needed to adequately address this issue.

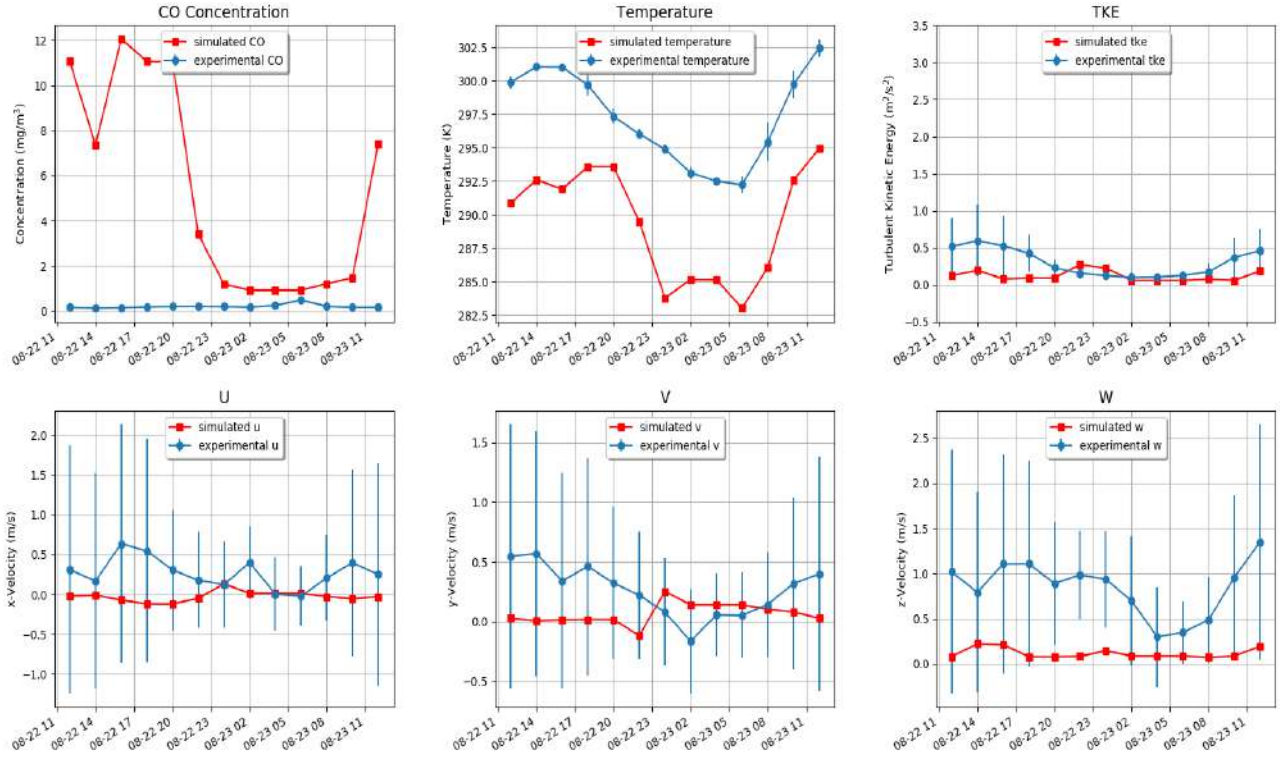

Figure 19: Laura Bassi street, summer. Comparison between numerical results (red) and experimental (blue).

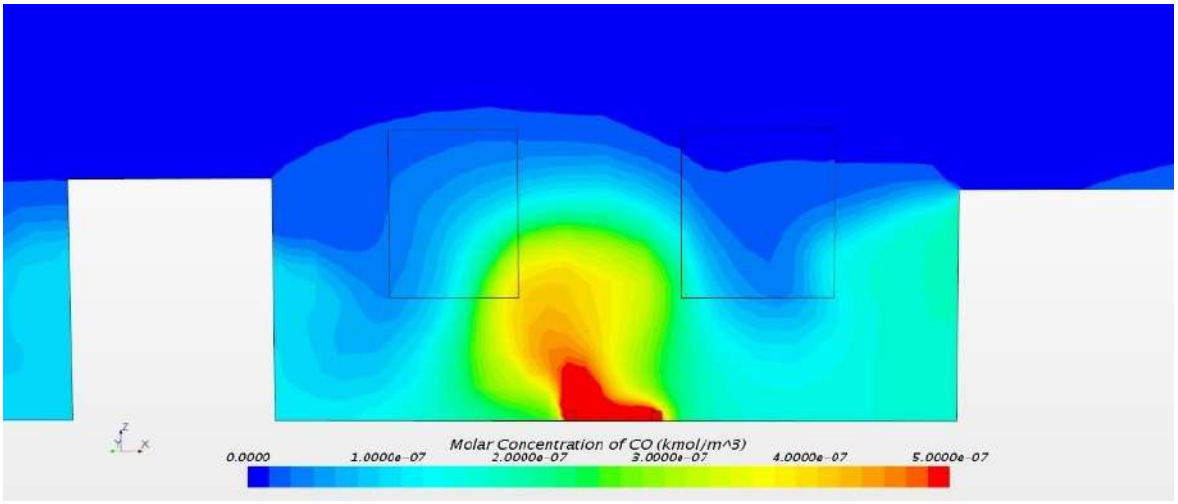

Figure 20: CO concentration contours obtained in Laura Bassi street, summer case: 22/08/2017, 18:00.

Fig. 21 shows the comparison between the simulations and the experimental measurements for Laura Bassi street, during the winter campaign. The figure shows that CO concentrations (top line, first from left) obtained from numerical simulations are in good agreement with the measurements. For the winter case, the concentration values obtained between 12 and 20 (on 08/02/2018) are lower than the measured ones. The numerical temperatures, for these cases, are in very good agreement with the experimental ones. This result confirms the previously supposed overestimation of the plants transpiration cooling: indeed, during winter for which this effect has been neglected the agreement between simulations and observations is far better. A good agreement was also obtained between numerical and experimental velocity components, while numerical values of TKE are higher than experimental ones.

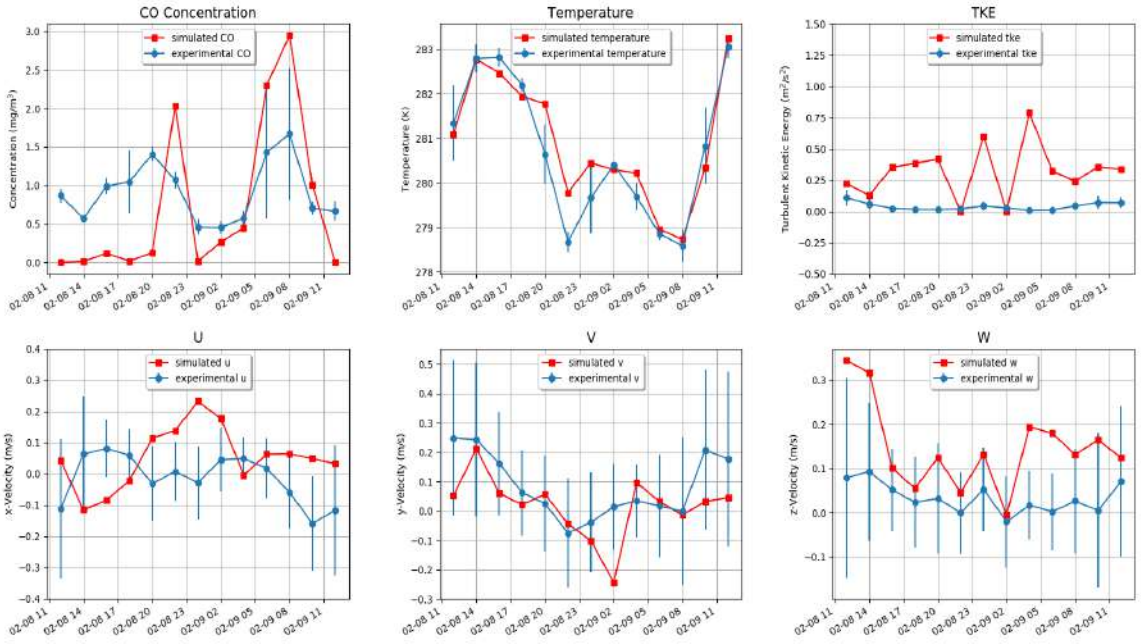

Figure 21: Laura Bassi street, winter. Comparison between numerical results (red) and experimental ones (blue)

2.2 Guildford

The Guildford living lab focuses on GI in open-road environments unlike other cites simulating street canyon conditions. An open road is an urban built environment feature in which both sides of the traffic corridor are open to generally detached single or multi-story buildings (Abhijith et al., 2017) and other manmade structures with fewer obstructions to wind flow result in no flow separation like street canyons. This condition includes locations range from built-up areas (human-occupied) adjacent to high-speed roads as well as peri-urban areas along busy roads.

As a part of D5.2, air quality modifications of three GIs, including hedges, trees and their combinations at six open road locations were investigated around Guildford during May to September 2017 and October to November 2018. The outcomes of this experimental study were submitted as a part of D5.2 and published in peer-reviewed journal (Abhijith and Kumar, 2019) and recent findings will be included in the latest revision of D5.2.

Out of six investigated GI scenarios, hedges reported the highest improvement in the air quality behind the GI in all studied wind directions. One of the monitoring locations with hedge, stoke road site, is located adjacent to a children's park opposite to residential buildings along major feeding road to the Guildford town. Thus, this experimental site has been considered for simulation studies. Simulation studies are emphases on understanding wind flow features and pollutant concentration variations discovered in the field measurements. The scenario analysis is expected to reveal the impact of physical dimensions and densities of hedges on air quality improvement. Hence, the optimised dimensions of hedges lead into generalised recommendations for D7.2 (*Generalised recommendations on PCSs for improving air quality*). Details of field measurements, model set and wind flow analysis are provided in the following sections.

2.2.1 Field measurements and instrumentation

Guildford town is a highly populated area in Guildford Borough, which is a part of Surrey County (Surrey-i, 2015). Guildford Borough has a population of 137,183 as per Surrey-i report in 2015 (Surrey-i, 2015). The most popular mode of transportation is by car that includes about 72% of trips to work and 42% of commute to school (Al-Dabbous and Kumar, 2014). Field experiment considered for modelling investigation consisted of hedges as a primary GI component in a residential area along with the children's park, close to Guildford town centre.

As mentioned before, the monitoring location with hedge was selected for the modelling work and details are shown in Fig. 22. This experimental site has well maintained hedge of 2 m height on the boundary of a children's play area adjacent to a two lanes busy road connecting two major towns Woking and Guildford (Road number A323). The hedge was 36 m long and 1.5 m thick all along the road. Leaf area index (LAI – dimensionless metric of leaf area per unit ground area m^2 m^{-2}) was measured from changes in photosynthetically active radiation passing through overlaying foliage measured by a handheld Ceptometer (Meter Environment, ACCUPAR LP80). The hedge has an LAI of 6.64 m^2 m^{-2}. The dimensions and LAI of all trees and hedges around the monitoring location were used for recreating the domain in the model. Average LAD estimated from the measured LAI and height of trees and hedges were 0.63 and 2.62 m^2 m^{-3}, respectively.

Figure 22: Details of the modelling domain from the experimental site, stoke park, Guildford. (a) Guildford town, the red circle shows the measurement site, b) highlighted circle shows area of interest, (c) red dots show monitoring locations, and (d) street view of the hedges at stoke park.

In this work, collected $PM_{2.5}$ data for model validation and detailed description of the experimental setup and monitoring protocols are provided in the D5.2. $PM_{2.5}$ concentration was measured by two GRIMM aerosol monitors, model EDM 107 and 11-C at a height of 1.5-1.7 m in front of the hedge and behind the hedge (Fig. 22c and 22d). Local meteorological conditions (air temperature, relative humidity, wind speed and direction) were logged by a portable weather station (Kestrel 4500) close to the hedge at 1-min resolution. In addition, meteorological conditions during the monitoring periods were obtained from the nearest UK weather station, located in Farnborough (~10 km North-West of Guildford). Comparison of the two measurements that provide local variation in wind direction and speed close to the hedge is shown in Fig. 23. Parallel to the road and perpendicular were two main wind directions during the measurement campaign. These wind data was sieved to generate log-wind profiles for mode input. Traffic counting was performed by using the SMART Traffic Counter App developed by University of Wollongong, Australia. Traffic was counted in the first 20 minutes of an hour and extrapolated to an hour to estimate hourly average traffic volume. The emission factors for $PM_{2.5}$ was estimated from this traffic data. The campaign was 5 days long and started and ended around 8:00 h and 18:00 h (local time) every day. No field measurements were carried out on rainy days.

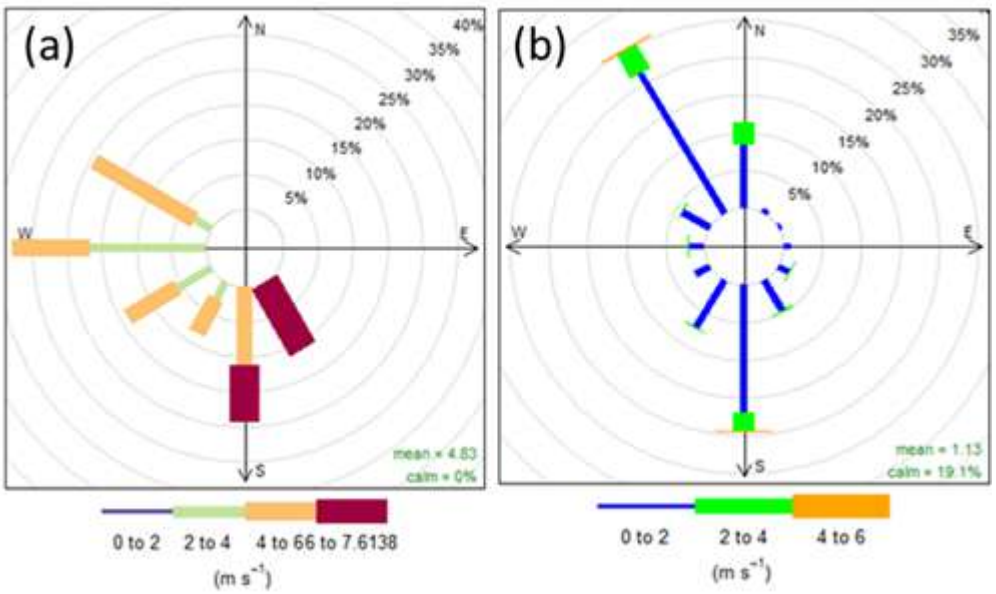

Figure 23: Comparison of wind data, meteorological weather station and portable weather station, at 1.5 m at monitoring site and 10 m height at meteorological site. Frequency of counts by wind direction of Metoffice monitoring site (a), and stoke road site (b).

2.2.2 Numerical setup and simulations

A CFD modelling tool, ANSYS FLUENT version 19.1, was used to simulate wind flow and dispersion of $PM_{2.5}$ in the open-road conditions at Stoke Park. Steady-state Reynolds-averaged Navier-Stokes (RANS) equations with realizable k-ε turbulence model were considered. Model geometry was created (as shown in Fig. 24) in ANSYS Workbench following the best practice guideline provided by the COST (Franke et al., 2007) and AIJ (Tominaga et al., 2008) guidelines as summarized in Table 10. The total dimension of the model was 416 m x 260 m x 117m (L x W x H). The total stream wise length of the domain was 416 m (32 H, H=13 m), which had an approach length of 8 H, a model region of 6H x 6H x 8H, and downwind length 18 H (Fig. 25). It consisted of lateral extension of buildings, and the upper boundary from roof of building according to the guidelines. Two wind directions were considered in this work as shown in Fig. 25. Building and GI shapes were simplified as cuboid similar to other CFD investigations (Amorim et al., 2013; Buccolieri et al., 2011; Gao et al., 2018; Garcia et al., 2013; Gromke et al., 2016; Moradpour et al., 2016). The stem of the trees was omitted in the geometry similar to previous studies (Abhijith and Gokhale, 2015; Buccolieri et al., 2011; Wania et al., 2012). Default program controlled assembly meshing of tetrahedral grid was applied for the special discretization of the computational domain. The size of the elements on building and GI was 0.1 m and the domain had 7.7 million elements in total. The grid size was increased with an expansion ratio of 1.1. Meshing face sizing was used for buildings, sources and GI to ensure finer grid resolution in the region of interest. ANSYS workbench was used to make mesh generation.

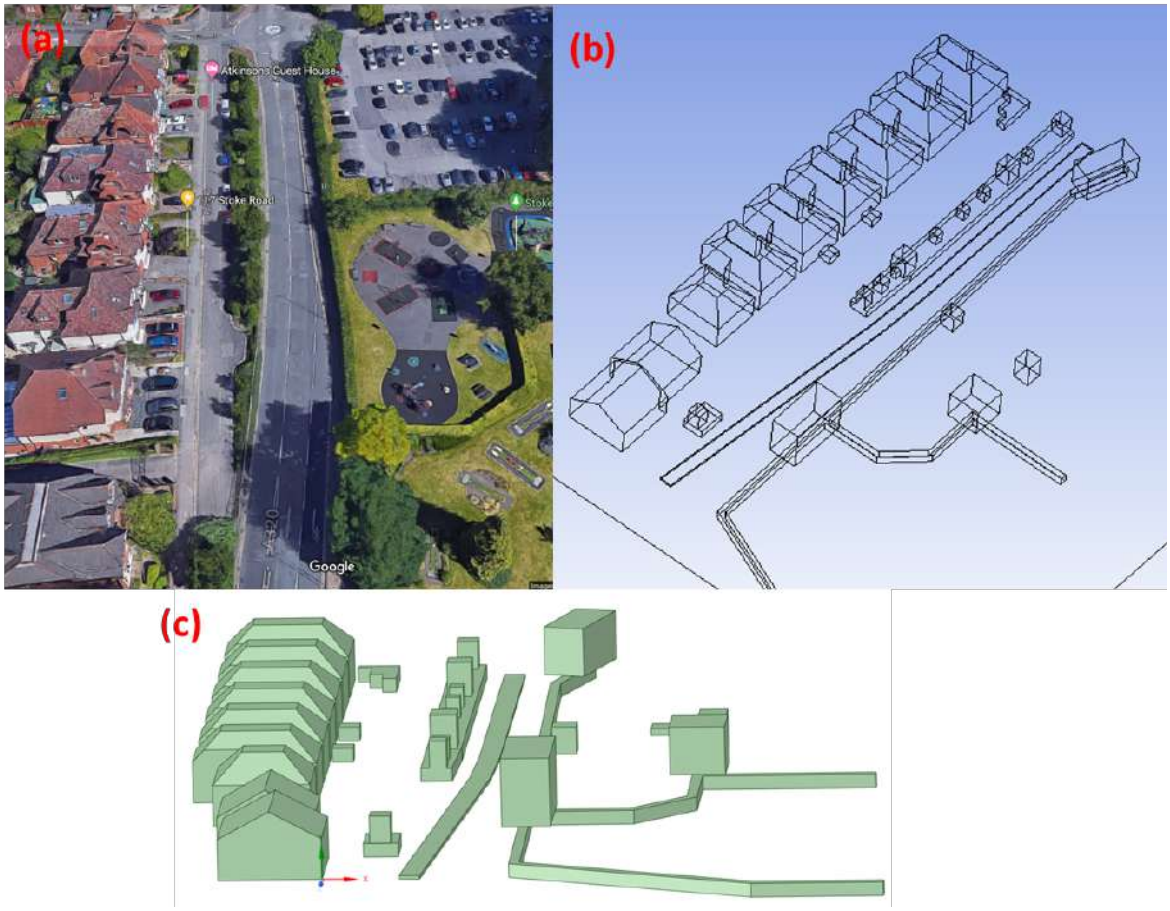

Figure 24: Modelled geometry in Workbench (a) real geometry, (b and c) line sketch of simplified geometry.

Inlet wind flow conditions were prescribed based on the meteorological data collected at the site and from met office. Richards and Hoxey's (1993) vertical profile equations for variables in the velocity, TKE (k) and dissipation rate (ε) with height were used and neutral stability conditions were assumed. Temperature was kept uniform in the domain and gravity was applied.

$$u(z) = \frac{u_*}{k_v} \ln\left(\frac{z+z_0}{z_0}\right) \quad (17)$$

TKE and dissipation rate profiles were specified as according to:

$$k = \frac{u_*^2}{\sqrt{c_\mu}} \quad (18)$$

and

$$k = \frac{u_*^2}{\sqrt{c_\mu}} \quad (19)$$

z is vertical position above the ground, z_0 the roughness length in the computational domain, u* the friction velocity, κ_v=0.42 the van Karman constant, C_μ=0.09 and δ the height of the computational domain. These parameters were incorporated into the model using a User-Defined Function (UDF) resulting the wind flow conditions of the experimental site.

Parameter	COST guidelines (Franke et al., 2007)	AIJ guidelines (Tominaga et al., 2008)
Domain size		
Lateral and top boundary extension	5H	5H (H= tallest building)
Out flow from building	15H	10H
Grid discretization		
Grid resolution		1/10 of building scale
Expansion ratio	1.2 to 1.3	≤ 1.3
Evaluation height from ground surface		3rd or higher grid
Min grids on building face	10	10
Grid dependence study		
No of refined grids for comparison	Richardson exploration or two grid comparison	At least 3
Ratio of two consecutive grids		3.4
Improvement of unstructured grids (tetrahedral elements)	Use of prismatic element	Use of prismatic element
Boundary conditions		
Inflow-equations	Richards and Hoxey (1993), or wind tunnel	Tominaga et al., (2008).
Side and top	Constant shear for top, symmetry condition for sides	Normal components zero
Outflow	All variable zero	All variable zero
Building surface	No slip condition	Logarithmic law of smooth wall or wall with specified roughness
Scheme for convection terms	Second order upwind scheme	Second order upwind scheme
Convergence criteria	Residuals of at least four order of magnitude and constant or oscillatory residual of target variable	Monitoring variables on specified points or overlapping the contours results at different calculation steps.
Initial condition	With a data having least uncertainty	Laminar or appropriate conditions

Table 11: Summary of best practice guidelines.

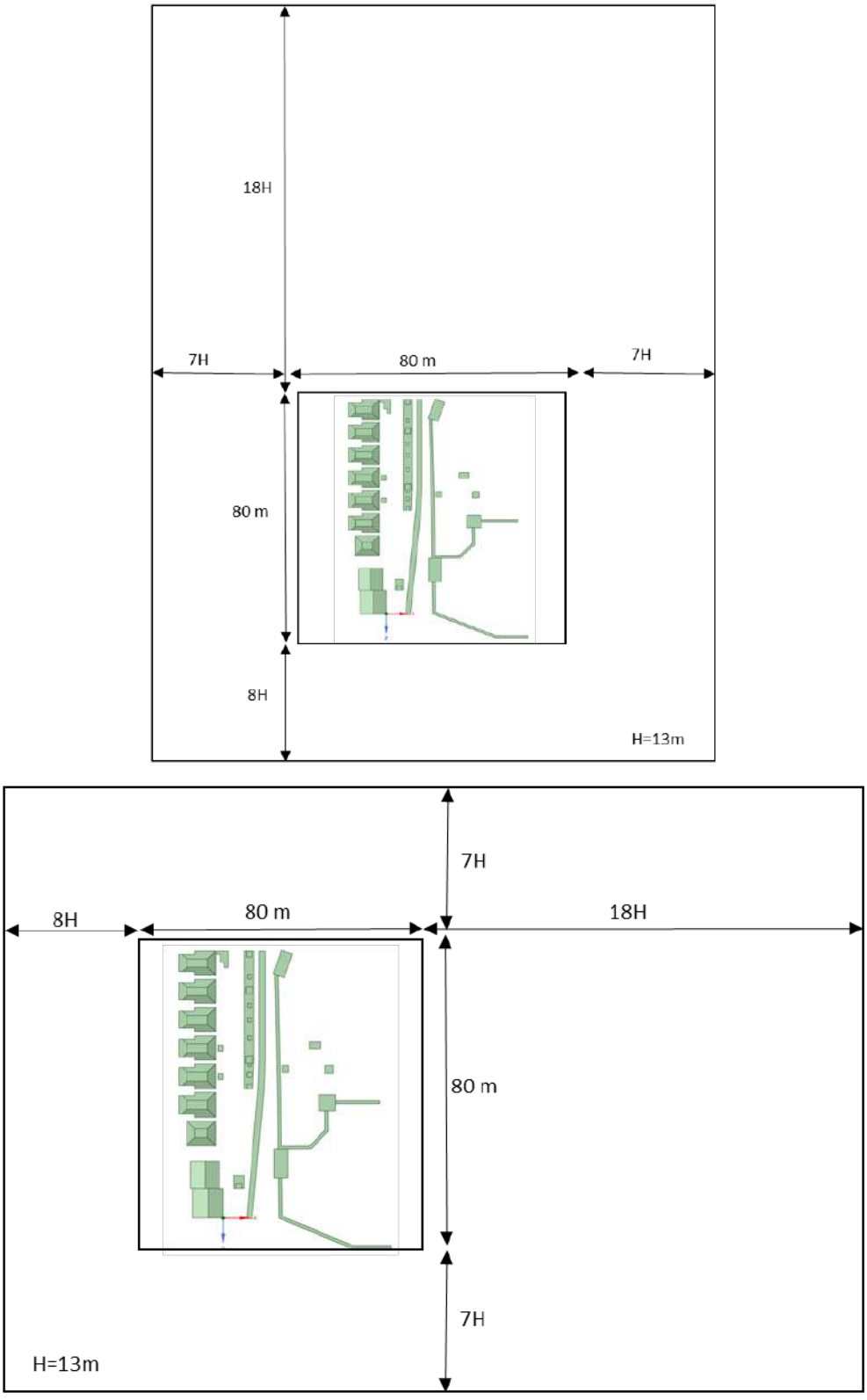

Figure 25: Model dimensions in along the road wind (top) and cross-road wind flow conditions (bottom).

No-slip wall boundary condition was imposed along the top, bottom and lateral boundaries of the domain. The same boundary condition was applied to the surfaces of the building as per the guidelines listed in Table 10. All walls were considered impermeable for species transport. In FLUENT 19.1, the surface roughness was expressed in terms of a sand grain roughness instead of the aerodynamic roughness as is the case in most meteorological codes. In order to circumvent problems with a coarse grid resolution near the ground due to a large sand grain roughness value, Gromke et al. (2008), Gromke and Ruck (2009), and Buccolieri et al. (2011) studies set equal to the aerodynamic roughness length, which was taken as 0.1 m. Previous real-world studies adopted roughness length of 0.003 to 1.1 m depending upon the site specific meteorological conditions (Amorim et al., 2013; Hofman et al., 2016; Moradpour et al., 2016; Sanchez et al., 2017; Santiago et al., 2017). A zero diffusive flux was imposed on the outflow boundary.

$PM_{2.5}$ were introduced in the model along the street as a particle emitting normal to surface at 0.5 m height along the street using a Lagrangian approach in FLUENT (Garcia et al., 2013). The dispersion model consists of a second phase of spherical inert particles in a Lagrangian frame of reference. The initial velocity of particles was kept zero, assuming no traffic induced turbulence. Emission rates were calculated based on the traffic counts taken during the field campaign.

Realizable turbulence model of ANSYS FLUENT 19.1 was employed to obtain solutions. Species transport equations were utilized for air-$PM_{2.5}$ mixed flow simulation. Second order upwind numerical scheme was selected. SIMPLE scheme was used for pressure-velocity coupling. Combined termination criteria were used. Scaled residuals were kept at and monitoring points of concentration of $PM_{2.5}$ and velocity magnitude were assigned in the domain, iterations were carried out till constant values were shown in monitoring points and residuals reached a desired level. After completing all the above steps, the results were taken out using CFD-POST and "solutions" in FLUENT, various statistical comparisons and analysis were performed to derive results.

GI modelling

The tree canopies were simulated by creating rectangular blocks in the geometry and defining them as porous zone with a pressure loss coefficients and porosity. In FLUENT, porous media are modelled by the addition of a momentum source term (actually a sink) to the standard fluid flow equations. The source term is composed of two parts: a viscous loss term and inertial loss term as shown in the equation (20).

$$s_i = -\left(\sum_{j=1}^{3} D_{ij}\mu v_j + \sum_{j=1}^{3} C_{ij}\frac{1}{2}\rho|v|v_j\right) \quad (20)$$

Where S_i is momentum sink term, $|v|$ magnitude of the velocity, D (m^{-2}) and C (λ) (m^{-1}) are pressure loss coefficients. The viscous resistance is neglected in flow modelling through the tree crown because it was considered much smaller than the inertial resistance (Balczó et al., 2009; Buccolieri et al., 2009; Gromke et al., 2008; Li et al., 2013). The viscous part of the equation was eliminated by taking zero value for D. The real tree canopy porosity expressed in volume fraction roughly varied from 93% to 99% (Zhou et al., 2002). The porosities used in wind tunnel simulations were 97.5% and 96% with coefficients 200 m^{-1} and 80 m^{-1}, respectively (Buccolieri et al., 2009 and 2011; Gromke et al., 2008; Gromke and Ruck, 2009 and 2012; Salim et al., 2011a and b). Whereas in real-world conditions, pressure loss coefficients are calculated as follows (Buccolieri et al., 2018):

$$\lambda = LADC_d \quad (m^{-1}) \quad (21)$$

C_d values were taken as 0.25 (Buccolieri et al., 2018; Jeanjean et al., 2016). Average LAD values were 0.63 and 2.62 for trees and hedges, respectively, resulting in pressure loss coefficients of 0.1575 m^{-1} and 0.655 m^{-1}, respectively. Similar modeling methods for GI were employed in previous studies (Di Sabatino et al., 2015; Xue and Li, 2017).

$$S_k = \rho LAD C_d\left(\beta_p U^3 - \beta_d U k\right) \quad \text{(kg m}^{-1}\text{ s}^{-3}\text{)} \quad (22)$$

$$S_\varepsilon = \rho LAD C_d\left(C_{\varepsilon 4}\beta_p \frac{\varepsilon}{k} U^3 - C_{\varepsilon 5}\beta_d U \varepsilon\right) \quad \text{(kg m}^{-1}\text{ s}^{-4}\text{)} \quad (23)$$

Where $0 \le \beta_p \le 1$ is the fraction of mean kinetic energy converted into TKE by means of drag, β_d is the dimensionless coefficient for the short-circuiting of the turbulent cascade, $C_{\varepsilon 4}$ and $C_{\varepsilon 5}$ are model constants. Several values of these parameters can be found in the literature. In this work $\beta_p=1$, $\beta_d=4$ and $C_{\varepsilon 4}=C_{\varepsilon 4}=1.5$ values obtained from Buccolieri et al. (2018) and Amorim et al. (2013) studies have been used.

Modelling of pollutant removal due to vegetation is carried out by introducing a sink term. The pollutant flux S_d (g m^{-2} s^{-1}) is calculated as the product of the dry deposition velocity V_d (cm s^{-1}) and pollutant concentration c (g m^{-3}) as listed in (Buccolieri et al., 2018):

$$S_d = -LAD V_d c \quad (24)$$

V_d value depends on the type of vegetation and 0.64 m s^{-1} was taken from the previous studies (Al-Dabbous and Kumar, 2014; Baldauf, 2016; Jeanjean et al., 2016, 2017).

2.2.3 Investigated PCS scenarios

Optimized GI dimensions and characteristics for D7.2 are developed through scenario analysis. GI impacts on air quality under different meteorological conditions are being analysed and the influence of height and width of hedges is being simulated. Two wind directions and wind speeds (from 2.5 to 8 m s^{-1}) have been considered. The heights used for simulations are 1, 1.5, 2, 2.5 and 3 m, whereas width varied from 0.75 to 2.5 m. The GI density of LAD are varied from 1-5 m^2 m^{-3} as reported by Buccolieri et al. (2018). The outcomes of this scenario analysis will be reported as generalized solutions in D7.2.

2.3 Dublin

The Dublin living lab focuses on the pollution concentration from vehicular emission inside a street canyon. The selected street canyon is located at the Dublin city centre, where the pollution is found to be high. This study develops a computational fluid dynamics (CFD) based simulation study by considering real world measures pollution data (NO_x and NO concentration), meteorological data (wind speed and wind direction) and traffic volume data. Simulation studies examine the changes in pollution concentration inside the street canyon with and without the presence of hypothetical low boundary walls as passive control structure. The section is structured as below: Section 2.3.1 provide details on the chosen study area, section 2.3.2 provides details on the field measurement data and their characteristics, section 2.3.3 describes the details on the developed CFD model and the setup and the section 2.3.4 provides the location details on the hypothetical low boundary walls.

2.3.1 Site description

This study focused on determining the effectiveness of different forms of passive controls to reduce personal exposure to vehicular pollutants. The study has been adapted from Gallagher (2013a). A

CFD model was constructed to replicate a section of Pearse Street in Dublin (Fig. 26), a busy urban street canyon with four lanes of traffic (circa 1500 vehicle hr^{-1} peak traffic). The model was calibrated using measurements of local meteorological conditions, on-street pollutant concentrations and traffic count data. The potential reduction in personal exposure to a specific air pollutant primarily sourced from vehicle emissions (nitrogen monoxide or NO) was calculated between the current street layout without passive controls and a subsequent scenario including passive control in the canyon. NO is a reactive pollutant and to minimize the conditions suitable for these reactions to take place, the street was monitored for NO_x concentrations during winter conditions (Huang et al., 2008; Parra et al., 2010). Lower temperatures in the street also increase thermal stability and reduce dispersion (Oke, 1988; Jicha et al., 2000; Santese et al., 2007; Huang et al., 2008). The study assessed the influence of LBWs placed along the edge of both footpaths in Pearse Street.

A detailed analysis of real-time data was carried out initially to identify trends and correlations between varying traffic volumes and compositions, pollutant concentrations and meteorological conditions. The study assessed the effect of wind speed and direction on pollutant dispersion and the development of vortices within the canyon, which have been found to influence air flow patterns significantly by previous researchers (De Paul & Sheih, 1986; Hoydysh & Dabberdt, 1988; Crowther & Hassan, 2002). Manual traffic counts were taken to establish an understanding of the different traffic flows in each of the traffic lanes during peak and off-peak times of the day. NO_x concentrations were also monitored at a selected location in the street. This data was used in the calibration of the model after a detailed analysis of the relationship of the pollutant concentration to traffic emissions and meteorological conditions.

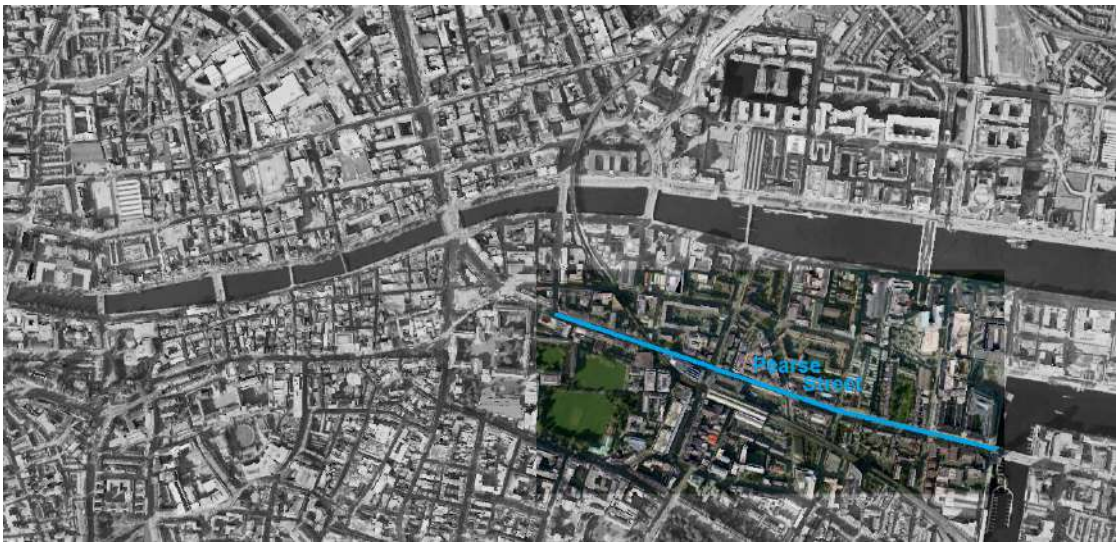

Figure 26: Pearse Street in Dublin City Centre obtained from Google Earth.

The objective of this study was to construct a calibrated model of Pearse Street to validate the potential of passive controls. The model was constructed from shapefiles of the buildings on Pearse Street sourced from Dublin City Council (DCC) using geographical information system (GIS) data.

The initial reference model was constructed based on the current Pearse Street layout. After this model was calibrated, the subsequent passive control models containing LBWs were developed. The reference model was calibrated using the combined data collected for traffic volumes, NO concentrations in the street canyon and local wind parameters. The conditions were replicated

in the passive control models and results were compared to the reference model. The models were solved using the Large Eddy Simulation (LES) turbulence model for different traffic flows, wind conditions and passive control configurations. The LES model has been previously used to successfully simulate air flow and pollutant dispersion in a real street canyon environment (Liu et al., 2011, Gallagher et al, 2011, 2012, 2013b).

Air pollutant concentrations were measured on the footpaths in the CFD models and the improvements or deteriorations in air quality were calculated between the reference and passive control models. The concentration values of air pollutants obtained based on the reference and passive control model were compared to yield the percentage difference between each model. The airflow in the modelling study was simulated from the flow of air over the top of the buildings and at either end of the street section by the velocity inlets. Velocity inlet properties were attached to different faces of the model depending on the direction of the prevailing wind. The relationship between the inlet velocity parameters and the measured wind speed and direction measured around Pearse Street was determined as part of the calibration process. The dispersion of NO in the turbulent air stream from traffic was simulated by releasing concentrations of the gas at street level. The emissions were represented as a surface source across each of the traffic lanes and were released after the initial development of vortices in the canyon. Fig. 27 displays the reference model layout and the boundary surfaces in the model and their associated characteristics.

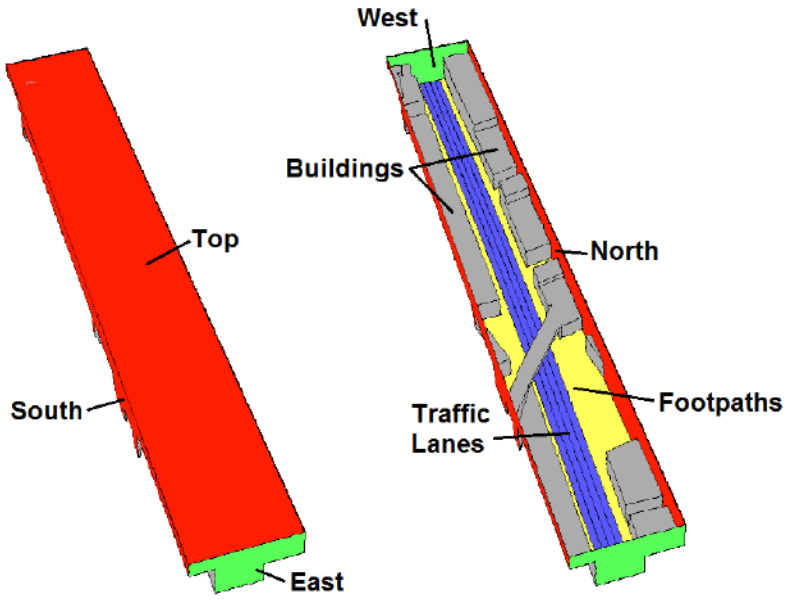

Figure 27: Display of (a) closed and (b) open fluent models.

2.3.2 Field measurements and instrumentation

NO_x measurement

NO_x concentrations were measured for two weeks in December at a selected location (Fig. 28) in Pearse Street to allow for the calibration of the model. Total NO_x and NO were measured using a Chemiluminescent $NO/NO_2/NO_x$ Analyser (Model 200EU) and NO_2 was calculated as the difference between the two concentrations under ISO 7996: 1985 standards (CEC, 1999). The NO_x analyser was located on the North side of the street on the 3rd floor of a building (Fig. 28).

This was considered a suitable location to monitor the pollutant concentration in the air flow of the canyon, as the zone was of a less turbulent nature than at street level. Therefore, it was considered that the data collected would be more stable and could allow the calibration of the model to be more accurate. Measurements of NO_x concentration are generally an overestimation of pollutant emissions during the summer months (Jensen et al., 2009). Therefore, the measurement of NO_x in winter conditions with low levels of solar radiation and low temperatures can allow an accurate representative measurement of NO_x sourced from vehicle emissions (Gualiteri & Tartaglia, 1997; Huang et al., 2008). This removed the complexity of modelling pollutant reactions in this study.

Figure 28: NOx (Red) and Wind (Blue) monitor locations on Pearse Street.

Wind data

Local wind speed and direction was measured using a Model 05103L wind anemometer and CR200 series data logger at an elevation of 19.3 m above street level, located on the roof of a building on Pearse street, as shown previously in Fig. 28. The instrument location (Fig. 29) was chosen as it was one of the highest points along the street canyon and therefore accurate measurements of wind speed and direction over the street could be recorded.

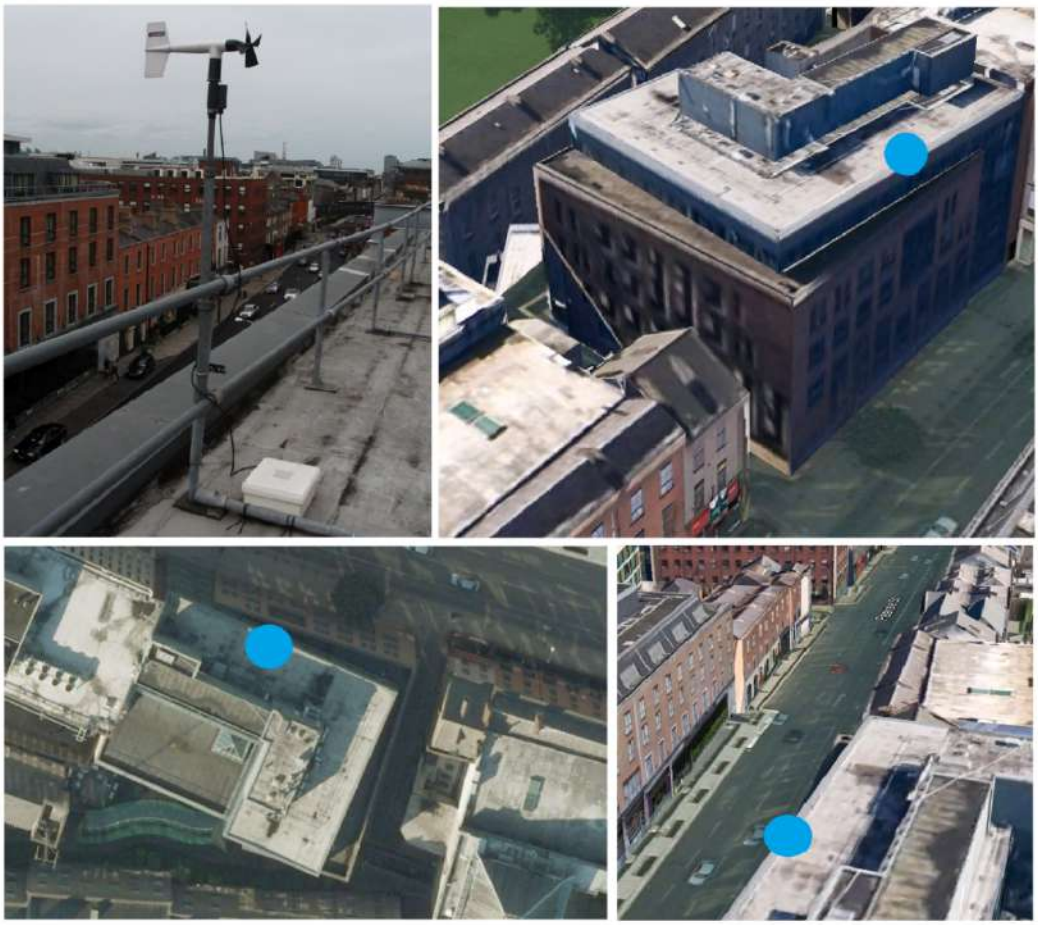

Figure 29: Wind Anemometer (Blue) on Pearse Street Rooftop.

The anemometer was set-up above the urban canopy layer (UCL) i.e. above the mean building height in the area (Oke, 1988). The data collected at the selected location was therefore considered to be in the inertial sub-layer (ISL), which suggests a reduced influence on wind data incurred by roughness from building rooftops (Oke, 2006). This was to improve the accuracy of the measured wind data parameters over the street canyon which conforms to guidelines in the report by the World Meteorological Organization (WMO) WMO/TD-No. 1250 (Oke, 2006). Wind measurements were collected at 5-min intervals for the duration of the pollutant monitoring period. This data was then averaged to 15-min intervals to correspond with the NO_x measurements and traffic data for calibration purposes.

Traffic counts

Traffic data was acquired from two sources; (i) manual data collection of traffic volumes on Pearse Street for individual lane traffic counts and (ii) DCC's intelligent transport system which is known as Sydney Coordinated Adaptive Traffic System (SCATS) which continuously monitors traffic flows in Dublin (NRA, 2010). The use of these combined methods of traffic data collection was to ensure the accurate measurement of fleet composition and distribution by the automated system SCATS. This ensured an accurate estimation of the average ER for each lane based on

identifying the different fractions of vehicle categories, similar to a previous investigation by Huang et al. (2008).

	Survey Information	Peak Traffic Times		Off-Peak Traffic Times	
		Morning 08:00 – 09:00	**Evening 17:00 – 18:00**	**Morning 11:00 – 12:00**	**Evening 19:00 – 20:00**
A	Date	6th December	6th December	5th December	6th December
	Traffic	1898	2467	1516	1862
	Weather	Overcast	Recent Shower	Sunny, No Clouds	Recent Shower
	W. Direction	East	South-West	East	South-West
	W. Speed	25 km h^{-1}	24 km h^{-1}	26 km h^{-1}	24 km h^{-1}
	Temperature	4 °C	6 °C	2 °C	4 °C
B	Date	7th December	7th December	6th December	12th December
	Traffic	1942	2728	1695	1661
	Weather	Sun	Fair	Sun & Cloud	Raining
	W. Direction	West	West	South-West	South-West
	W. Speed	33 km h^{-1}	33 km h^{-1}	24 km h^{-1}	20 km h^{-1}
	Temperature	3 °C	5 °C	4 °C	9 °C
C	Date	8th December	13th December	7th December	13th December
	Traffic	2012	2636	1720	2115
	Weather	Light Rain	Fair	Sun	Fair
	W. Direction	South-West	South-West	West	South-West
	W. Speed	41 km h^{-1}	39 km h^{-1}	33 km h^{-1}	39 km h^{-1}
	Temperature	9 °C	2 °C	5 °C	9 °C
D	Date			8th December	
	Traffic			1895	
	Weather			Recent Rain	
	W. Direction			South-West	
	W. Speed			41 km h^{-1}	
	Temperature			8 °C	

Table 12: Traffic survey data for Pearse Street, Dublin.

The vehicles were categorised as (i) light vehicles including motorcycles, (ii) medium and large vehicles, (iii) buses and (iv) cyclists. The manual traffic data was collected at random peak and off-peak times during the pollutant monitoring period to record data in different weather conditions. A summary of the data collected from the manual traffic counts and the corresponding weather data obtained from Met Éireann (www.met.ie) is displayed in Table 11.

A total of fourteen individual traffic counts took place during the monitoring period. The traffic data was collected by carrying out simultaneous manual counts for each of the four traffic lanes, distinguishing the fleet composition and the fractions of the total traffic that are in each of the lanes. Table 11 summarises the data collected from the traffic count for each count and additional information which was collected from the Met Éireann for local weather forecasts for the Dublin region. A significant variance for each of the weather parameters can be observed from Table 11 throughout the monitoring period. This underlines the complexity of the data collected with respect to the development of a calibrated model for Pearse Street.

A detailed analysis of the data collected for each of the parameters was carried out individually prior to the calibration of the Pearse Street model. This was to assess the validity of each of the data sets and to investigate unusual events, which were not considered to fit within the standard cyclic patterns of hourly, daily or weekly routine. The correlation of traffic emissions to measured

pollutant concentrations was initially considered to be relatively straightforward prior to the analysis carried out in this section. However, as Fig. 30 displays, the correlation between these two parameters in parallel and perpendicular wind conditions can be more complex than expected. Therefore, during the calibration process, a number of different parameters that vary over time will need to be considered.

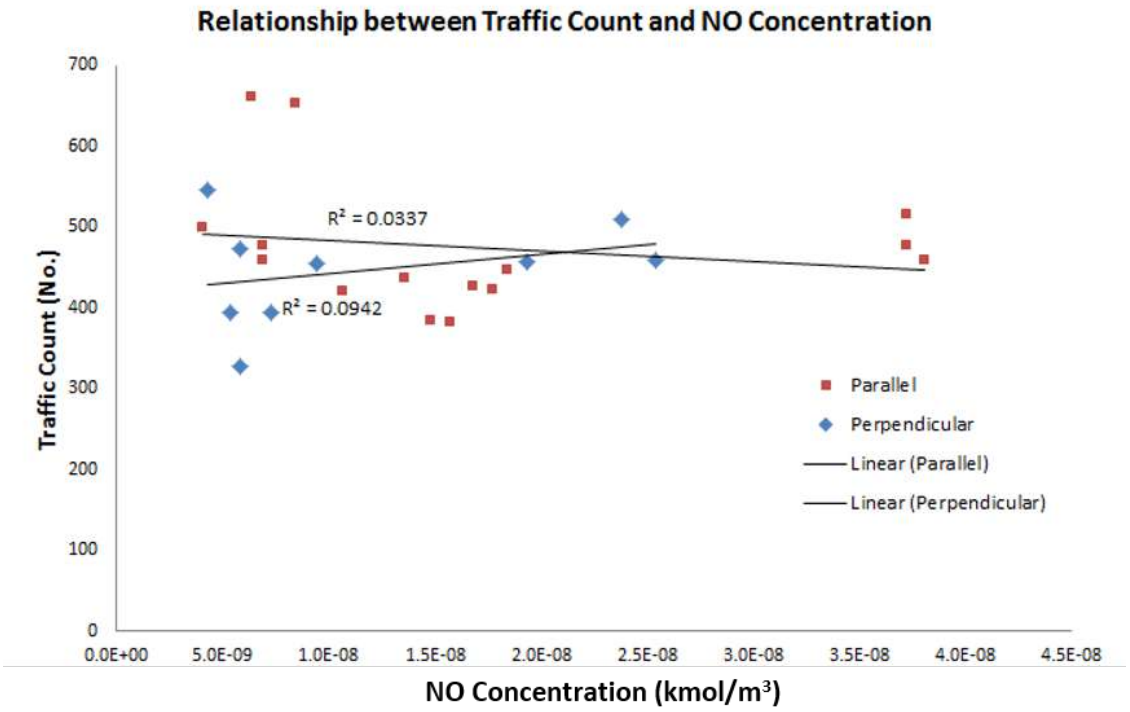

Figure 30: Plot of NOx concentration against Traffic Data on Pearse Street.

A diurnal plot of the NO concentration is represented in Fig. 31, which shows the average daily, weekday and weekend concentrations during the monitoring period.

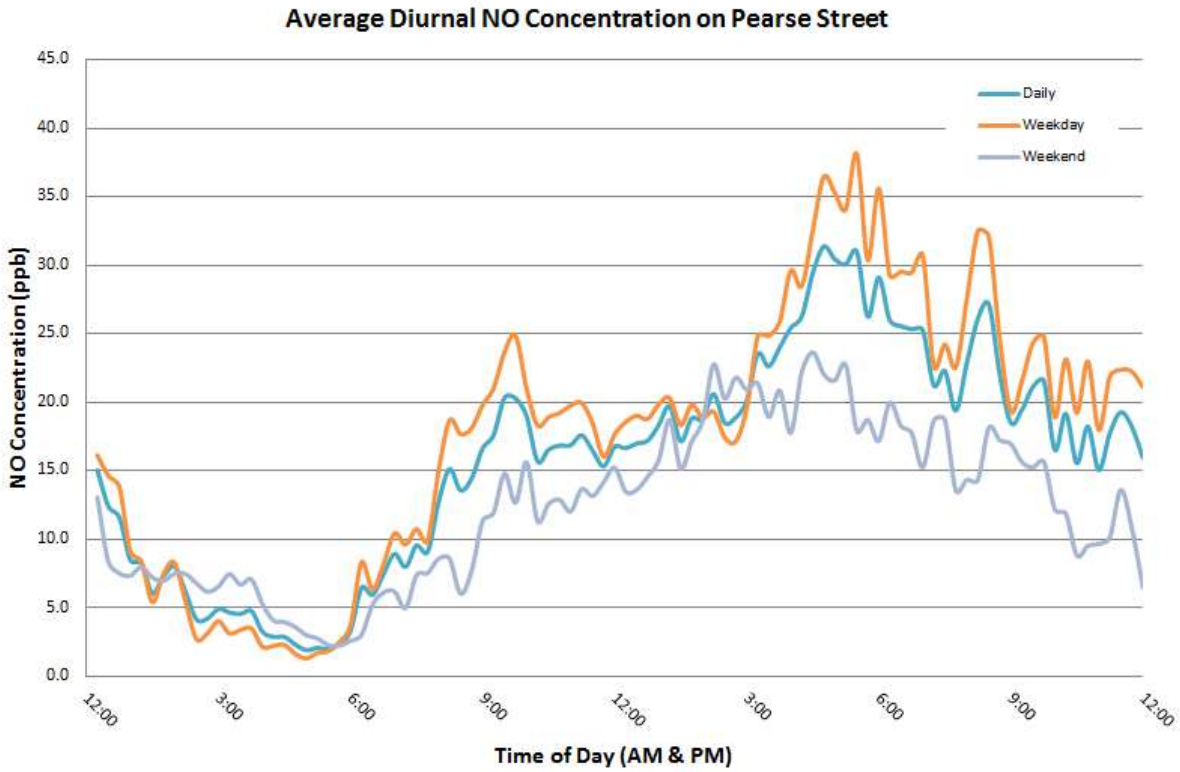

Figure 31: Plot of daily NO concentrations.

An analysis of the figure identifies the common trend for the daily NO concentrations in Pearse Street. A gradual reduction of NO is observed from midnight (00:00 am) to the early hours of the morning (5:00 - 6:00 am). This is followed by a sharp increase during the morning period (6:00 - 10:00 am), with a gradual levelling out of NO concentrations in the later morning through to mid-afternoon (10:00 am – 3:00 pm). A steady increase can be viewed (3:00 - 5:00 pm) until peak evening traffic (5:00 – 7:00 pm) followed by an ultimate steady reduction in the NO concentration towards midnight (7:00 pm – 12:00 am).

Pearse Street contains of four lanes of one-directional traffic. Typical road users use the same route (a two-directional street) in the morning and evening to travel to and from a place of work, residence or other activity. If the NO concentrations are considered to be associated with Pearse Street traffic volumes, then the majority of road vehicles use Pearse Street solely during the evening.

The additional plots in Fig. 31 for NO shows the clear difference between the average weekday and weekend concentrations. This is considered to be due to an increase in traffic volumes during weekdays compared to weekend or Sunday traffic, which was also noted in investigations by Ghenu et al. (2008), Broderick et al. (2006) and Wehner et al. (2002). The NO data collected during the monitoring period and which correspond to the times of the manual traffic counts are summarised in Table 12.

(μg m^{-3})	Peak Traffic Times	Off-Peak Traffic Times

		Morning 08:00 – 09:00	Evening 17:00 – 18:00		Morning 11:00 – 12:00	Evening 19:00 – 20:00
Total	Min.	1.3	6.7		6.0	3.8
	Avg.	14.9	30.3		16.5	22.2
	Max.	38.9[a]	111.4[a]		37.0[a]	76.2[a]
Week 1	Min.	1.3	8.7		6.4	6.1
	Avg.	16.5	22.0		13.9	15.4
	Max.	38.9	37.0		24.2	35.5
Week 2	Min.	1.8	6.8		6.5	3.8
	Avg.	14.0	38.2		17.3	26.0
	Max.	18.3	111.4[b]		37.0	76.2[b]

[a] Denotes concentrations which lie outside the 95th percentile (average ± two standard deviations) of the respective data sets.
[b] Evening concentrations during week 2 which are significantly higher from equivalent week 1 concentrations.

Table 13: Summary of NO monitoring data on Pearse Street.

Comparison of the relatively small data set collected manually by carrying out traffic counts of Pearse Street with the SCATS data over the entire monitoring period were performed and shown in Table 13.

	Manual Data					SCATS Data*			
	L1[a]	L2	L3	L4		L1[a]	L2	L3	L4
Min.	29	177	141	0		1	127	151	8
Avg.	75	215	199	56		38	200	204	66
Max.	102	270	247	143		442	248	248	175

* The Shaw Street traffic was equally divided evenly over the four lanes to simplify this comparison.
[a] Bus Lane.

Table 14: Comparison of manual and SCATS traffic data for Pearse Street.

The table indicates that the difference in average traffic count for the three lanes L2-L4 are considerably less, though there is a difference in average traffic count for the bus lane L1. Furthermore, the slope of the regression relationship developed between traffic counts based on manual data and SCATS data for Lanes L2-L4 were found to be 1.04, which is very close to unity. This would suggest that that there is very little difference between traffic numbers measured by both the manual and SCATS systems for three of the four lanes.

Despite the strong correlation between the data sets for three of the four lanes of traffic, there was some concern for the use of SCATS data to predict a relationship between NO_x concentrations and traffic emissions. During the model calibration process, the manual traffic information was used as much as possible as it provided more accurate information for both the traffic lane distribution and the vehicle composition. In scenarios where the SCATS data was used (to ensure the data sets were large enough to identify trends), the traffic data for Lane 1 was estimated only when manual data had been collected i.e. the four 1-hr periods during weekday. This was considered essential for the accurate allocation of specific emissions rates along each of the traffic lanes in Pearse Street.

Evaluation of the composition of the traffic fleet carried out in Pearse Street is presented in Table 14 and Fig. 32. An examination of the results in the table shows that in the behaviour of the traffic during peak and off-peak times of the day, some common trends are evident with regards to changes in the vehicle composition on Pearse Street.

The highest fraction of light vehicles occurred during off-peak periods in the day. Large vehicles were primarily using Pearse Street during the morning (both at off-peak and peak times) as there were approximately 3-4 times the number of these vehicles on the road in the evening period. The fraction of buses remained relatively constant (average of 2.0%) as a fraction of the total traffic, but a small increase was observed in the morning period, at the peak morning traffic time (2.4%) in particular. The percentage of cyclists varied throughout the day (from 2.6% to 7.9%) with the most significant fraction of cyclist numbers (7.9%) accounted for during the evening peak traffic time.

Vehicle Category	Average	Peak Traffic Times		Off-Peak Traffic Times	
		Morning 08:00 – 09:00	Evening 17:00 – 18:00	Morning 11:00 – 12:00	Evening 19:00 – 20:00
Light	91.3%	90.3%	89.8%	93.3%	91.8%
Med/Large	1.2%	1.7%	0.6%	1.9%	0.5%
Bus	2.0%	2.4%	1.7%	2.1%	1.9%
Cyclist	5.5%	5.6%	7.9%	2.6%	5.9%

Table 15: Percentages of fleet composition during peak and off-peak times.

It can be clearly observed that the vast majority of vehicles (> 91%) in Pearse Street fall into the category of light vehicles and motorcycles. Cyclists (5.5%) are considered the second highest category of vehicles in Pearse Street during all peak and off-peak times. Buses (2.0%) are the third largest vehicle group and the remaining medium and large vehicles (1.2%) making up the smallest fraction of the total traffic on Pearse Street.

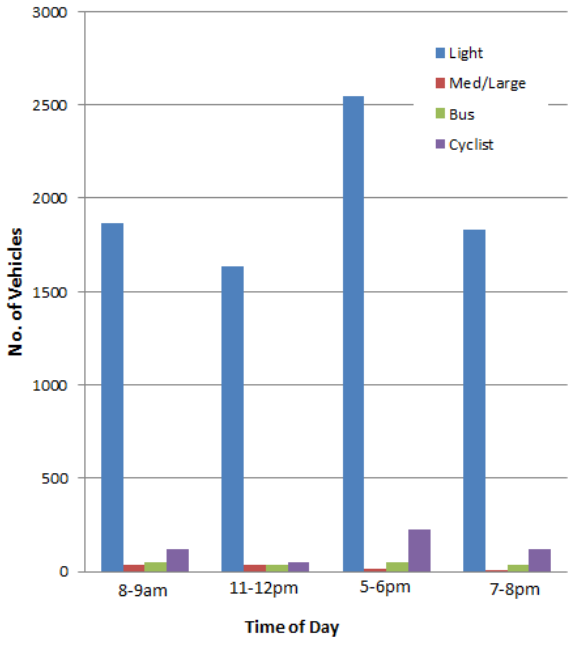

Figure 32: Variations in the fleet composition during peak and off-peak times.

As each vehicle category is responsible for different emission rates, the number of vehicles in each category was multiplied by a coefficient for the respective vehicle type. A number of sources were reviewed for NO_x EFs as differences in these EFs were observed between the literature sources. The emission factors for this study were taken as 0.3 g NO_x km^{-1} for light vehicles and 8.0 g NO_x km^{-1} for buses (NAEI, 2009). As the fraction of medium and large vehicles accounted for only 1.2% of the fleet composition, a similar emissions factor of 8.0 g NO_x km^{-1} was used for this vehicle category. A plot of the total NO_x emissions for each vehicle category is shown in Fig. 33 (a).

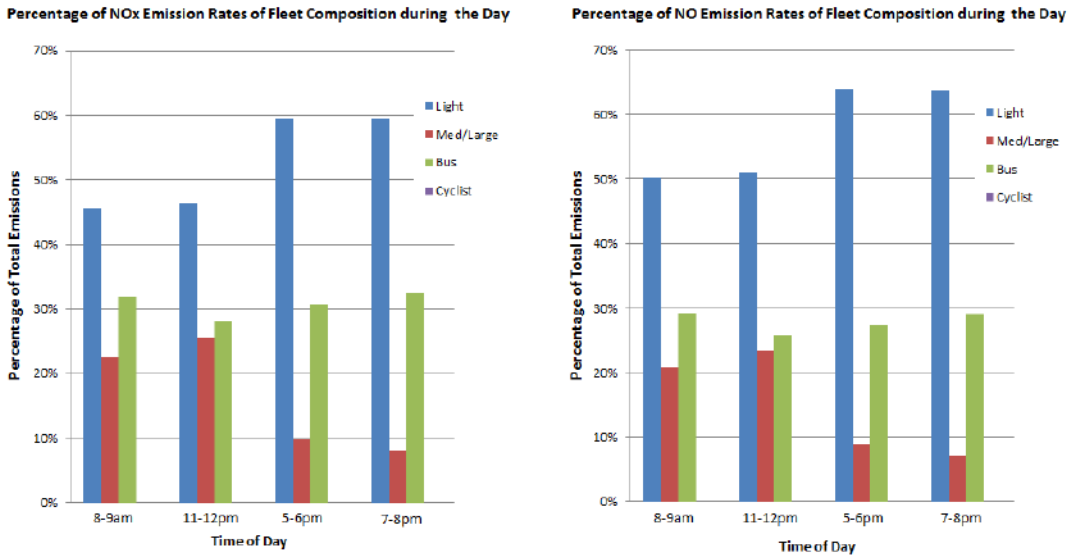

Figure 33: Plots of (a) NO and (b) NO emissions associated with fleet composition.

As this analysis focuses on modelling the dispersion of NO, additional literature was reviewed to determine the ratio of NO to total NO_x. Studies identified the concentration of NO_2 and NO_x and therefore NO was calculated as the difference between NO_x and NO_2 (Carslaw, 2005; Carslaw & Beevers, 2005; Department for Environment Food and Rural Affairs, 2007). To summarise the findings by Carslaw (2005), NO_x concentrations have reduced in the past number of years, yet the NO_2 concentrations have remained constant. Therefore the NO_2:NO_x ratio has recently seen an increase (Carslaw, 2005). This means that a small adjustment was required to the total NO_x emission factors for estimating NO. The percentage of NO_2 to NO_x for light vehicles is approximately 4% and a more significant 20% on average for buses and medium/large vehicles (Kelly et al., 2011). Therefore, an ER of 0.3 g NO km^{-1} for light vehicles and 6.4 g NO km^{-1} for buses or medium/large vehicles was projected after calculating the NO fraction of total NO_x. Fig. 33 (b) illustrates these NO emissions.

The plots of the percentage emissions in Pearse Street which is created by the different vehicle categories in Fig. 33 is very different compared to the previous plot of the fleet composition in Fig. 32. This highlights the importance of the accurate assessment of the fleet composition as the assumption of an average emission factor for each vehicle would generate a significant error in the calibration process. As cyclists have no associated ER, this category is not depicted in Fig. 33. The fraction of light vehicles equated to an average of 53% and 57% of the total NO_x and NO traffic emissions, respectively. However, a distinct difference of approximately 13% was

observed between the average emissions for both NO_x and NO during the morning (46% and 59%) and evening (50% and 63%) periods. This was due to increases of traffic volumes in Pearse Street in the evening period, of which it is primarily light class vehicles. In a similar manner to Fig. 32, a clear difference in NO_x and NO emissions sourced from medium and large vehicles was observed between the morning (24% and 22%) and evening (9% and 8%) periods due to the majority of the vehicles delivering goods in the morning. A similar pattern was visible from the emissions sourced from buses with only a small difference of approximately 2% observed for NO_x (28 – 32%) and NO (26 – 30%) during the day.

Based on the analysis of the traffic data, the calculation of NO emissions from vehicles has a significant amount of variability based on the vehicle type, size, average speed and fuel type. Zhang et al. (2011) stated that measured concentration in a street canyon can be dependent on driving behaviour, vehicle dispersion and traffic flow and that these factors can lead to almost double the pollutant concentration in relatively similar dispersion conditions. The calibration of this model requires significant analysis to ensure the input parameters meet real time conditions.

The estimated ER for the vehicle categories in g NO km^{-1} allows for the calculation of a set ratio between a car and bus or medium/large vehicle emissions. This ratio is useful to reverse calculate the ER of the vehicle emissions in the Pearse Street model from the monitored NO concentration in µg m^{-3}.

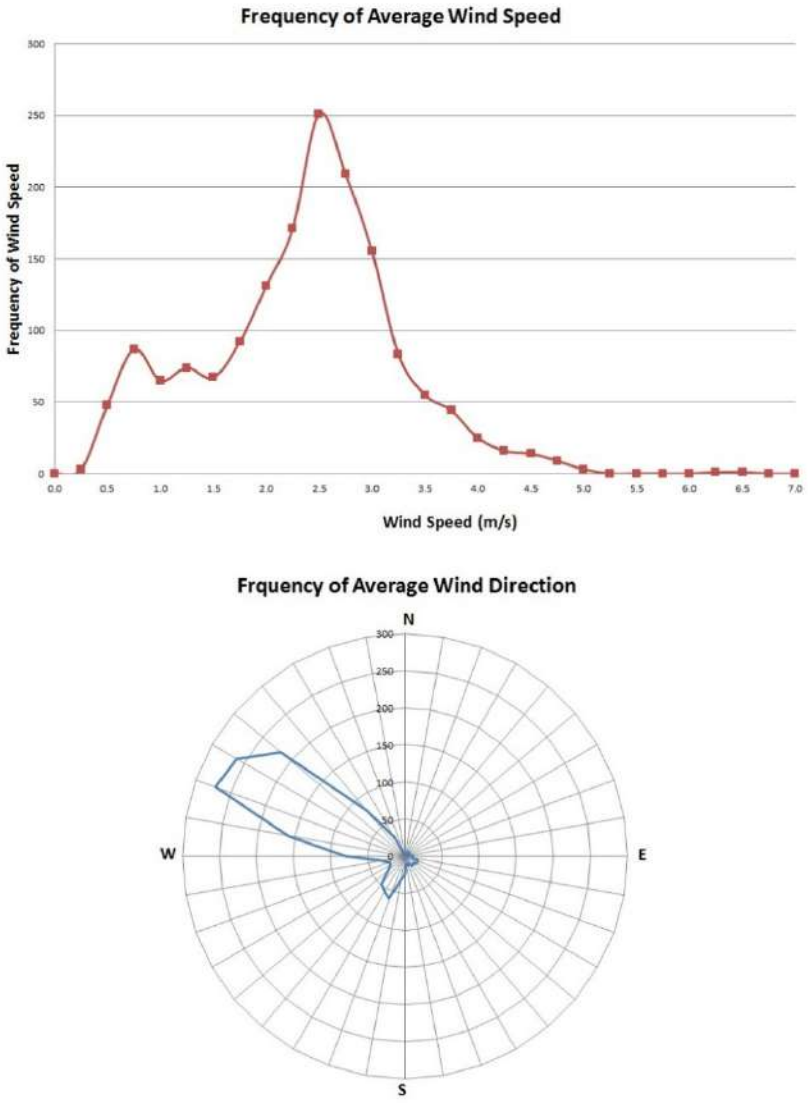

Figure 34: Frequency plot of average wind speed and direction in Pearse Street.

An initial analysis of the data from the wind anemometer on Pearse Street was carried out to identify patterns or trends with respect to wind direction and speed. A plot of the Pearse Street wind parameters observed in Fig. 34 for the monitoring period in December reveals that there is a common range for local wind speed and direction. The predominant wind parameters measured in Pearse Street shown a range in wind speed of 2 to 3 m s^{-1} and wind direction range of between 290° and 310°.

Based on a detailed understanding and validation of the data sets collected for NO_x concentrations, traffic information and wind parameters, the data could then be considered for the calibration process of the Pearse Street model.

2.3.3 Numerical setup and simulations

Canyon geometry

Mesh discretization

A detailed mesh discretization analysis was carried out in FLUENT to determine suitable mesh parameters for the Pearse Street model in accordance with modelling guidelines by COST (2005). The street canyon model was designated with a series of grid mesh schemes (shown in Table 15) combining different surface meshes at canyon floor and/or building surfaces with a proportionate volume mesh. To put the mesh dimensions in context of the size of the canyon model, the street floor was an average of 22 m wide, 380 m long with an average building height of approximately 10 m. This excludes a significant extended height above the buildings and the width over the rooftops.

Mesh	Mesh Scheme Dimensions[1]			Cells[2]	Comparison[3]	
	Floor	Buildings	Volume		150lt	300lt
Fine	0.4	-	1.6	1.33	1.25	1.24
Medium	0.5	-	1.5	0.97	1.60	1.53
Coarse	0.5	-	2.0	0.74	1.87	1.95

[1] All mesh dimensions in metres
[2] Cell count in millions
[3] 1e-04 of pollutant concentrations measured on footpath

Table 16: Details of refined mesh grid schemes and NO dispersion results.

Optimization of mesh scheme

Three meshing schemes were constructed (in line with methodology guidelines) and reviewed to determine the most suitable mesh to optimize accuracy and running time, the results of which are shown in Table 15 and Fig. 35. The table shows details of the three mesh schemes, the number of cells in each model (which is inversely proportional to the model running time) and the average concentration measured on the footpath at times of 150 and 300 seconds. Fig. 35 illustrates the plots of the pollutant concentrations for each of the mesh schemes.

Based on these results the coarse grid mesh was selected for the canyon model. Differences were observed in the results between the mesh schemes from Table 15, however the turbulent behaviour displayed in Fig. 35 existed in all model and suggests that the difference in pollutant concentration was not significant. The mesh schemes meet guideline requirements as the footpath areas were of specific interest and therefore the chosen mesh layout is deemed adequate for this study. The model was meshed with triangular mesh elements of 0.5 m on both footpaths and the road surface with the overall volume meshed with a 2.0 m tetrahedral mesh.

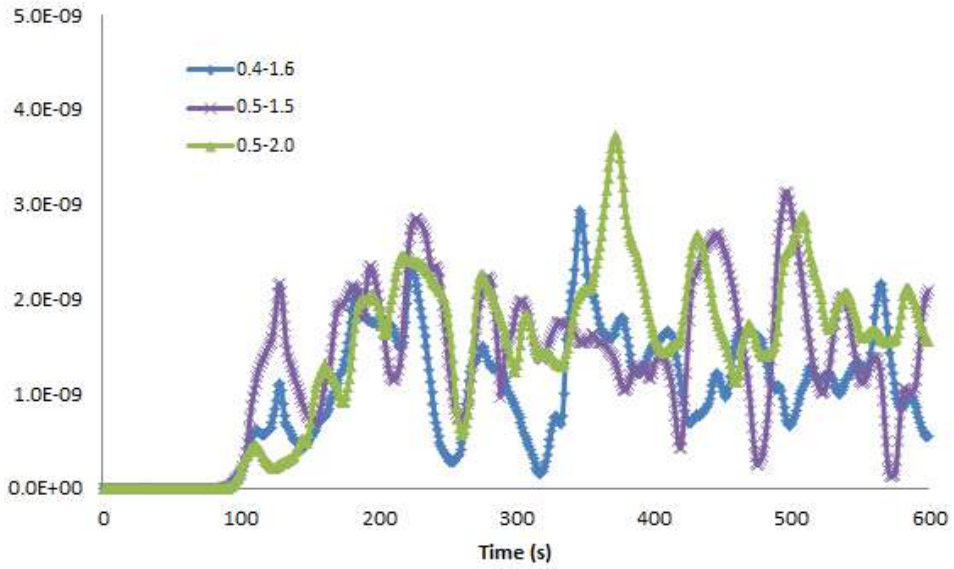

Figure 35: Pollution concentration (kmol m-) at monitoring location for different mesh schemes.

Optimisation of steady state simulation

Prior to the release of the pollutant concentration, the model was initially run for 60 seconds to allow the development of the vortices in the canyon in a similar manner to Baker et al. (2004). This allowed a steady state for air flow to be achieved in the Pearse Street model. The NO concentrations were then released from the individual traffic lanes at ground level (i.e. Z = 0) in the Pearse Street model. The pollutants were emitted as a species mass fraction with different ER for each traffic lane based on the associated traffic composition of the respective lanes. The same ER was used in the reference and passive control models. This allowed for a clear comparison of the effectiveness of the passive control layouts in a real street canyon in different traffic and meteorological conditions.

Optimisation of atmospheric extension above canyon

Presence of a complex building geometry in the Pearse Street along with elements such as a railway bridge increases the complexity of the model and turbulence at roof level. Hence, the model was extended above the rooftop of the buildings by a height of 4 Hr (Hr equals to the height of the tallest building in the canyon) to allow for air flow entering or exiting the canyon above the buildings.

Wind speed and direction

A number of model scenarios were run for different wind speeds and directions. The objective of this phase of the calibration process for the Pearse Street model was to identify the correlation between the input wind parameters and the output at the wind anemometer location in the model.

Model calibration for wind direction

The calibration of wind direction and speed was carried out separately, to a degree, and this was to distinguish between the elements that can influence these parameters individually as well as in unison in an urban canyon environment. Prior to modelling emissions transport and dispersion, a series of models were run for different wind directions (primarily in 45° segments) at the average

wind speed measured from the wind anemometer of 2.5 m s^{-1}. The results of this investigation are plotted in Fig. 36.

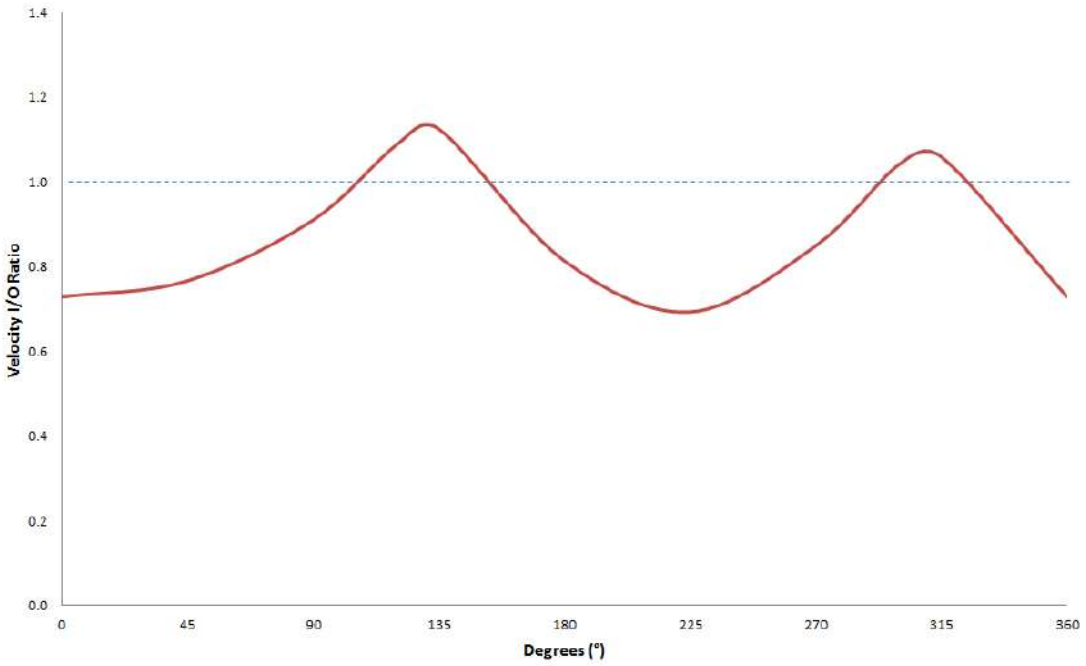

Figure 36: Plot of velocity inlet vs. measured velocity for 360°.

Fig. 36 illustrates the relationship between the inlet velocity (I) and the measured output velocity (O) at the wind anemometer location in each model. An I/O ratio equal to unity indicates an inlet velocity equalling the measured outlet velocity. The plot displays the varying relationship between input and output with respect to the different wind directions. This allows for a back calculation of the input parameters to correspond to a required measured output value, and thus an accurate calibration of the wind direction in the Pearse Street model. The deviations in the I/O ratio were due to the surrounding geometry of the buildings in the canyon, which influenced the wind direction in some cases.

A comparison of the input wind direction to the output wind direction was assessed. An average variability of ±7.5° was found at a wind 1.0 m s^{-1}, with average differences of ±4.1° and ±3.9° for higher wind speeds of 2.5 m s^{-1} and 5.0 m s^{-1}, respectively. The findings suggest an increase in the confidence level of wind direction with an increase in wind speed.

The values of the individual X and Y components of the input velocity and the measured wind anemometer velocity were also compared. This found that differences existed between the percentage differences for the individual X and Y components of the wind velocity. Therefore, the wind direction calibration process requires a case by case assessment to ensure the wind direction in the model is accurate.

A series of canyon simulations were run to establish a confidence level in the calibration process of wind conditions. The results identified a high level of accuracy in wind direction based on input values for wind component values, with a maximum error of ±5° deemed acceptable for the calibration process.

Model calibration for wind speed

In addition to the calibration of wind direction, two additional sets of models were run for different wind speeds to correspond to the lower (1.0 m s^{-1}) and higher (5.0 m s^{-1}) range of measured wind speeds in Pearse Street. The models were run for different wind directions in a similar manner to the previous section. The plot layout for each of the wind speeds resembles the previous figure, but shows a mix of similar and contrasting results for different wind directions (Fig. 37).

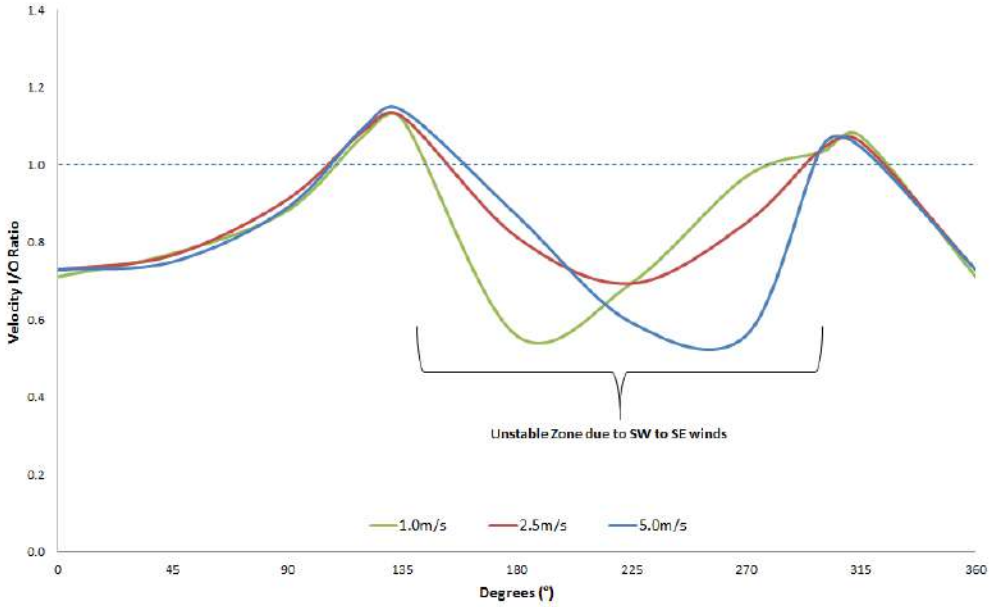

Figure 37: Velocity inlet vs. measured velocity at different wind speeds.

There is a notable variance in the I/O ratio for different wind speeds between 135° and 300°. This is considered to be due to the building extension to the south of the wind anemometer, causing a level of recirculation and turbulence of air. The zone highlighted in Fig. 38 is located to the South of the wind anemometer and therefore wind is clearly influenced by the building behind the anemometer and thus affects the I/O relationship identified in Fig. 37. As the I/O ratio is less than 1.0, the input velocities will be higher than the measured output velocities to calibrate the model. This is due to losses in wind velocity caused by the asymmetry and shapes of the buildings. Therefore, an increased inlet velocity was included for calibrating the Pearse Street model for most scenarios. This analysis allows for the accurate input of I, to ensure O is correlated to the wind velocity required in the Pearse Street model. After analysing the individual X and Y components of the measured wind velocity against the input velocity, the results suggest a very turbulent zone specifically between 135° and 315°. Table 16 identified differences of up to 41% (for both 180° and 270°) were calculated for the X and Y components in this turbulent zone. This enforces the need for a case by case calibration of any street canyon model.

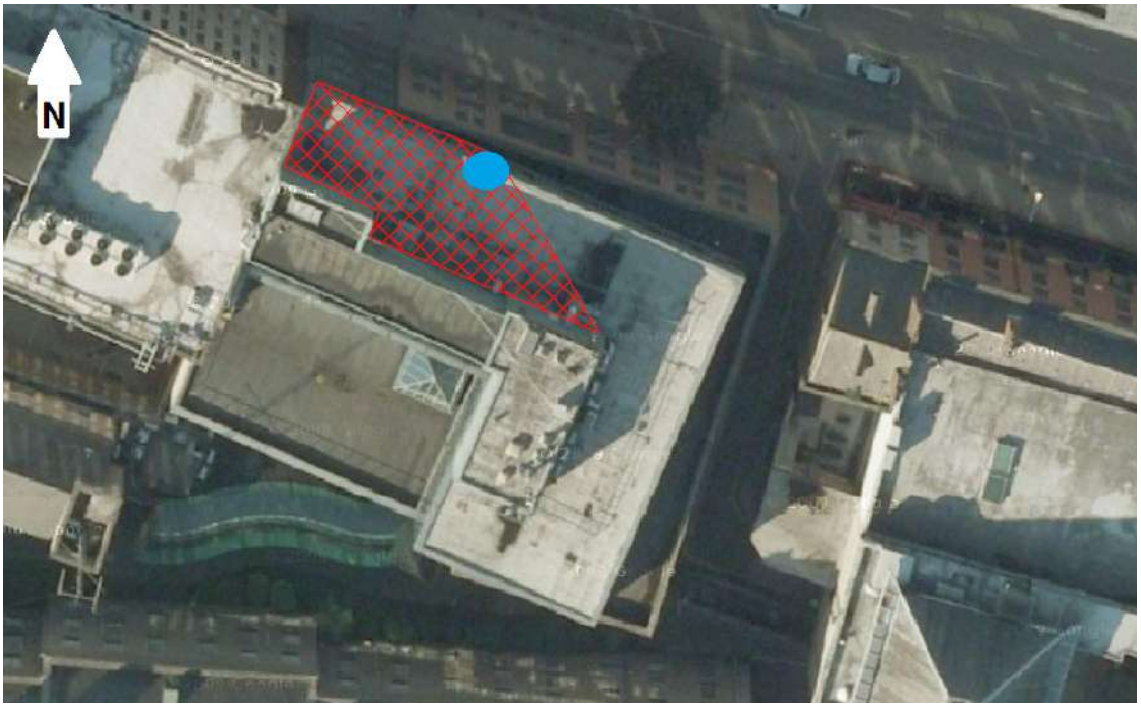

Figure 38: Turbulence zone between 135° and 315°.

Wind Direction	Model Input (m s^{-1})			Model Output (m s^{-1})			% Differences		
	1.0	2.5	5.0	1.0	2.5	5.0	1.0	2.5	5.0
45°	1.0	2.5	5.0	0.77	1.92	3.75	77%	77%	75%
90°	1.0	2.5	5.0	0.88	2.28	4.45	88%	91%	89%
135°	1.0	2.5	5.0	1.12	2.81	5.71	112%	113%	114%
180°	1.0	2.5	5.0	0.54	2.03	4.35	54%	81%	87%
225°	1.0	2.5	5.0	0.69	1.73	2.95	69%	69%	59%
270°	1.0	2.5	5.0	0.97	2.12	2.79	97%	85%	56%
315°	1.0	2.5	5.0	1.07	2.65	5.23	107%	106%	105%
360°	1.0	2.5	5.0	0.71	1.82	3.65	71%	73%	73%

Table 17: Input & output wind speed components for different wind directions.

From this assessment, the correlation of I/O in the coefficient plot (Fig. 37) identified differences between the input values of wind speed and direction and the measured values by the wind anemometer. This allowed an accurate estimation of the input velocity component values to ensure an accurate calibration of the model for real time conditions. The turbulent zone from Fig. 38 is also highlighted in data in Table 16 from the Pearse Street model, whereby wind speed and direction is influenced in one particular zone (180° to 270°). Once the model was calibrated for these conditions, the NO emissions were simulated to calibrate the pollutant concentration to the monitoring point (displayed previously in Fig. 28) in Pearse Street.

A series of simulations were run taking into account the findings from Table 16, using the data for the percentage difference for wind speed to input the adjusted value to ensure the output

value was similar to the measured wind speeds from the monitoring period. Fig. 39 displays a plot of confidence (R^2 of 0.96) for output wind speed from some of the models versus measurements of wind speed by wind anemometer in parallel wind conditions. Similar confidence levels were estimated for both the X and Y components with calculated coefficients of determination (R^2) of 0.96 and 0.94, respectively.

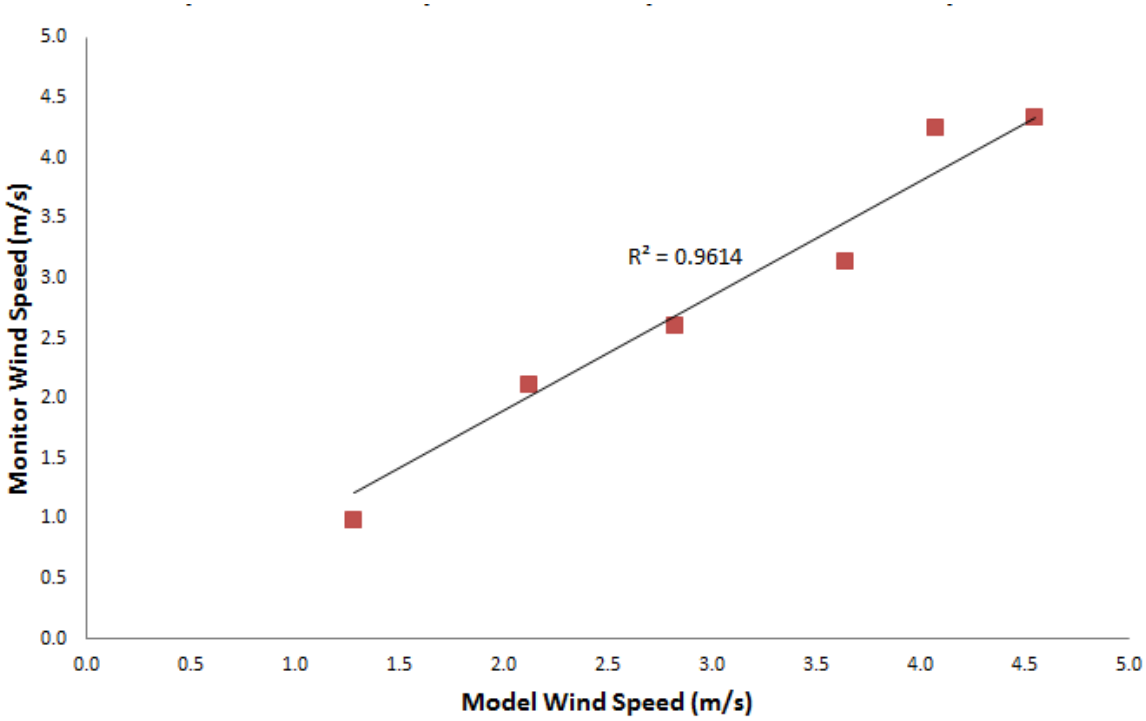

Figure 39: Confidence in model output vs. real-time wind speed measurements.

NO emission

A breakdown of the different traffic fleet compositions was required for the NO calibration process to estimate the emissions entered into the Pearse Street model. Due to the regular variances in wind direction, the calibration of the model focused on wind data corresponding to the parallel wind direction to the direction of the street. As the data varied significantly for each 15-min duration, a ±10° variance to the given wind direction was considered acceptable as it behaved in a similar manner as defined by Hoydysh and Dabberdt (1988). To ensure the most accurate NO data set was selected, the 5-min wind direction averages were also reviewed and compared to the 15-min values. The NO concentrations were only included if the variation in the 5-min averages were within a ±20° deviation from each selected wind direction. This reduced the size of each data set, but it ensured that the NO concentrations for a given wind direction were accurate and could be correlated to the other parameters influencing pollutant dispersion in the street canyon.

For the perpendicular wind direction, a different approach was required as no perpendicular wind data met the set criteria. For perpendicular wind, a selection of 5-min average values was chosen to calibrate the Pearse Street model. Traffic data was then adjusted for the 5-min averages for

each of the lanes and the average measured pollutant concentration over the 15-min period for which the 5-min wind direction fell within was used.

NO emissions vs. lane distribution

As Fig. 30 showed no direct correlation between the traffic data and measured pollutant concentrations, the distribution of traffic across the four lanes was considered. The data sets shown in Table 17 and Table 18 contain a mix of peak and off-peak traffic times, high and low wind speeds and different traffic compositions for the perpendicular and parallel wind directions, respectively.

			Wind		Traffic				
No.	**Date**	**Time**	**Direction (°)**	**Speed (m s^{-1})**	**L1**	**L2**	**L3**	**L4**	**Total**
1	4th December	8:15 am	200.72	1.83	9	38	48	5	100
2	19th December	8:30 am	204.72	1.50	43	160	173	86	462
3	6th December	11:35 am	204.91	1.86	13	50	66	3	132
4	11th December	11:55 am	199.45	0.54	42	108	159	12	321
5	13th December	5:55 pm	200.77	1.97	22	87	76	55	240
6	14th December	7:15 pm	186.07	0.41	97	244	256	61	658
7	14th December	7:20 pm	205.94	0.54	90	205	254	60	609

Table 18: NO concentrations and traffic data for perpendicular wind conditions at 5 minutes intervals.

Where manual traffic data was not available, the automated SCATS traffic counts were used. As significant errors were evident for Lane 1, estimations were made for the lane based on trends. These were based on the trends identified during the analysis of the manual traffic data for peak and off-peak traffic and the relationship between the manual and automated traffic counts for the other three lanes.

No.	Date	Time	Wind		Traffic				
			Direction (°)	Speed (m s^{-1})	L1	L2	L3	L4	Total
1	7th December	8:15 am	280.13	2.43	30	192	160	52	434
2	5th December	8:15 am	295.28	2.98	38	149	179	75	442
3	5th December	8:45 am	290.40	3.04	45	160	222	98	524
4	5th December	11:15 am	291.25	2.59	54	182	147	0	383
5	9th December	11:15 am	286.77	2.64	39	190	204	17	450
6	13th December	11:15 am	289.63	2.83	38	179	202	20	437
7	7th December	11:30 am	288.91	4.60	50	189	169	10	418
8	15th December	11:45 am	292.75	3.22	38	186	193	30	447
9	7th December	11:45 am	284.05	4.52	44	202	158	7	411
10	5th December	12:00 pm	284.01	3.19	53	177	152	6	388
11	5th December	5:15 pm	285.62	2.71	56	229	223	138	646
12	6th December	5:45 pm	282.94	1.92	49	216	246	129	640
13	8th December	5:45 pm	283.58	4.22	43	142	141	172	497
14	15th December	7:15 pm	296.19	0.88	46	216	217	59	537
15	6th December	7:30 pm	291.88	2.09	67	194	182	13	456
16	15th December	7:45 pm	287.50	0.78	46	223	228	42	539
17	8th December	8:00 pm	284.56	3.63	43	226	210	24	504

Table 19: NO Concentrations and traffic data for parallel wind conditions at 15 minutes intervals.

Traffic distribution, fleet composition and vehicular dispersion are simplified in the FLUENT models and therefore a semi-empirical equation was developed from literature to take into account these factors in addition to the results from the model (Gallagher et al., 2013b). Equation 25 shows the derived equation which accounts for factors which are not included in the CFD model. The equation derives that the monitored NO concentration is a function of vehicle speed, fleet composition, lane distribution, emission rates and vehicular turbulence.

$$NO_M = \left(\sum_{L=1}^{4} \frac{E_C}{S_A}.V_C.D_L + 22\sum_{L=1}^{4} \frac{E_O}{S_A}.V_O.D_L\right).T_C \quad (25)$$

where

NO_M: NO measured by monitor in Pearse Street (10^{-9} g m^{-3})

E_C: ER rate for cars (based on average vehicle speed in different traffic conditions) (10^{-3} g m^{-1})

E_O: ER rate for other vehicles (10^{-3} g m^{-1})

S_A: Surface area of each traffic lane (m^2)

V_C: Number of cars in the respective lane

V_O: Number of other large vehicles (Buses & HGVs) in the lane

D_L: Coefficient for distribution of emissions between individual lane and monitor

T_C: Coefficient of vehicular turbulence in the canyon

The ERs for cars (E_C) and other vehicles (E_O) were found to be equal to 0.3 and 6.4 g NO m^{-1}, respectively (Fig. 33). As NO monitoring data (NO_M in g m^{-3}) was collected as volumetric data, the

calculated ERs (E_C and E_O in g m^{-1}) were divided by a factor representing the road surface area (S_A in m^2) for each lane as defined in equation 26. This was to balance the units within the equation.

$$E_R = \frac{E_C}{S_A} \; or \; \frac{E_O}{S_A} \tag{26}$$

Fleet distribution

The equation was initially developed based on the diffusion equation defined by Johnson et al. (1973), which calculated the pollutant concentration at the receptor location as a function of distance from the pollutant source. The NO concentration transported from the emissions source to receptor for different vehicle types, namely cars (V_c) and other (V_o), was based on the traffic counts and fleet composition from each individual lane.

$$NO_M = \sum_{L=1}^{4} V_C \cdot \frac{E_C}{S_A} + \sum_{L=1}^{4} V_O \cdot \frac{E_O}{S_A} \tag{27}$$

This equation takes fleet composition into consideration, and the introduction of the E_c:E_o ER ratio for cars to large vehicles which was calculated as 1:22 was then introduced into equation 27. This updated version of the equation is shown in equation 28.

$$NO_M = \sum_{L=1}^{4} V_C \cdot \frac{E_C}{S_A} + 22 \sum_{L=1}^{4} V_O \cdot \frac{E_C}{S_A} \tag{28}$$

Traffic lane emissions

The previous section dealt with simplifying the effect of wind direction in the calibration process, however, a number of elements are still not included in this equation and needed to be addressed, namely the effect of wind speeds and vehicular dispersion. The simulation of traffic emissions from each individual lane determined the distribution of emissions (D_L) from the source to receptor which varied in parallel and perpendicular wind conditions and was dependent on wind speed. To ensure optimum accuracy in the calibration process, the equations shown in Fig. 40 and Fig. 41 (based on 1.0 g m^{-3} emitted from lane) were used to calculate the dispersion coefficient for each respective lane of interest based on the respective wind speed and direction.

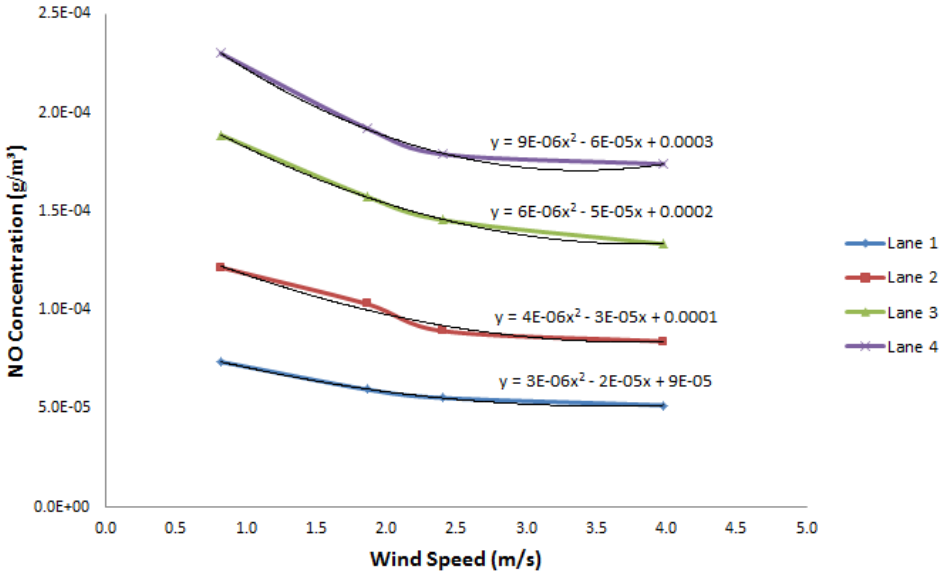

Figure 40: Estimation of vehicle emissions transported from traffic lane to monitor in parallel (286°) wind conditions.

In parallel wind conditions, the increase in wind speed had only a small influence on the fraction of emissions transported from each lane to the monitoring location. The curvilinear profile of NO concentrations against wind speed, displayed in Fig. 40, suggests that an increase in wind speed clearly reduces the concentration measured at the monitoring location. In addition, the most notable differences in NO concentrations occurred with an increase in wind speed at the lower end of the wind speed profile.

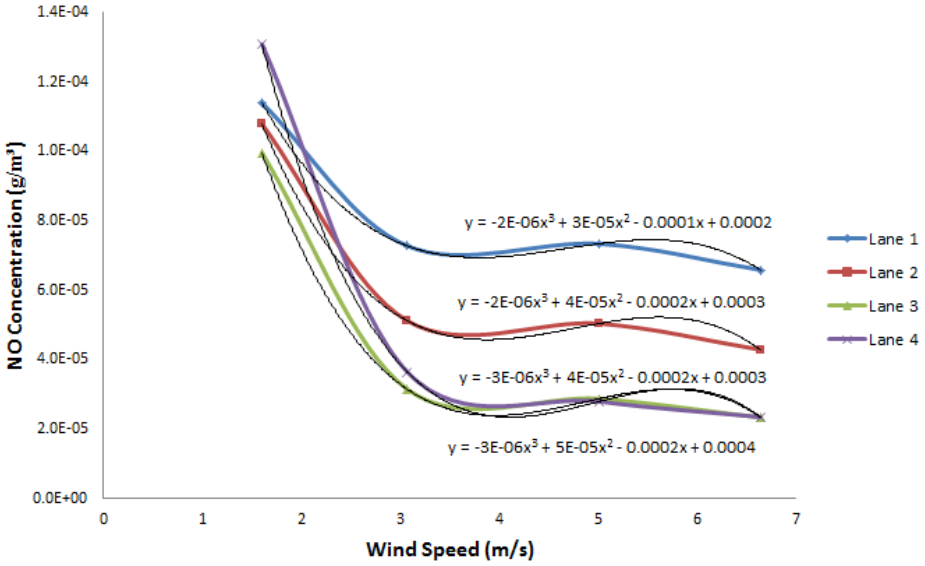

Figure 41: Estimation of vehicle emissions transported from traffic lane to monitor in perpendicular (196°) wind conditions.

In perpendicular wind conditions, the results of the simulations suggest that the emissions were transported by the primary eddy away from the monitoring location and then recirculated in the eddy towards the monitor in higher wind conditions. In low wind conditions, the highest concentration measured at the monitoring point were sourced from Lane 4, which was the lane nearest the monitor. This was due to the weakness of the eddy in low wind speeds, thus the emissions were transported directly from the traffic lane to the monitor. The results suggest that the bus lane (which is location the largest distance away from the monitor) constitutes the greatest fraction of NO at the monitoring location in higher wind speeds, assuming vehicular turbulence is not included in the simulations. Fig. 40 and Fig. 41 allow for the introduction of emissions distribution into equation 29 for the respective lanes to accurately calculate the ER or measured NO concentration. The concentrations were calculated with respect to the measured wind speed. A simplified version of the equation is shown in equation 30.

$$NO_M = \sum_{L=1}^{4} V_C . D_L . \frac{E_C}{S_A} + 22 \sum_{L=1}^{4} V_O . D_L . \frac{E_C}{S_A} \quad (29)$$

$$NO_M = \frac{E_C}{S_A} . \left(\sum_{L=1}^{4} V_C . D_L + 22 \sum_{L=1}^{4} V_O . D_L \right) \quad (30)$$

As the emissions rate (E_C) and surface area (S_A) are the same in both vehicle categories due to the inclusion of the correction factor of 22, these factors can be taken out of the overall equation.

The equation term for estimating the emission transport from the source to receptor ($[x^2+z^2]^{1/2}$ based on Pythagoras' theorem to calculate hypotenuse length) by Johnson et al. (1973) was omitted here and replaced by the term representing the distance between the source and receptor for each lane with the D_L coefficient.

Vehicular turbulence

The introduction of vehicular turbulence (T_C) was the most challenging element of the model calibration process. A turbulence coefficient was required in the equation to compensate for the omission of vehicular turbulence in the model simulations due to the simplification of the surface emissions source, commonly used to significantly reduce the computational running time of each model (Baker et al., 2004; Murena et al., 2009; Gallagher et al., 2011, 2012). As the turbulence and emission rates are affected by the speed and nature of flow of traffic, some statistical analysis was required to determine a series of different turbulence coefficients for different traffic flows (Jicha et al., 2000; Solazzo et al., 2008, 2009). The turbulence coefficient included factors such the rate of turbulence, average vehicle speed and wind speed. The vehicular turbulence formula is displayed in equation 31.

$$T_C = S_F \left({}^{V_S}/_{W_S} \right)^2 \quad (31)$$

where

S_F: Vehicle shape factor based on vehicle counts and fleet composition in street
V_S: Average vehicle speed (m s^{-1}) based on Table 19
W_S: Average wind speed at corresponding time of day (m s^{-1})

A statistical analysis of the data sets in Table 17 and Table 18 was carried out to estimate a set of turbulence coefficients related to vehicular turbulence. This took into account the measured wind speed (W_S) and estimated average traffic speeds (V_S) at different times of the day and which were considered to be proportional to the traffic count in the street canyon. Table 19 lists the estimated average vehicle speeds in each lane for each of the traffic count periods. The traffic speed and traffic volume are both linked to the rate of congestion in the canyon, therefore each parameter was interconnected in the analysis process so that a change of one value alters the result of the entire equation.

Time	Average Speed (m s^{-1})					
	Lane 1	Lane 2	Lane 3	Lane 4		Average
8:00 – 9:00 am	5.56	4.17	4.17	6.94		5.2
11:00 – 12:00 pm	6.94	4.17	5.56	6.94		5.9
5:00 – 6:00 pm	5.56	2.78	2.78	6.94		4.5
7:00 – 8:00 pm	6.94	4.17	5.56	6.94		5.9
Note: Average Speed limits adjusted to correspond to different traffic counts						

Table 20: Average vehicle speed in each lane in different traffic conditions.

The level of congestion in the street is directly linked to the average vehicle speed as the increase in vehicle numbers leads to increased congestion at peak traffic times, which can reduce the effect of vehicular turbulence and increase emission rates from vehicles. The calibration of pollutant concentration is highly influenced by all these factors and the subsequent paragraphs deal with the calibration of the model to take vehicular turbulence into account in the equation.

Turbulence shape factor

As the NO emission for different vehicle types are different, a vehicle shape factor (S_F) related to turbulence traffic rate was calculated and used instead of the actual traffic count. This rate was calculated using equation 32.

$$S_F = \frac{(V_{tc}+V_{to})}{(V_{tc}+ t_o.V_{to})} \quad (32)$$

where

V_{tc}: Total number of cars in street
V_{to}: Total number of other large vehicles in street
t_o: Turbulence coefficient for larger vehicle (in this case 5)

The fraction of large vehicles varies during the day and therefore influences pollutant dispersion in the model. The distribution of the average percentage of large vehicles in each lane is plotted in Fig. 42. It displays the differences in fleet composition in the four traffic lanes at different times of the day.

Two scenarios were compared using the final calibration equation, to determine the effect of the turbulence shape factor in the final equation. As manual traffic data was required to include this factor, it was considered important to understand the scale of influence of the shape factor. The findings determined that the exclusion of the shape factor did not significantly influence the results and therefore the automated traffic data could be used as it provided a larger data set for calibration purposes.

The relationship between the average vehicle speed (V_s) and average wind speed (W_s) in equation 31 accounts for the effect of vehicle speed upon wind speed as values constantly change for both parameters. Equation 33 displays the simplified version of equation 25.

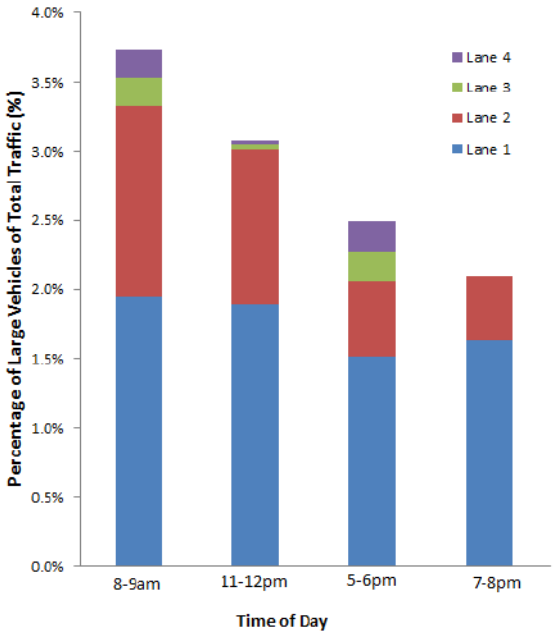

Figure 42: Percentage of large vehicles of total traffic at peak and off-peak traffic times.

$$NO_M = \frac{E_C}{S_A}.(\sum_{L=1}^{4} V_C.D_L + 22\sum_{L=1}^{4} V_O.D_L).T_C \quad (33)$$

Emissions adjustment coefficient

The fit between the monitoring data and the output from equation 33 required a further coefficient to further improve the accuracy of the equation. The ratio between the NO monitoring data and the calculated NO concentration was plotted against wind speed for the parallel and perpendicular data sets. These plots are displayed in Fig. 43 and Fig. 44.

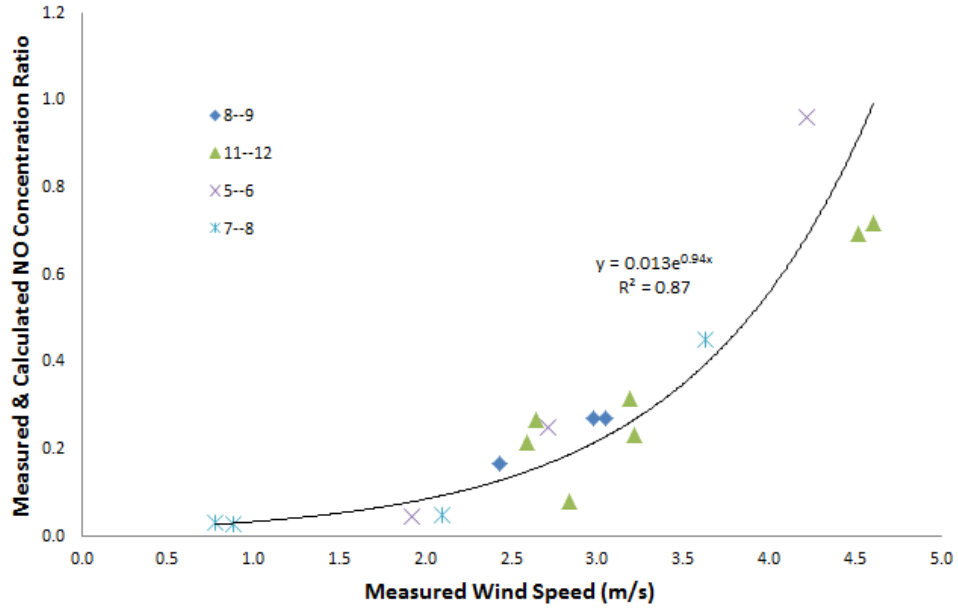

Figure 43: Correlation of measured wind speed and ratio of measured and calculated NO concentrations in parallel wind conditions.

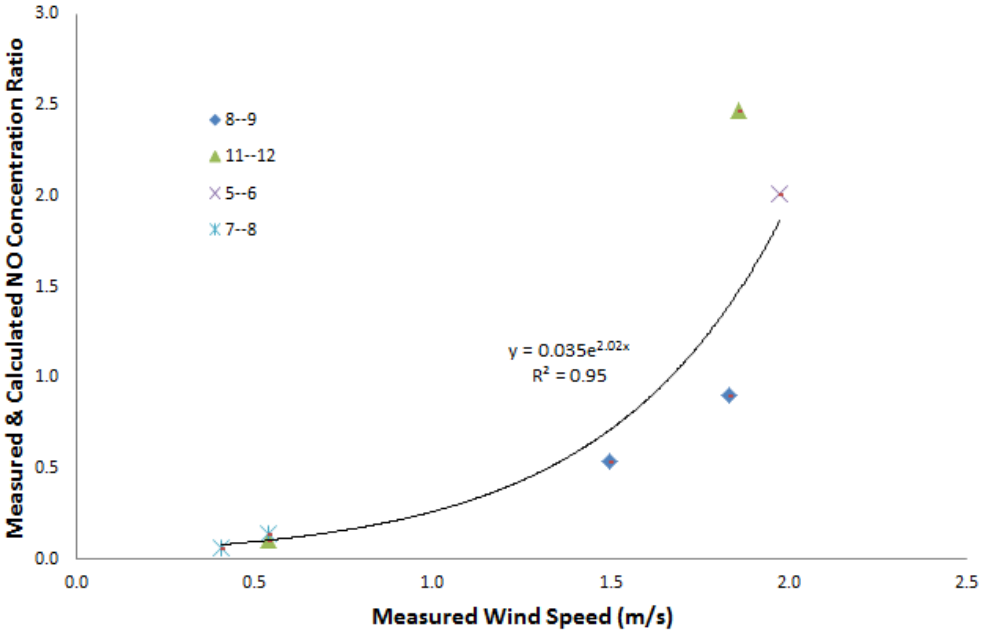

Figure 44: Correlation of measured wind speed and ratio of measured and calculated NO concentrations in perpendicular wind conditions.

The data in both figures represent the most stable wind conditions and therefore a high level of confidence (R^2 of 0.87 and 0.95) can be taken for the fit equations to be used to accurately estimate the pollutant concentration at the monitoring location. Therefore, the equations for the trendlines (C_R) are included in equation 34 to provide an accurate equation to estimate pollutant concentrations at the monitoring location. In addition, a I/O coefficient is included so that the calculated concentration equals the measured concentration for each data point.

$$NO_M = \frac{E_C}{S_A}.(\sum_{L=1}^{4} V_C.D_L + 22\sum_{L=1}^{4} V_O.D_L).T_C.C_R.C_{IO} \quad (34)$$

where

C_R: Adjustment coefficient based on measured to calculated concentration ratio against wind speed
C_{IO}: I/O coefficient to ensure calculated concentration (y) equals measured concentration (x)
The I/O coefficients vary for different wind directions and values of 1.37 and 1.13 were calculated for parallel and perpendicular wind directions, respectively.

NO measurement vs. model output

Measurements of NO were compared to the calibrated model for each wind direction and the findings are shown in Fig. 45.

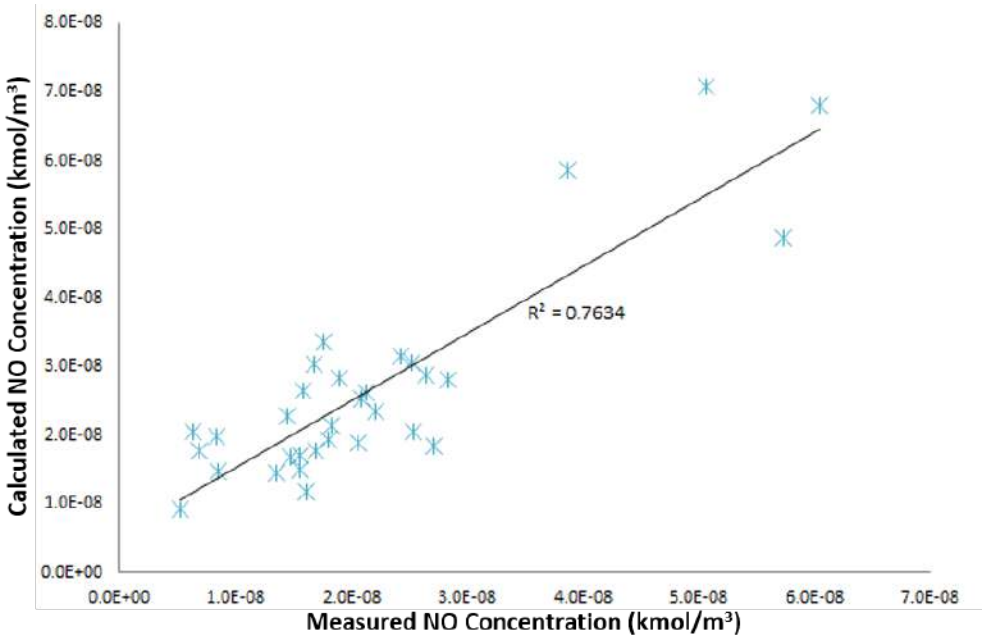

Figure 45: Correlation of measured NO concentrations vs. model output.

An R^2 of 0.76 demonstrated a good fit for the calibrated model to the measured NO concentrations in Pearse Street. Based on the findings of the calibrated Pearse Street models for

three different wind directions, the assessment of introducing passive controls in the models was subsequently carried out.

2.3.4 Investigated PCS scenarios

The analysis assessed the LBW passive control in parallel (~286°) and perpendicular (~196°) wind direction to traffic flow in the canyon. The predominant wind speed of 2.5 m s^{-1} which was measured at the monitoring location was also used in the modelling process to investigate passive control model. Fig. 46 displays the locations of the monitoring point in the Pearse Street plan view of the street canyon. The LBW considered in the study exhibit a number of openings at junctions, bus stops and emergency exits.

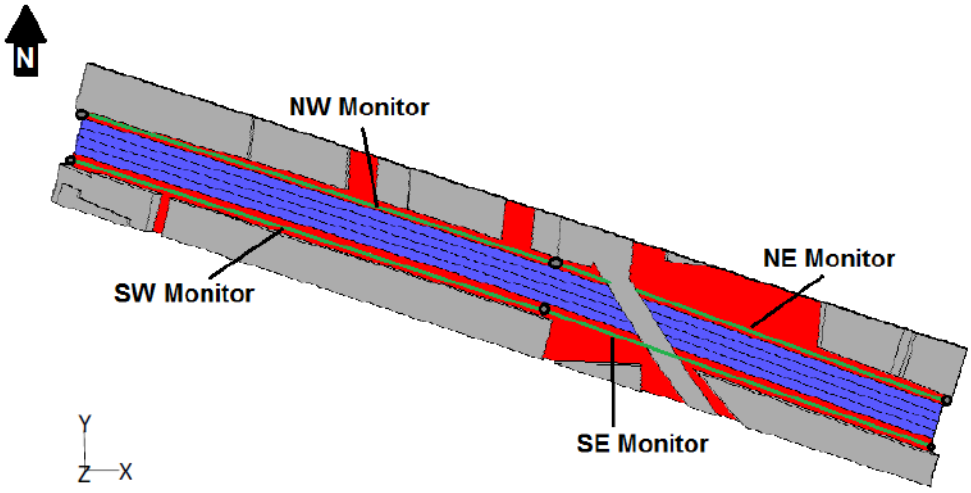

Figure 46: Plan view of Pearse Street model with footpath monitoring locations

3 Results

The aim of this section is to present outcomes of modelled scenarios of with and without PCS in each iSCAPE city. Several simulations of PCS will provide the changes in air quality depending on meteorological conditions as well as characteristics of investigated PCS (height, thickness and density of GI, dimensions of LBW, configurations of trees and LBW in street canyon and open-roads).

3.1 Bologna

In this section, the results regarding Marconi street are shown, to evidence the differences between the winter and summer diurnal cycles. After that, the same approach is also used to present the results for Laura Bassi street. Then, differences between the two street canyons are outlined. Finally, the results of the simulations conducted for two ideal scenarios are shown: a case with Marconi St. with trees and a case with Laura Bassi St. without trees.

3.1.1 Marconi street – summer

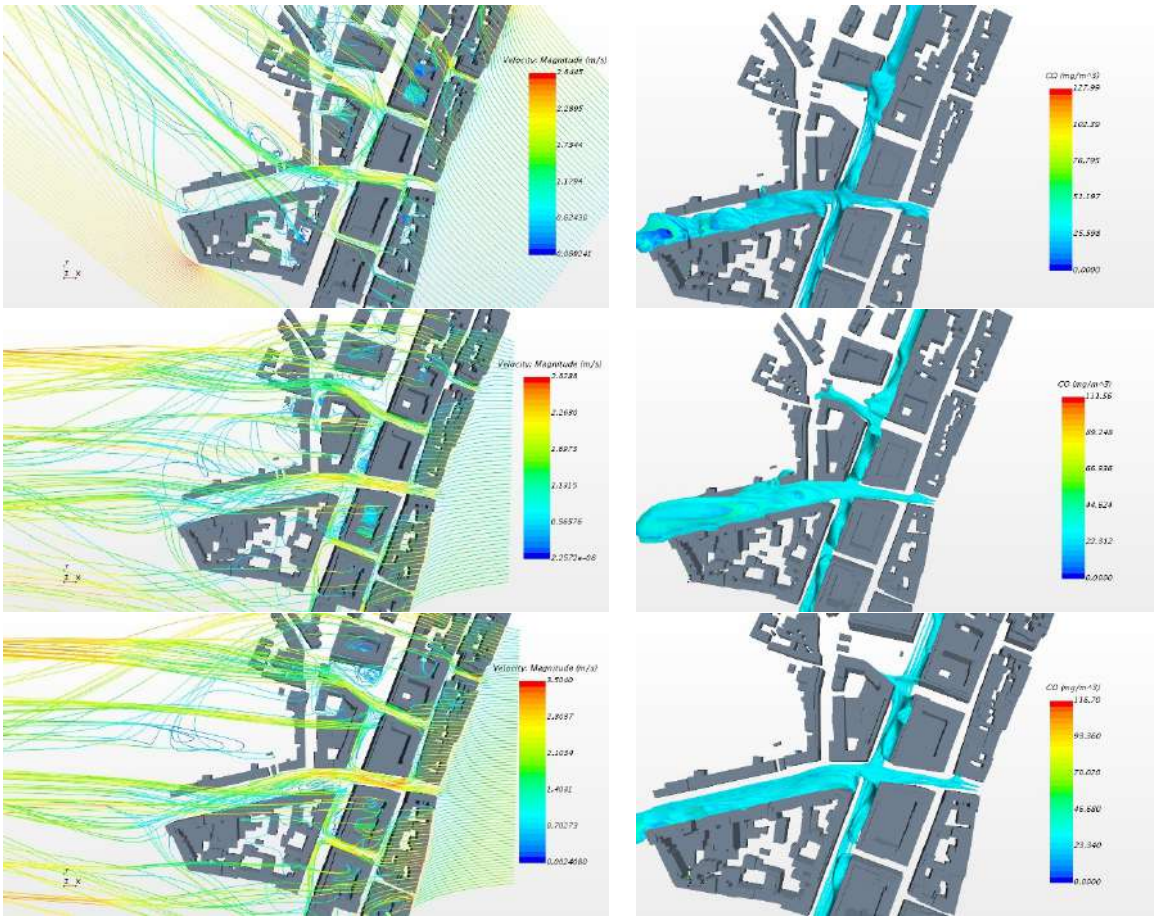

Figure 47: Marconi summer, afternoon. Case 22/08/2017 UTC 10:00 (top), UTC 12:00 (middle) and UTC 14:00 (bottom). Streamlines (left) and CO concentration (right).

Fig. 47 shows the streamlines and CO concentrations obtained for the afternoon hours, from UTC 12:00 to UTC 14:00. In particular, the wind directions for the two cases UTC 12:00 and UTC 14:00 are similar, as shown by Table 1 (93° and 91° respectively), but the wind velocity is higher in the second case. This difference gives similar streamlines along the street parallel to the flow (Riva Reno street) but different streamlines in the street perpendicular to the flow (Marcon street). In the first case (UTC 12:00), vortices are visible at the sides of the intersection, while in the second case, no vortices are present near the intersection. This results in different CO plume shapes, as shown by Fig. 47 (right), with CO peaks that occur for the first case (UTC 12:00) and not in the second one (UTC 14:00).

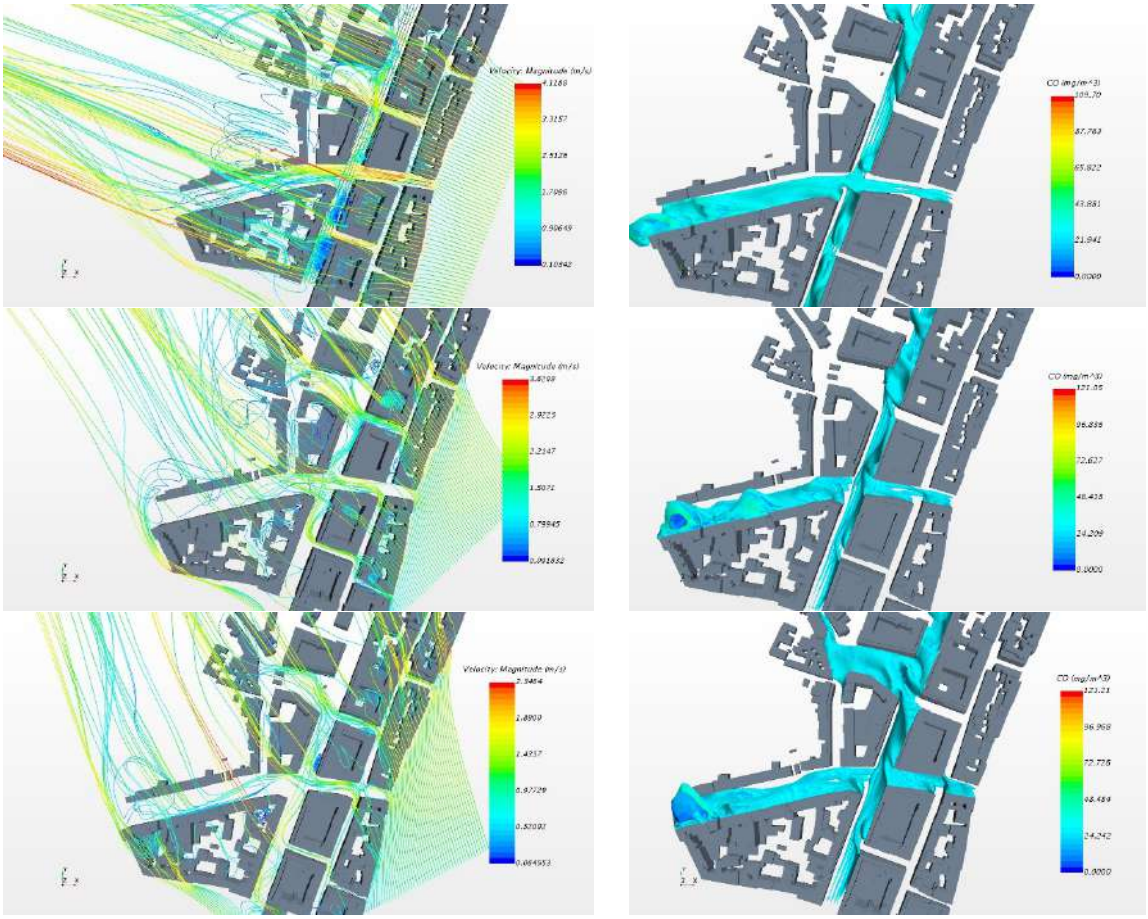

Figure 48: Marconi summer, evening. Case 22/08/2017 UTC 16:00 (top), 18:00 (middle) and 20:00 (bottom). Streamlines (left) and CO concentration (right).

Fig. 48 shows the streamlines and CO concentrations obtained for the evening hours, from UTC 16:00 to UTC 20:00. The wind direction is rotating from East to South (from 107° to 151°) and the wind velocity is reducing (from 6.3 m s^{-1} to 4.2 m s^{-1}), as shown by Table 1. In the first case (UTC 16:00) the wind velocity is high, but the flow is almost parallel to Riva Reno street. Then, the flow separation at the upstream corner of Riva Reno street leads to the formation of recirculating vortices at the entrance of the sides of the intersection, in Marconi street. As a result, the CO plume is located at one side of the intersection, as shown by Fig. 48 (right, top).

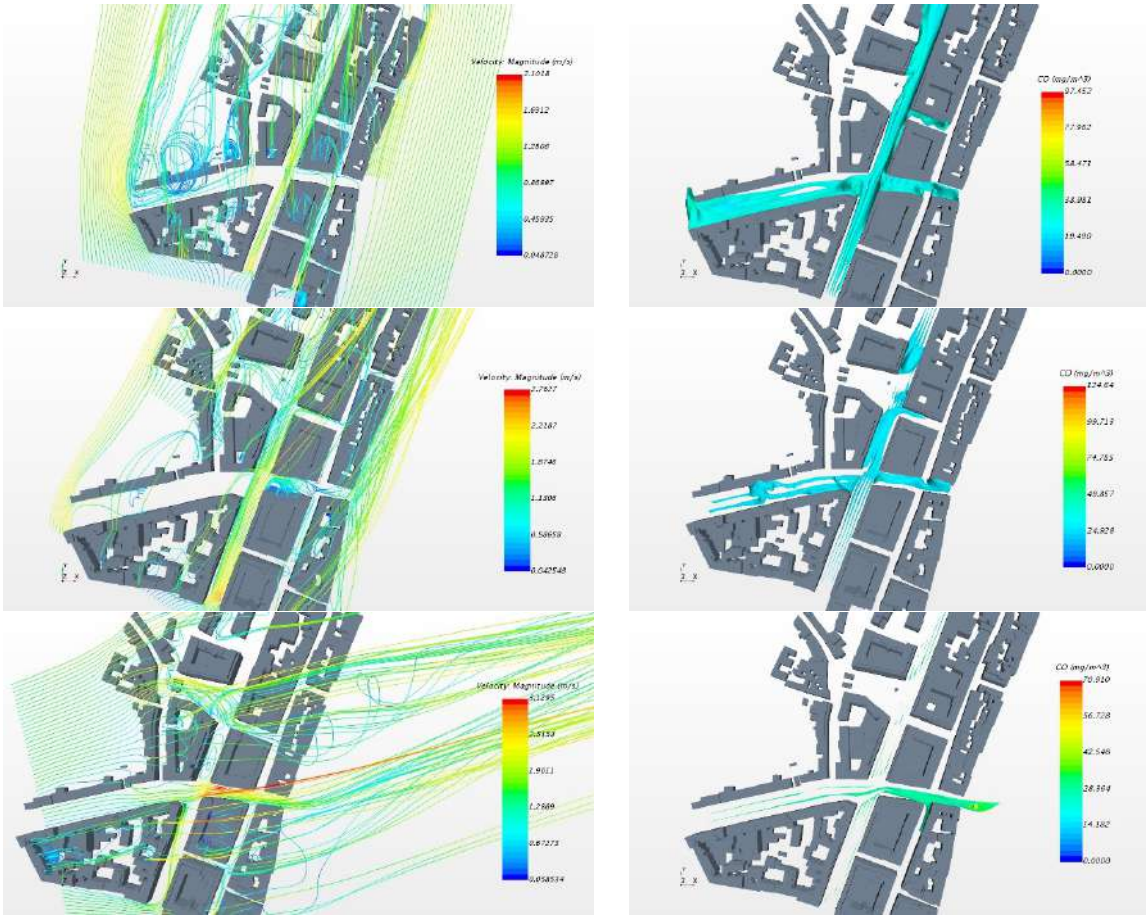

Figure 49: Marconi summer, night. Cases 22/08/2017 UTC 22:00 (top), 23/08/2018 UTC 0:00 (middle) and 2:00 (bottom). Streamlines (left) and CO concentration (right).

Fig. 49 shows the streamlines and CO concentrations obtained for the night hours, from UTC 22:00 (22/08/2017) to UTC 2:00 of the 23/08/2017. The wind direction is rotating from South to West (from 190° to 257°) and the wind velocity is increasing (from 2.9 m s^{-1} to 4.8 m s^{-1}), as shown by Table 1. In the first case (UTC 22:00) the wind velocity is parallel to Marconi street. Then, the flow separation at the upstream corner of Marconi street leads to the formation of recirculating vortices at the entrance of the sides of the intersection. This results in higher CO concentration levels at the two sides of the intersection, as shown by Fig. 49 (right, top).

Fig. 50 shows the streamlines and CO concentrations obtained for the morning hours, from UTC 4:00 to UTC 8:00 of the 23/08/2017. The wind direction is coming from South-West (with angles 239° and 221° respectively) in the first two cases, while in the third case wind is form West (with angle 92°). In the second case (UTC 6) the wind is almost parallel to Marconi street. Then, increase of CO concentration upstream the intersection is obtained. This case corresponds to a rush hour traffic. The recirculation vortices upstream the intersection causes higher CO concentration levels at the East side of the intersection, as shown by Fig. 51.

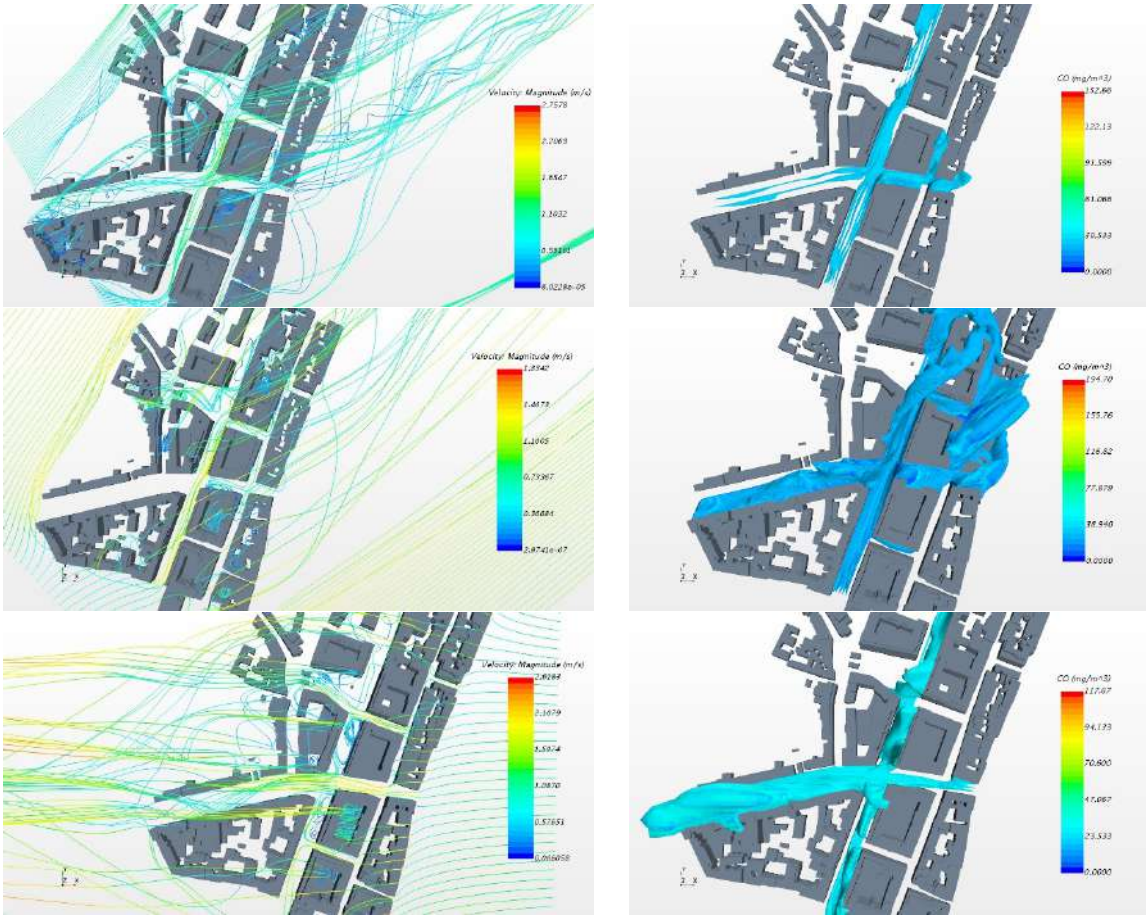

Figure 50: Marconi summer, morning. Cases 23/08/2017 UTC 4:00 (top), 6:00 (middle) and 8:00 (bottom). Streamlines (left) and CO concentration (right).

As a closure of the summer diurnal cycle, Fig. 52 shows the streamlines and CO concentrations obtained at noon (local time), i.e. the case 23/08/2017 UTC 10:00. The wind direction in this case (with an angle of 76º) is closer to that observed in the cases 23/08/2017 UTC 12:00 and UTC 14:00 rather than to that of the same time on the day before (22/08/2017 UTC 10:00). The wind velocity in this case is lower than on the day before. In this case, vortices and CO peaks are visible at the South sides of the intersections, while in the second case, no vortices are present near the intersection, in all the intersections along Marconi street.

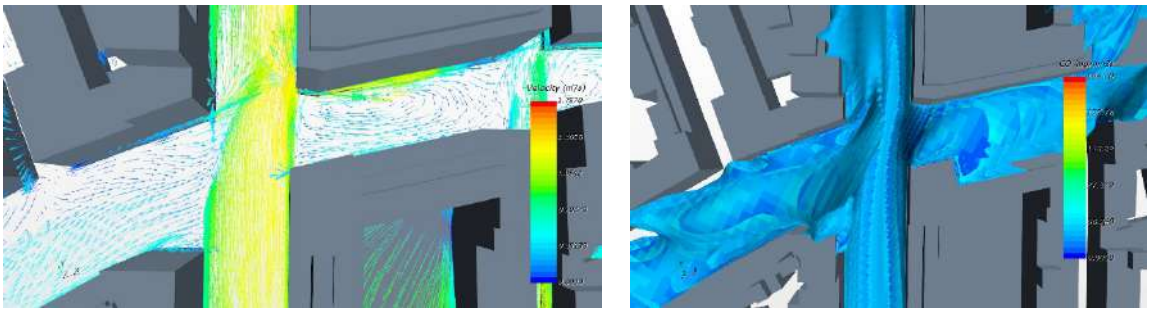

Figure 51: Marconi summer, morning. Case 23/08/2017 UTC 6:00. Streamlines (left) and CO concentration (right).

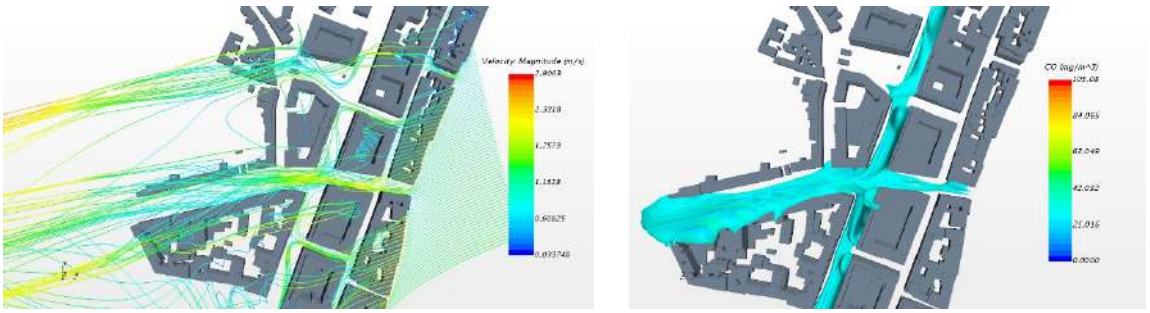

Figure 52: Marconi summer, 23/08/2017 UTC 10:00. Streamlines (left) and CO concentration (right).

3.1.2Marconi Street – winter

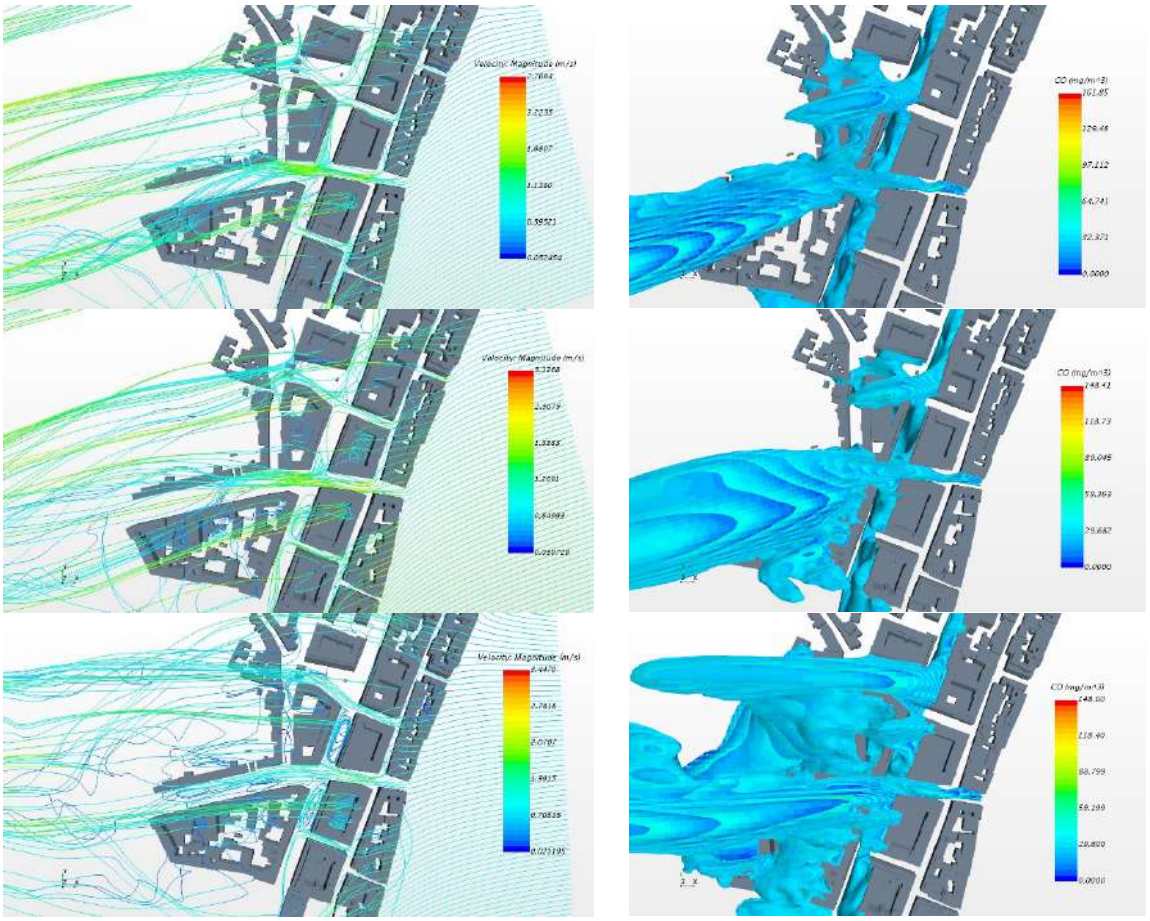

Figure 53: Marconi winter, afternoon. Cases 08/02/2018 UTC 10:00 (top) UTC 12:00 (middle) and UTC 14:00 (bottom). Streamlines (left) and CO concentration (right).

Fig. 53 shows the streamlines and CO concentrations obtained for the afternoon hours, from UTC 10:00 to UTC 14:00 of the 08/02/2018. The wind direction is North-East (with angles in the range 75° – 86°), and the wind velocity is in the range (1.5 m s^{-1} – 2.1 m s^{-1}). The streamlines show

similar behaviour of the flow field: a channelling flow from East to West in via Riva Reno street, with two recirculation vortices at the entrance of the two sides of Marconi street. It is interesting to notice that the two recirculation vortices have the same length of one building block, i.e. the recirculation is broken by the air inlet from tributary side streets. CO concentration peaks are observed in correspondence of these recirculation zones for Marconi street.

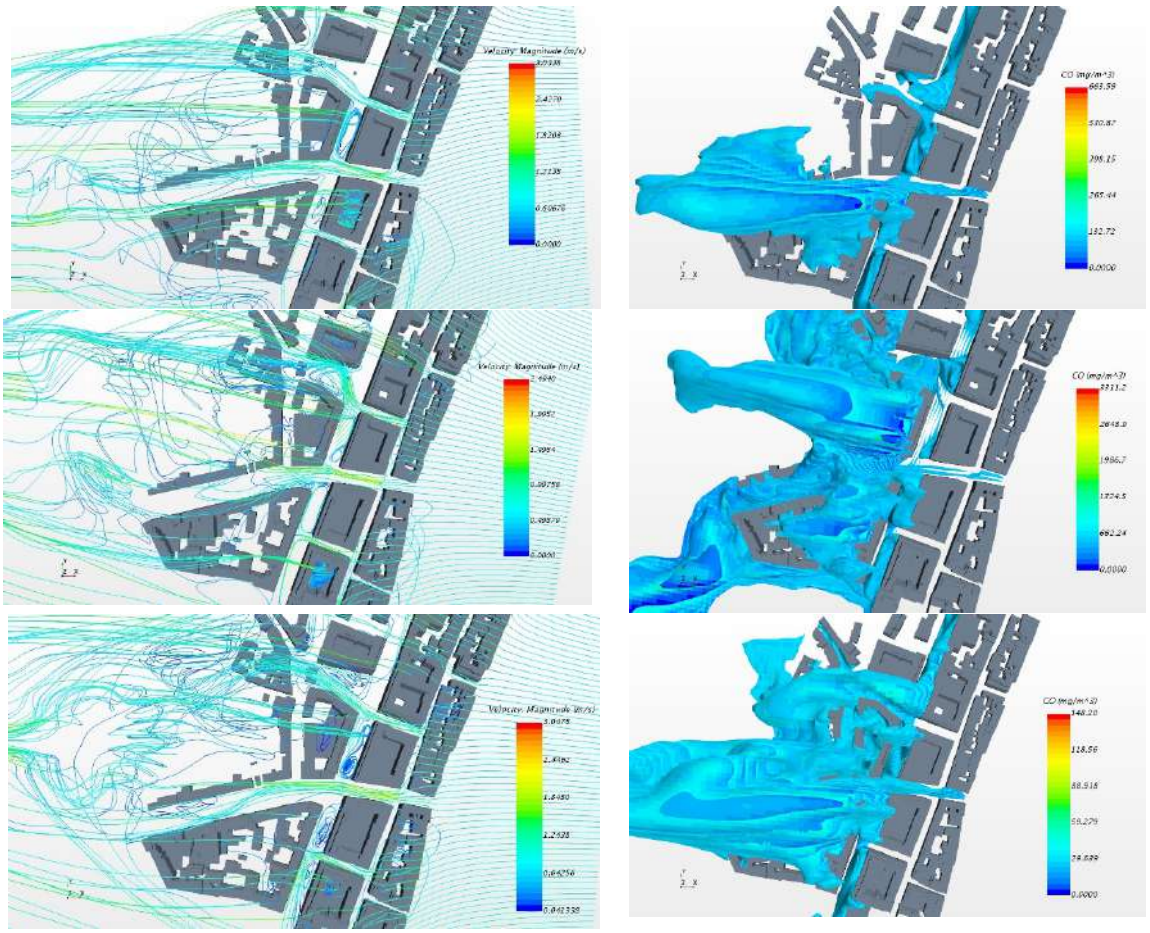

Figure 54: Marconi winter, evening. Cases 08/02/2018 UTC 16:00 (top) UTC 18:00 (middle) and UTC 20:00 (bottom). Streamlines (left) and CO concentration (right).

Fig. 54 shows the streamlines and CO concentrations obtained for the evening hours, from UTC 16:00 to UTC 20:00 of the 08/02/2018. The wind direction is East (with angles in the range 88° – 101°), and the wind velocity is in the range (1.6 m s^{-1} – 3.2 m s^{-1}). The streamlines show similar behaviour of the flow field: a channelling flow from East to West in via Riva Reno street, with two recirculation vortices at the entrance of the two sides of Marconi street. The shape of recirculation vortices depends on the intersection geometry in combination with wind direction and wind velocity. For instance, Fig. 55 shows the velocity vectors obtained for case 2 (08/02/2018, UTC 18:00) and 3 (08/02/2018, UTC 20:00). In case 2, when the wind direction is perpendicular to Riva Reno street, only two vortices appear at the two sides of Marconi street. In case 3, when the wind direction is slightly inclined with Riva Reno street, two counter-rotating vortices appear at the South side of Marconi street.

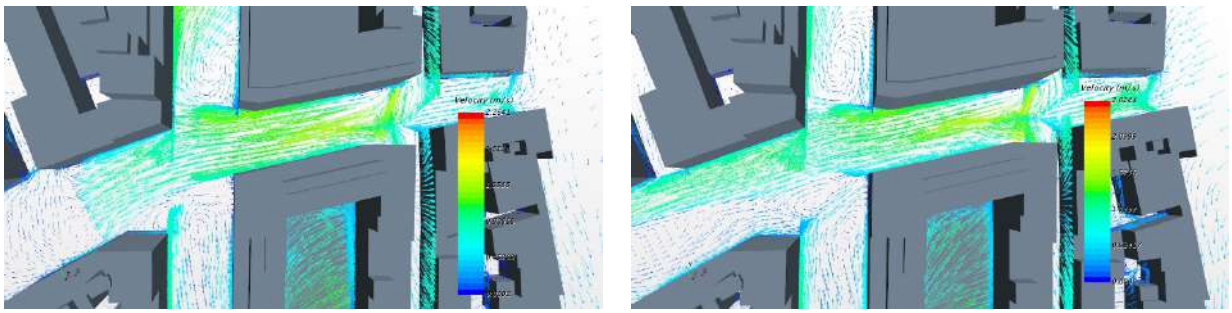

Figure 55: Marconi winter, evening. Velocity vectors obtained for cases 08/02/2018 UTC 18:00 (left) and UTC 20:00 (right).

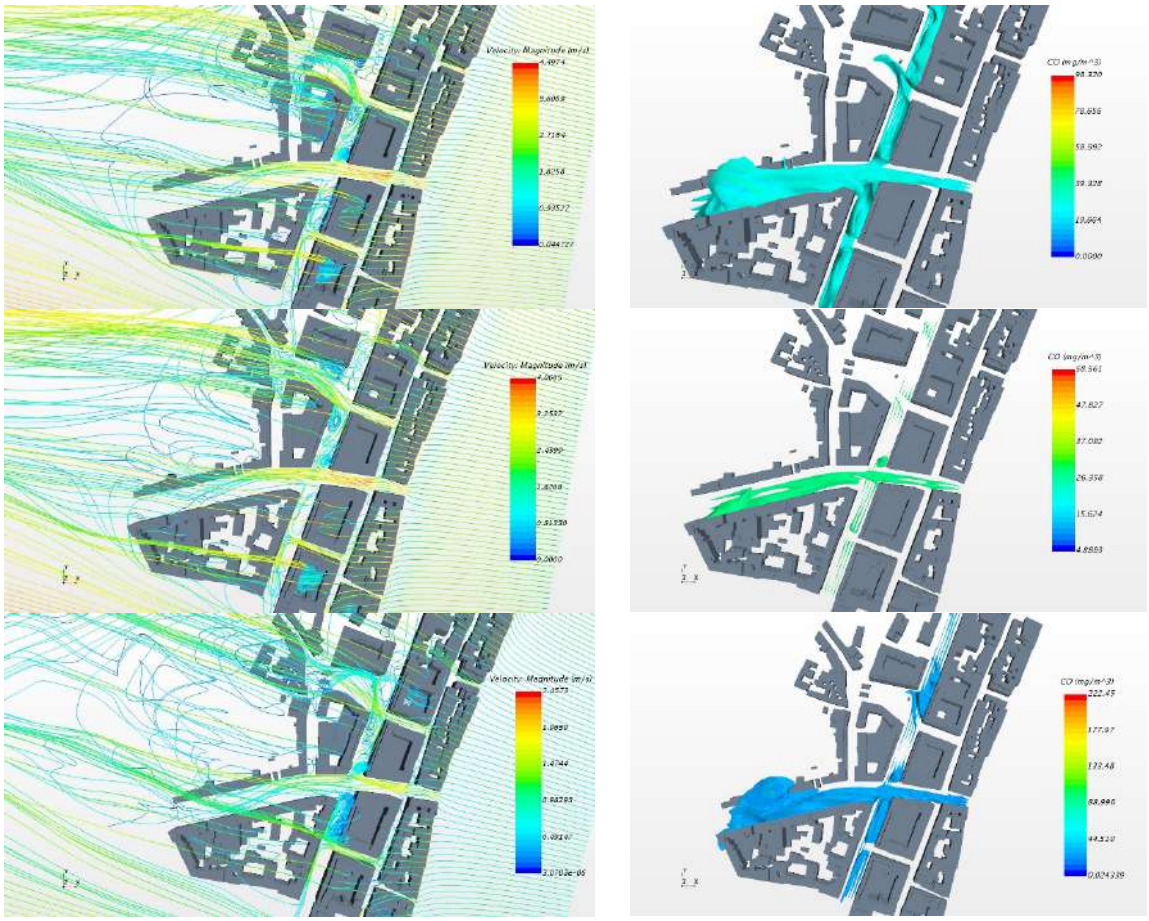

Figure 56: Marconi winter, night. Cases 08/02/2018 UTC 22:00 (top), 09/02/2018 UTC 0:00 (middle) and 09/02/2018 UTC 2:00 (bottom). Streamlines (left) and CO concentration (right).

Fig. 54 shows the streamlines and CO concentrations obtained for the evening hours, from UTC 22:00 of the 08/02/2018 to UTC 2:00 of the 09/02/2018. The wind direction is East (with angles in the range 99º – 103º), and the wind velocity is in the range (2.6 m s^{-1} – 7.3 m s^{-1}). In the first two cases, the combination of a high velocity channelling along Riva Reno street with the presence of a curve in Riva Reno street after the intersection create flow separation in the South side of Riva Reno street, after the intersection.

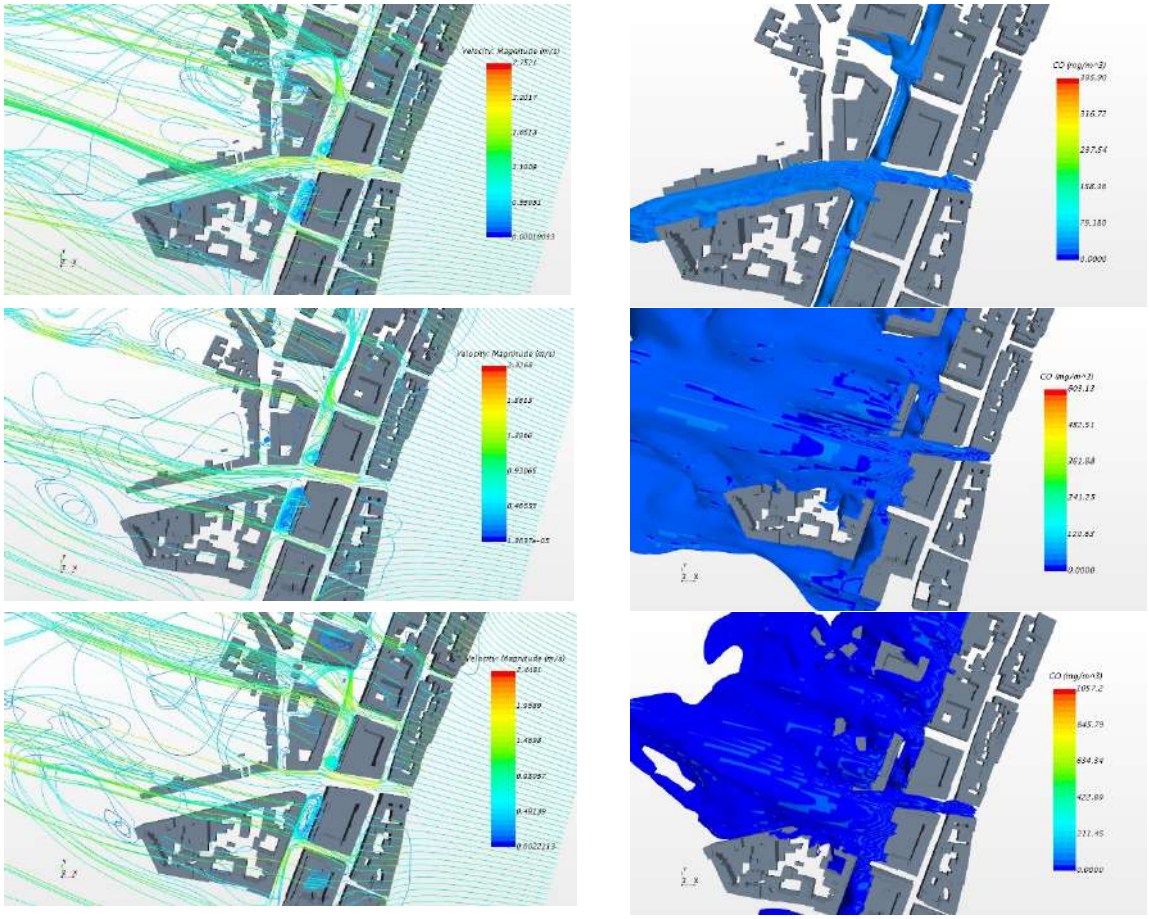

Figure 57: Marconi winter, morning. Cases 09/02/2018 UTC 4:00 (top), UTC 6:00 (middle) and UTC 8:00 (bottom). Streamlines (left) and CO concentration (right).

Fig. 57 shows the streamlines and CO concentrations obtained for the morning hours, from UTC 4:00 to UTC 8:00 of the 09/02/2018. The wind direction is from East (with angles in the range 103° – 107°), and the wind velocity is in the range (1.5 m s^{-1} – 2.3 m s^{-1}). These three cases represent peak traffic events, as during the morning the transit of buses through Marconi street is especially intense. In the first two cases, the combination of a high velocity channelling along Riva Reno street, together with the presence of a curve in Riva Reno street after the intersection creates flow separation in the South side of Riva Reno street, after the intersection. Fig. 58 shows velocity vectors (left) and CO concentration profiles (right) obtained near the intersection for case 2 (09/02/2018 UTC 6:00). The recirculation vortices at the two sides of the intersection correspond to CO concentration peaks. Near those peaks, high pollutant concentration gradients are observed.

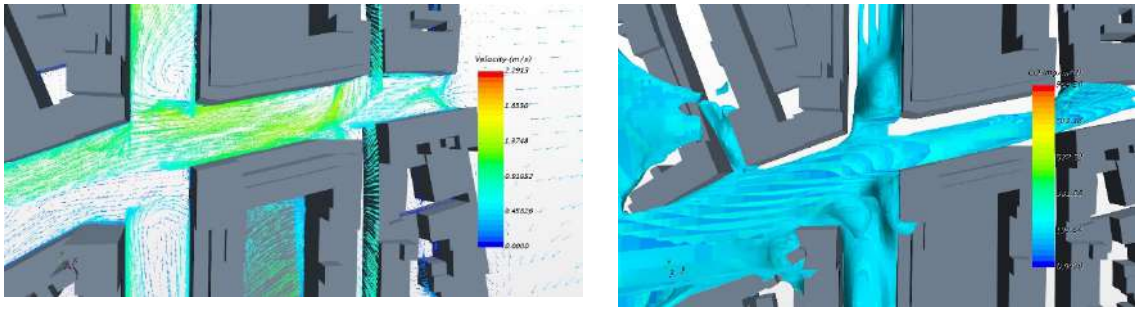

Figure 58: Marconi winter, morning. Case 09/02/2018 UTC 6. Velocity vectors (left) and CO concentration (right).

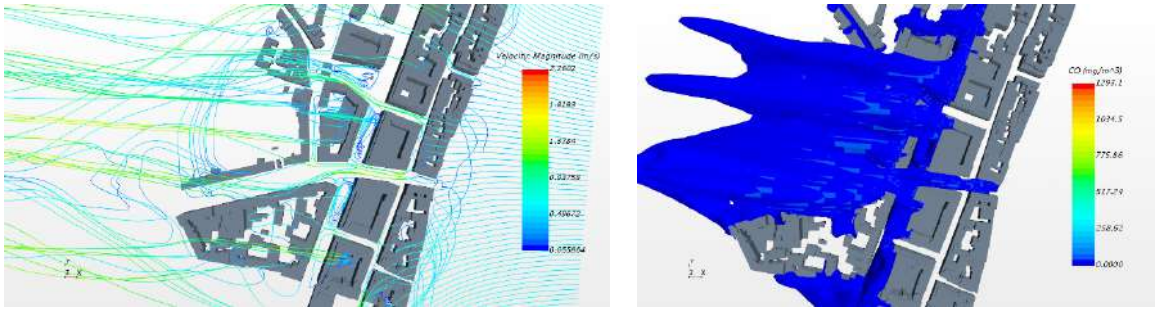

Figure 59: Marconi winter, noon. Case 09/02/2018 UTC 10:00. Streamlines (left) and CO concentration (right).

As a closure of the winter diurnal cycle, Fig. 59 shows the streamlines and CO concentrations obtained at noon (local time), i.e. the case 09/02/2018 UTC 10:00. The wind direction in this case (with an angle of 94°) is from East, with the lowest wind velocity measured during the experimental campaign. The same flow structures as those observed for the other cases are present, but with higher CO concentration values.

3.1.3 Marconi Street – results

In this section Marconi Street canyon modelling investigation has been outlined to determine the effect of geometry on pollutant distribution. In particular, the CO distribution near the traffic intersection (TI) between Marconi Street and Riva Reno Street has been investigated. Quantification of the increases in pollutant concentrations at the sides of the TI have been provided in Table 20. The table displays the results for the area of influence of the TI in terms of the presence and dimensions of the recirculation vortices at the sides of the TI and the percentage difference in pollutant concentrations between TI and pathways along Marconi Street in different wind conditions.

Wind direction	Traffic	Recirculation vortices	Vortex width V_w/W	Vortex length V_l/W	Vortex height V_h/W	CO_V/CO_m
Parallel	Peak	Both sides	1	>5	2	2.3
	Off-peak	East side	0.5	0.5	1.3	1.1
45º	Peak	Both sides	1	>5	1.9	1.8
	Off-peak	Both sides	0.5	0.5	1.2	1.5
Perpendicular	Peak	Both sides	1	>5	1.8	2.6
	Off-peak	North side	0.5	0.5	0.8	1.4

Table 21: Area of influence at the TI.

The table refers to Marconi street, so that parallel means that the wind direction is parallel to Marconi street axis, 45º means that the angle between Marconi street and wind direction is 45º and perpendicular means that the wind direction is perpendicular to Marconi street axis. As the angle between Marconi street axis with the North-South direction is 25º, the first condition means that the angle between wind direction and the North-South direction is about 25º or 205º in the first case, 70º or 250º in the second and 115º or 295º in the third case. Table 20 displays the presence of recirculation vortices at both sides of the TI for all the wind directions during peak traffic conditions. The pollutant concentrations on the TI sides are always higher than those corresponding to pathways. During off-traffic conditions the presence of vortices is not symmetric, as the TI is not exactly symmetric. In the case of off-peak conditions, the vortices have the dimension of a cone, with basis diameter generally equal to 1/2W, where W is the street width, and a height higher than W. During peak traffic conditions, the width of the recirculation zone is about the street width W, while the length is equal to the length of an entire building block, that in this case is greater than 5W. The increases in pollutant concentrations within the recirculation vortices are between 10% to 40% in off-peak conditions, while in traffic peak conditions the CO concentration within the vortices can be more than twice that obtained on the pathways. These results confirm that pollutant concentrations vary significantly at various locations around TIs, in agreement with Goel and Kumar (2014), with maximum values within the recirculation vortices at street corners. The dimensions of these vortices depend on the aspect ratio of the street, in combination to the wind direction.

3.1.4 Laura Bassi street – summer

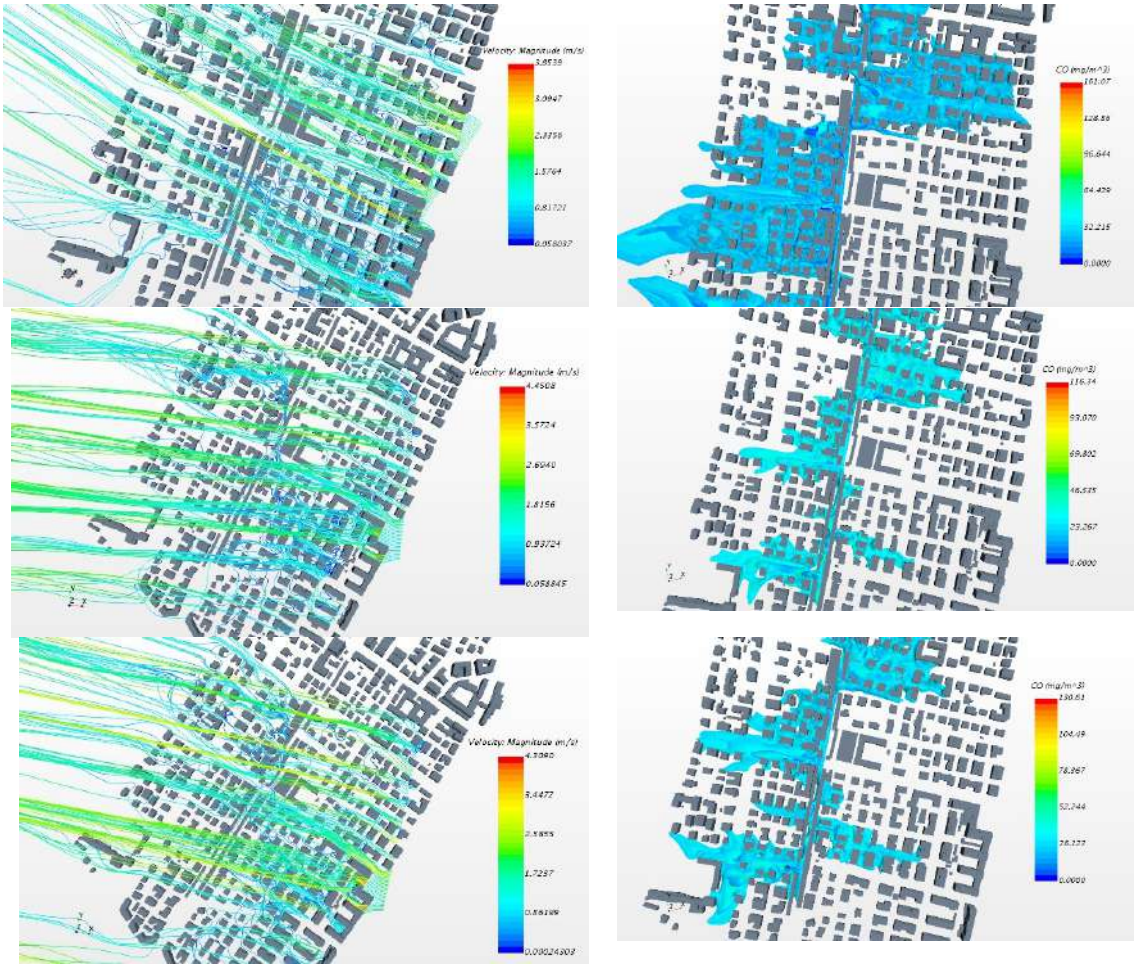

Figure 60: Laura Bassi street, summer afternoon. Case 22/08/2018 UTC 10:00 (top), UTC 12:00 (middle) and UTC 14:00 (bottom). Streamlines (left) and CO concentration (right).

Fig. 60 shows the streamlines and CO concentrations obtained for the afternoon hours, from UTC 10:00 to UTC 14:00. In particular, the wind directions for the two cases UTC 12:00 and UTC 14:00 are similar, as shown by Table 1 (93° and 91° respectively), but the wind velocity is higher in the second case. The figure shows that, for these two cases, air flow channelling through the main street perpendicular to Laura Bassi street (Mezzofanti street) is obtained. However, near the intersection between Laura Bassi street and Mezzofanti street, no recirculation zones as those obtained at the intersection between Marconi street and Riva Reno street are observed. The presence of trees and the different arrangement of buildings at the sides of Laura Bassi street prevent the formation of vortices at a street scale. However, in some zones downstream Laura Bassi street recirculation flows are visible, involving around 3-4 building blocks. As a consequence, no peaks of high CO concentration are obtained, but a spreading of pollutant within these zones characterized by lower and more uniform pollutant concentration distribution.

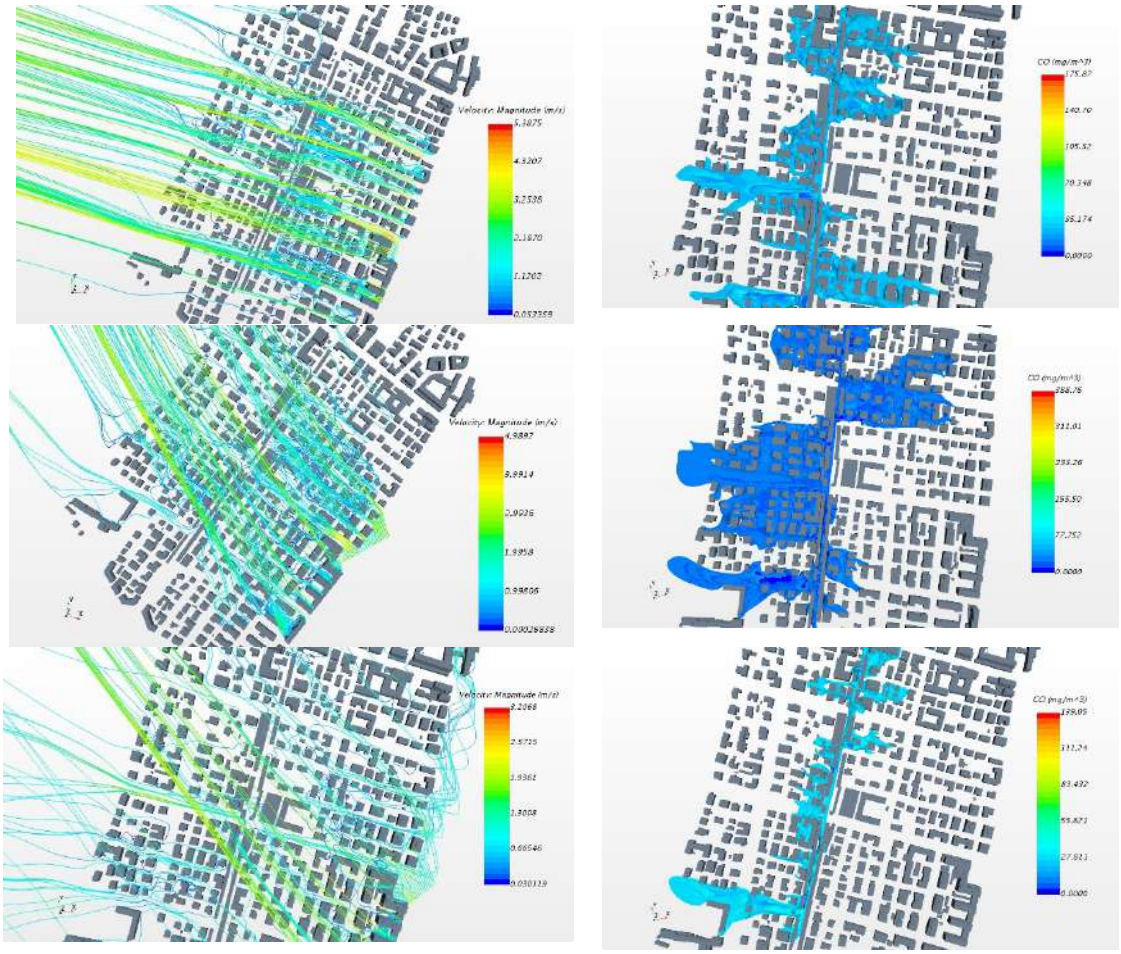

Figure 61: Laura Bassi street, summer evening. Case 22/08/2018 UTC 16:00 (top), UTC 18:00 (middle) and UTC 20:00 (bottom). Streamlines (left) and CO concentration (right).

Fig. 61 shows the streamlines and CO concentrations obtained for the evening hours, from UTC 16:00 to UTC 20:00. In particular, the wind directions for the two cases UTC 18:00 and UTC 20:00 are similar, as shown by Table 1 (138° and 151° respectively). In these cases, all the streets in the arrays of buildings are inclined with respect to the wind direction. Then, the channelling through Mezzofanti street is interrupted and many recirculation vortices are obtained around groups of 3-4 buildings. Also in these cases, no peaks of high CO concentration are obtained, but a spreading of pollutant within these zones characterized by lower and more uniform pollutant concentration distribution.

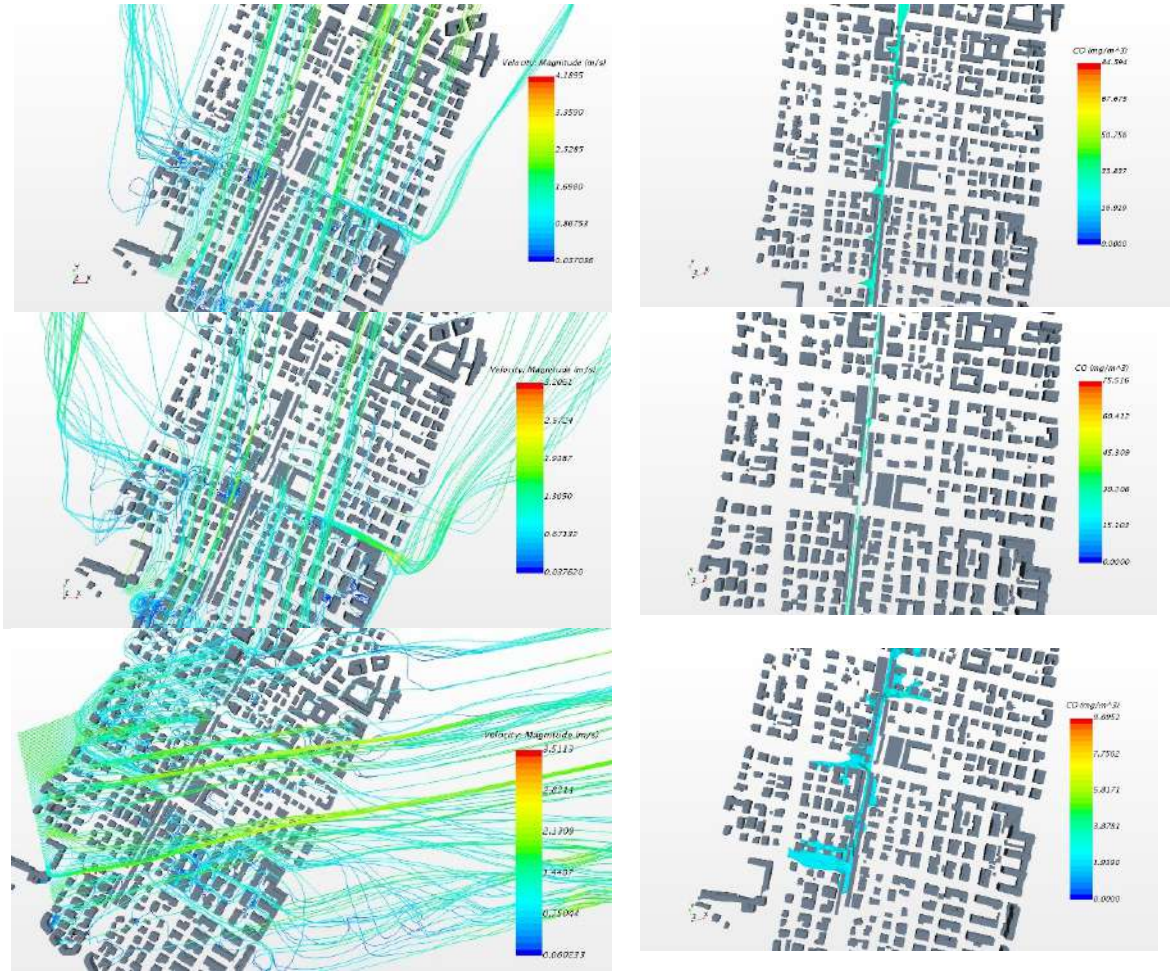

Figure 62: Laura Bassi street, summer night. Case 22/08/2018 UTC 23:00 (top), 23/08/2018 UTC 1:00 (middle) and UTC 3:00 (bottom). Streamlines (left) and CO concentration (right).

Fig. 62 shows the streamlines and CO concentrations obtained for the night hours, from UTC 23:00 (22/08/2018) to UTC 3:00 (23/08/2018). In the first two cases the wind direction is from South-West, but no strong channelling is observed along Laura Bassi street. In these cases, al the streets in the arrays of buildings are inclined with respect to the wind direction. The inhibition of channelling is caused by the presence of trees. Furthermore, the mixing is also inhibited in this region, resulting in a higher pollutant concentration distribution along the street.

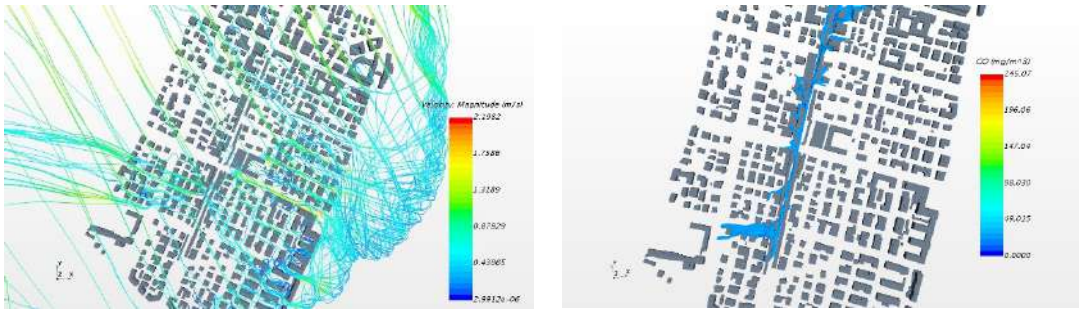

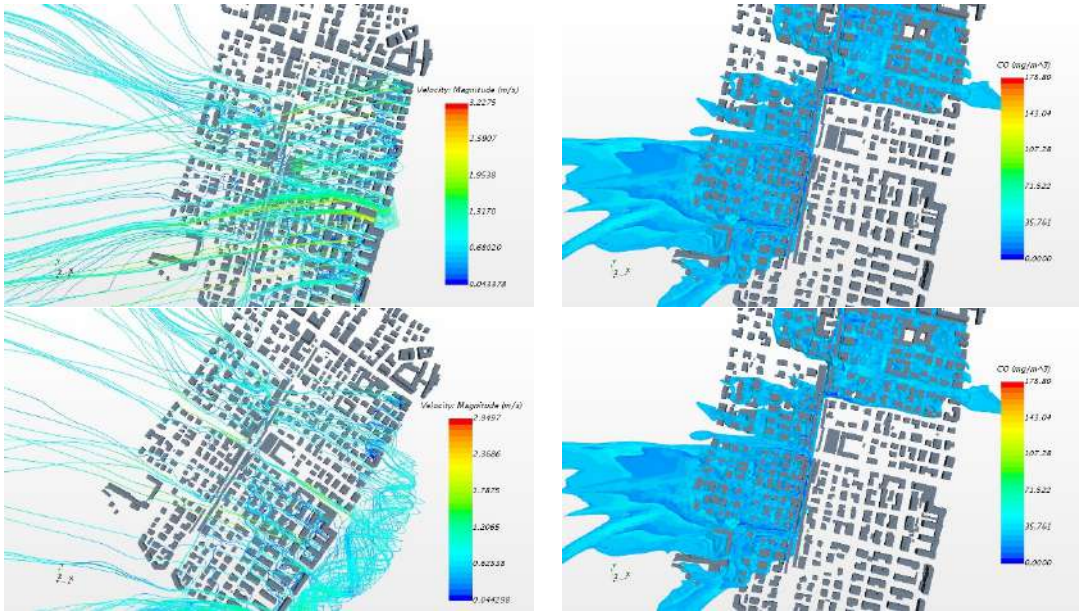

Figure 63: Laura Bassi street, summer morning. Case 23/08/2018 UTC 5:00 (top), UTC 7:00 (middle) and UTC 9:00 (bottom). Streamlines (left) and CO concentration (right).

Fig. 63 shows the streamlines and CO concentrations obtained for the summer morning hours, from 23/08/2018 UTC 5:00 to UTC 9:00. The wind direction for these cases forms angles 45° with both Laura Bassi street and Mezzofanti street. The situation is similar to that observed during the afternoon cases (UTC 16:00 and UTC 18:00). The channelling through the two main street is interrupted and many recirculation vortices are obtained around groups of 3-4 buildings. As a consequence, even in these cases no peaks of high CO concentration are obtained, but a spreading of pollutant within these zones characterized by lower and more uniform pollutant concentration distribution.

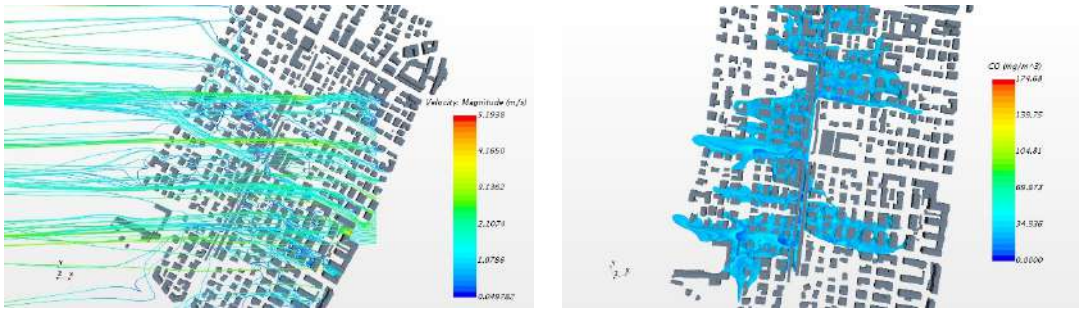

Figure 64: Laura Bassi street, summer noon. Case 23/08/2018 UTC 11:00. Streamlines (left) and CO concentration (right).

The same occurs for the case 23/08/2018 UTC 11:00, shown by Fig. 64. The channelling through the two main street is interrupted and many recirculation vortices are obtained around groups of 3-4 buildings. As a consequence, also results of this simulation does not present high peaks in CO concentration, but a spreading of pollutant within these zones characterized by lower and more uniform pollutant concentration distribution.

3.1.5 Laura Bassi street – winter

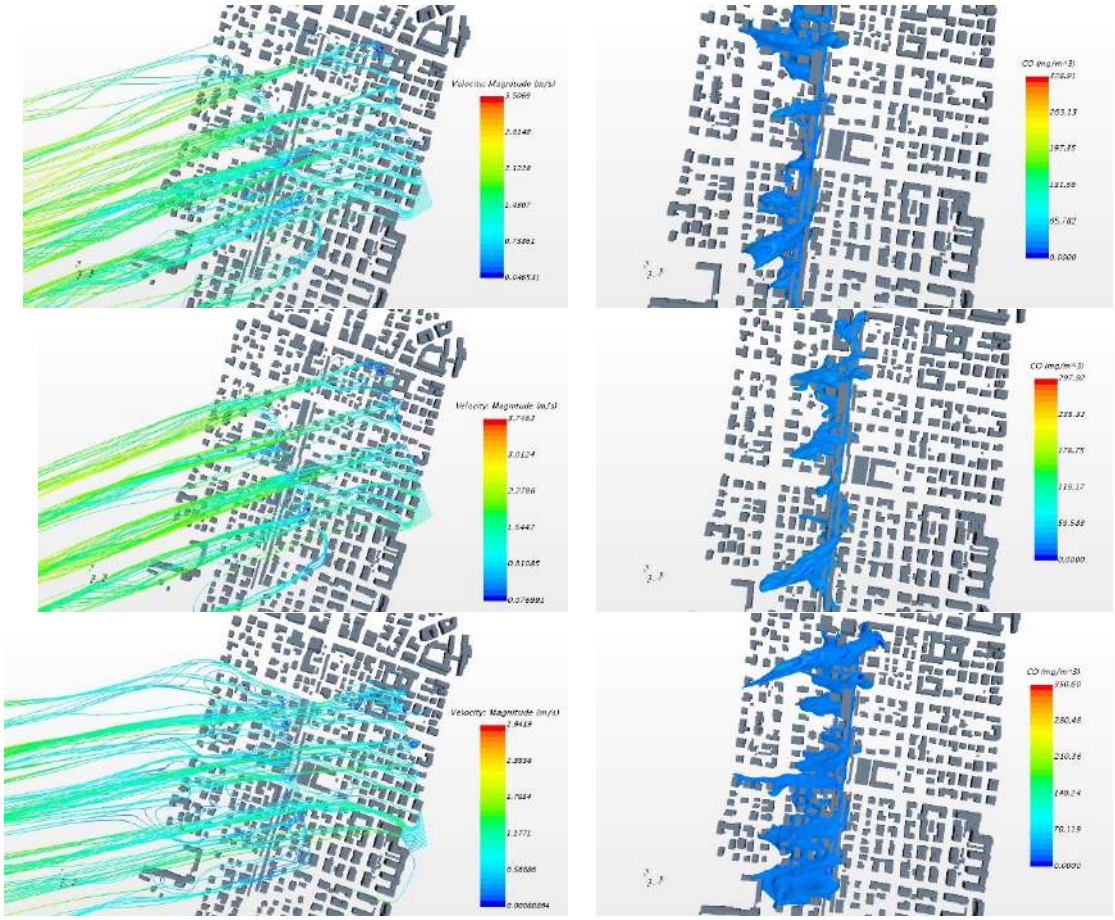

Figure 65: Laura Bassi street, winter afternoon. Case 08/02/2018 UTC 11:00 (top), UTC 13:00 (middle) and UTC 15:00 (bottom). Streamlines (left) and CO concentration (right).

Fig. 65 shows the streamlines and CO concentrations obtained for the winter afternoon hours, from UTC 11:00 to UTC 15:00. In particular, the wind directions for the two cases UTC 11:00 and UTC 13:00 are similar, as shown by Table 4 (75° and 79° respectively), with a higher wind velocity in the second case. The wind direction is inclined with respect to the streets in the array of buildings. Then, the channelling through the two main streets (Laura Bassi street and Mezzofanti street) is interrupted and many recirculation vortices are evidenced. In this case, unlike what observed in the summer cases, the pollutant spreads only downstream Laura Bassi street. During summer, large zones with pollutant spread even upstream Laura Bassi street have been observed (see for instance Fig. 64). The main difference between these summer and winter cases are the tree foliage, as the trees in that area are deciduous trees.

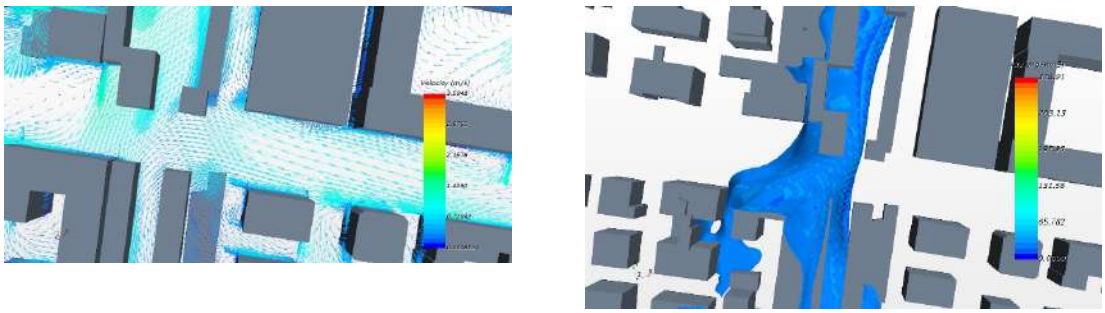

Figure 66: Laura Bassi street, winter afternoon. Case 08/02/2018 UTC 11:00. Wind velocity vectors (left) and CO concentration (right).

Fig. 66 shows velocity vectors and CO concentration obtained near the intersection between Laura Bassi street and Mezzofanti street for the case 08/02/2018 UTC 11:00. The figure shows that during winter, street scale vortices are present near the intersection where also trees are present but without foliage. As such, during winter, CO distribution is less uniform then in summer and CO concentration peaks may occur near the intersections.

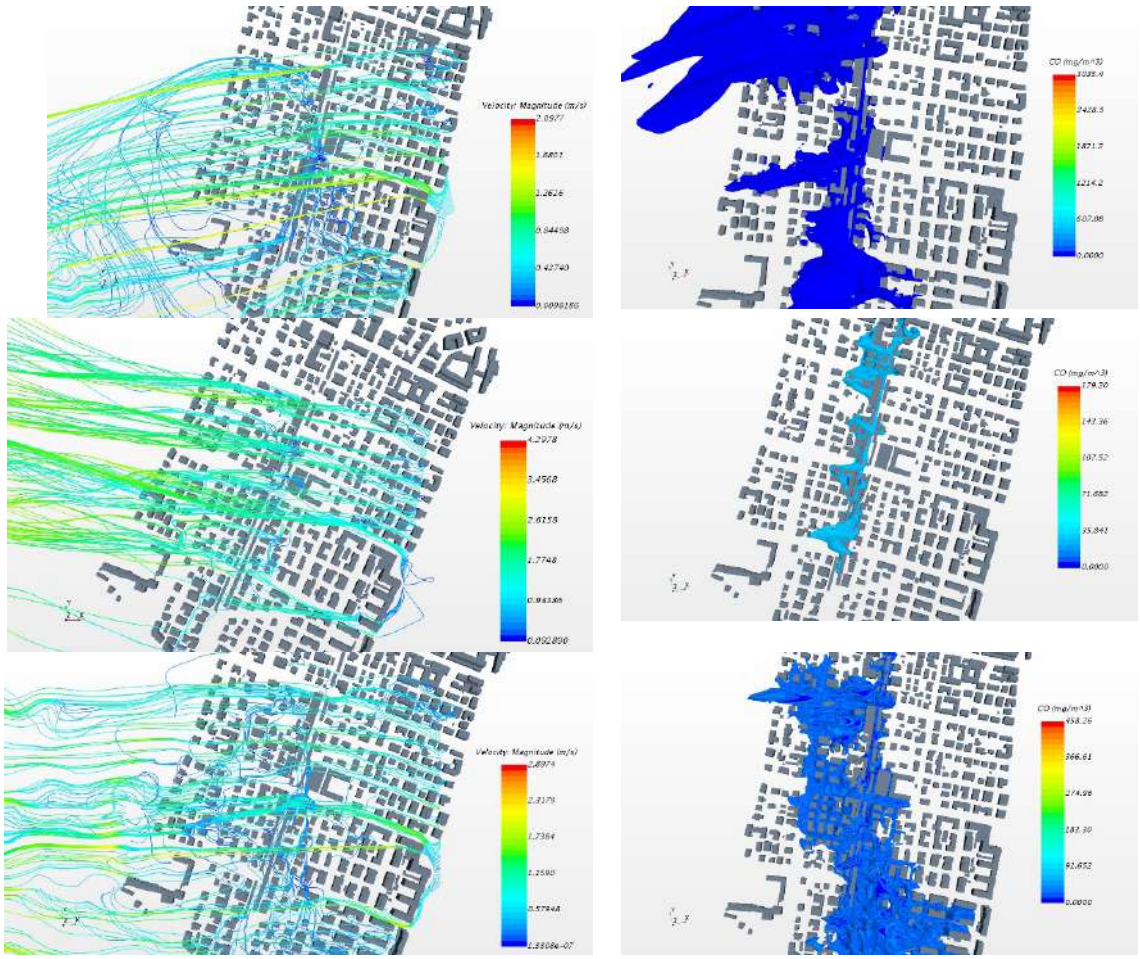

Figure 67: Laura Bassi street, winter evening. Case 08/02/2018 UTC 17:00 (top), UTC 19:00 (middle) and UTC 21:00 (bottom). Streamlines (left) and CO concentration (right).

Fig. 67 shows the streamlines and CO concentrations obtained for the winter evening hours, from UTC 17:00 to UTC 21:00. In particular, the wind directions for the two cases UTC 19:00 and UTC 21:00 are similar, as shown by Table 4 (101° and 96° respectively), with a higher wind velocity in the second case. The angle between Mezzofanti street and wind direction is about 20°. Then, the channelling through Mezzofanti street and the parallel streets is interrupted and many recirculation vortices are evidenced. In this case, pollutant diffusion is obtained.

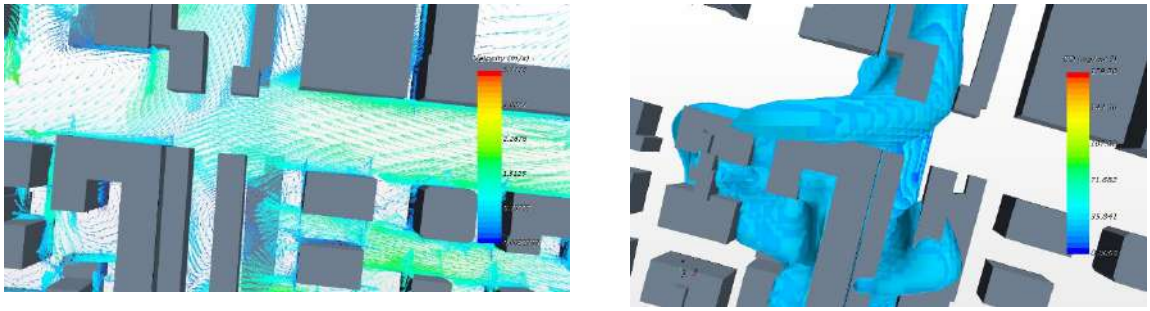

Figure 68: Laura Bassi street, winter evening. Case 08/02/2018 UTC 19:00. Velocity vectors (left) and CO concentration (right).

Fig. 68 shows velocity vectors and CO iso-surface obtained near the intersection between Laura Bassi street and Mezzofanti street for the case 08/02/2018 UTC 19:00. The figure shows that the vector map obtained for this case is very similar to that obtained for the case shown by Fig. 65 (relative to case 08/02/2018 UTC 11:00). The wind direction for the case shown by Fig. 65 is 75° while for this case is 101°. This means that for this building arrangement a 25° difference in the angle between wind direction and the streets does not affect the local flow structures around intersections.

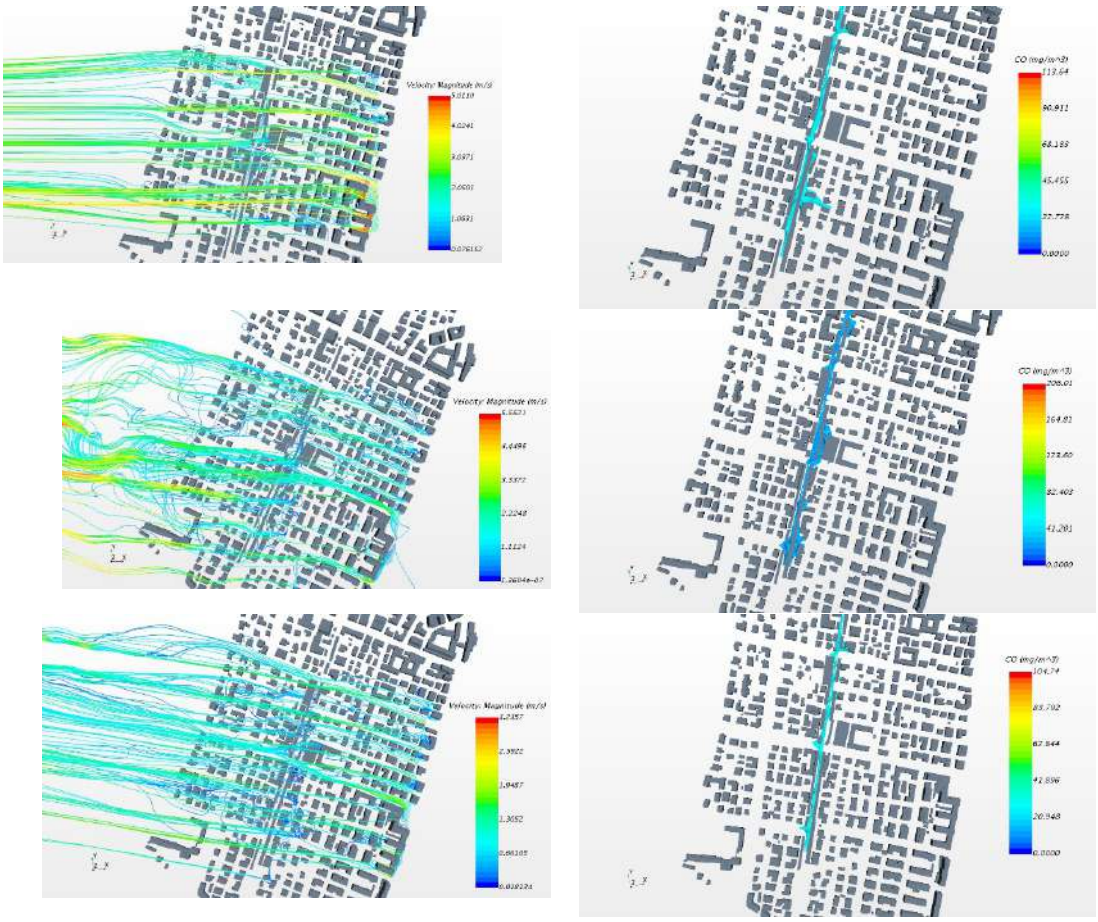

Figure 69: Laura Bassi street, winter night. Case 08/02/2018 UTC 23:00 (top), 09/02/2018 UTC 1:00 (middle) and UTC 3:00 (bottom). Streamlines (left) and CO concentration (right).

Fig. 69 shows the streamlines and CO iso-surfaces obtained for the winter night hours, from UTC 23:00 (08/02/2018) to UTC 3:00 (09/02/2018). The wind directions for the three cases are 100, 99 and 103 respectively, as shown by Table 4, with the highest wind velocity in the first two cases. The angle between Mezzofanti street and wind direction is about 20°. The pollutant distribution is very similar to that obtained for the case 08/02/2018 UTC 19:00, with lower concentrations as these cases refer to night.

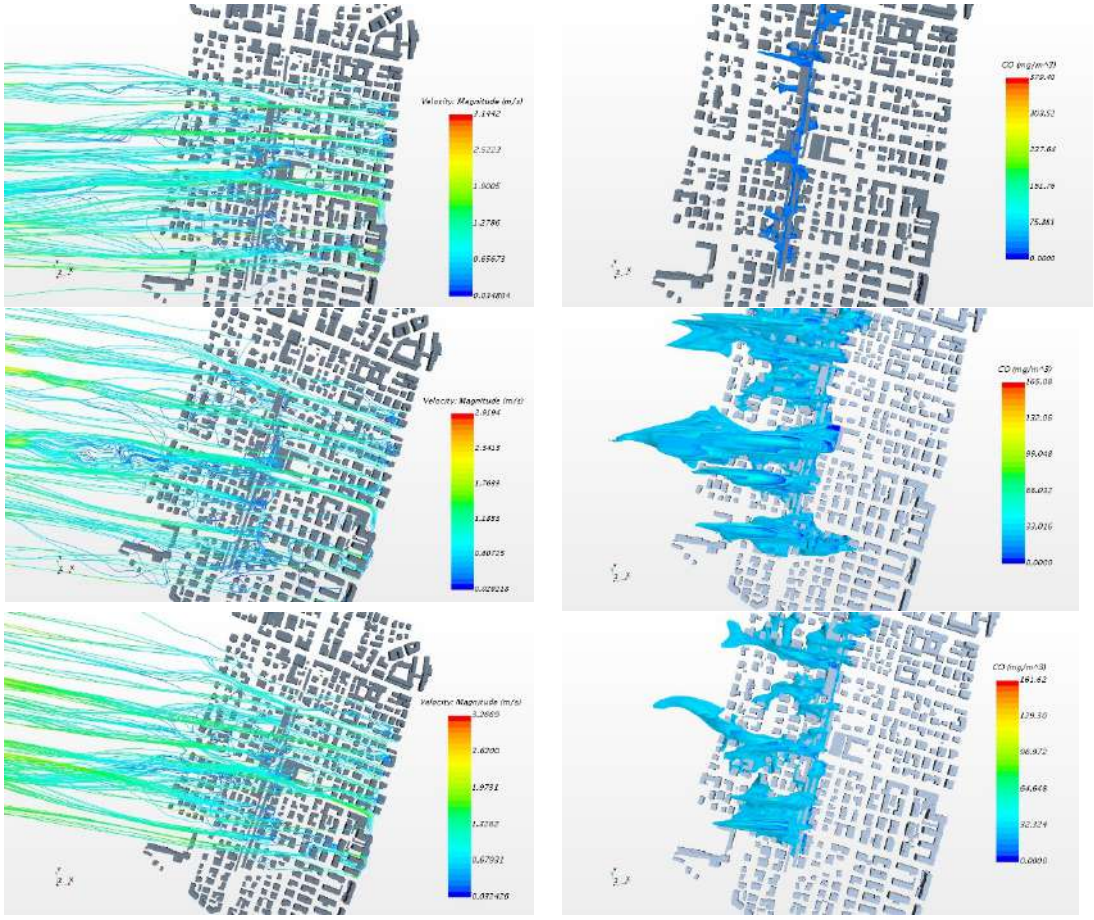

Figure 70: Laura Bassi street, winter morning. Case 09/02/2018 UTC 5:00 (top), UTC 7:00 (middle) and UTC 9:00 (bottom). Streamlines (left) and CO concentration (right).

Fig. 70 shows the streamlines and CO iso-surfaces obtained for the winter morning hours, from UTC 5:00 (09/02/2018) to UTC 9:00. The wind directions for the three cases are 107°, 103° and 104° respectively, as shown by Table 4, with the wind velocity in the range between 1.5 and 2.3 m s^{-1}. The pollutant distribution is very similar to the evening and night cases (shown by Figs. 67 and 69), with higher CO values as these cases refer to peak traffic time.

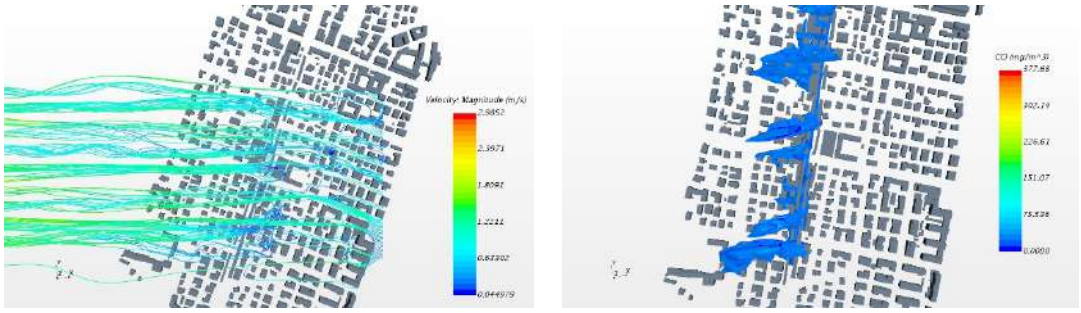

Figure 71: Laura Bassi street, winter noon. Case 09/02/2018 UTC 11:00. Streamlines (left) and CO concentration (right).

The same occurs for the case 09/02/2018 UTC 11:00, shown by Fig. 71. As provided in Table 4 the wind direction for this case is 94°, with the wind velocity equal to 0.75 m s^{-1}. The pollutant distribution is very similar to that obtained in the previous cases.

3.1.6 Laura Bassi street – results

In this section Laura Bassi street canyon modelling investigation has been outlined to determine the effect of trees on pollutant distribution. In particular, the normalised flow rate by the reference flow rate far upstream the buildings array (according with Buccolieri et al., 2010) has been investigated. Quantification of the differences in normalised flow rates at the top of Laura Bassi street is provided in Table 21. The table displays the results for the normalised flow rates in function of the presence of trees under different wind conditions.

Wind direction	Q* with trees	Q* without trees
Parallel	0.21	0.55
45°	0.24	0.43
Perpendicular	0.26	0.39

Table 22: Normalised flow rates.

The table refers to Laura Bassi street, i.e. parallel means that the wind direction is parallel to Laura Bassi street axis, 45° means that the angle between Laura Bassi street and wind direction is 45° and perpendicular means that the wind direction is perpendicular to Laura Bassi street axis. As the angle between Laura Bassi street axis with the North-South direction is 35°, the first condition means that the wind direction angle with the North-South direction is about 35° or 215° in the first case, 80° or 260° in the second and 125° or 305° in the third case. Table 21 displays the flow rates evaluated at Laura Bassi street top normalised with the reference flow rate far upstream, for all the wind directions. The flow rate is always reduced by the presence of trees. For parallel wind direction, the flow rate is reduced by 60% because of the presence of trees, while for wind direction forming an angle of 45° and perpendicular with the street axis the reductions are about 50% and 33%, respectively. Therefore the presence of trees reduces the ventilation at the street level. Nevertheless, the presence of trees reduces the presence of recirculation vortices near the intersections, and as such the pollutant distribution is more uniform and the hotspots are mitigated. This effect is investigated with more details through the two scenarios analysed in the following subsections.

Analysis of different scenarios

The case of 22/08/2018 UTC 12:00 has been chosen as a reference, as during summer the effect of trees is more relevant. In this section, two scenarios have been analysed: the case of Marconi street with a line of trees similar to the ones analysed in Laura Bassi street, and the case of Laura Bassi street without trees.

First scenario: Marconi street with trees

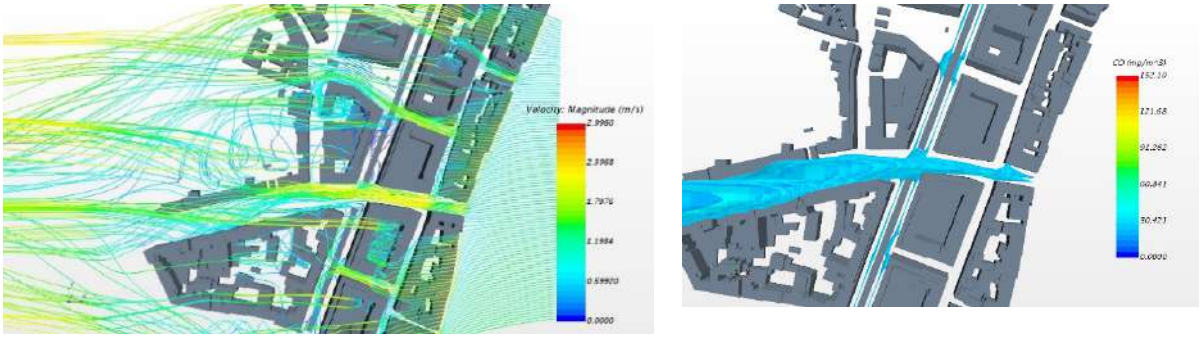

Figure 72: Marconi street, summer. Case scenario 22/08/2018 UTC 12:00 obtained by placing a line of trees in the middle of Marconi street. Streamlines (left) and CO iso-surfaces (right).

Fig. 72 shows the streamlines and CO iso-surfaces obtained for the summer case at noon, 22/08/2017 UTC 12:00. The wind direction for this case is 93°, as shown by Table 4, with the wind velocity equal to 4.4 m s^{-1}. By comparing Fig. 72 with Fig. 47, it can be observed that the flow field obtained for this scenario is very different to that obtained for the real Marconi street. The presence of trees inhibits the formation of recirculation vortices at the street intersection between Marconi street and Riva Reno street. As a consequence, the pollutant distribution obtained for the scenario with trees is also very different, as no CO concentration peaks are visible on the lateral sides of the TI. These differences are shown in Fig. 73.

The figure shows velocity vectors and CO iso-surfaces obtained near the intersection between Marconi street and Riva Reno street for the case 22/08/2017 UTC 12:00, for the real case without trees (top) and for the scenario with trees (bottom). The vector map obtained for the case with trees shows a main flow on Riva Reno street with secondary flows from the two sides of Marconi street, dragged by the main flow without the creation of vortices. This flow enhances the pollutant transfer between the streets at the intersection, driven by the mixing at the TI. As a result, the local pollutant concentration obtained in Marconi street is lower in the case of the presence of trees with respect to the real case.

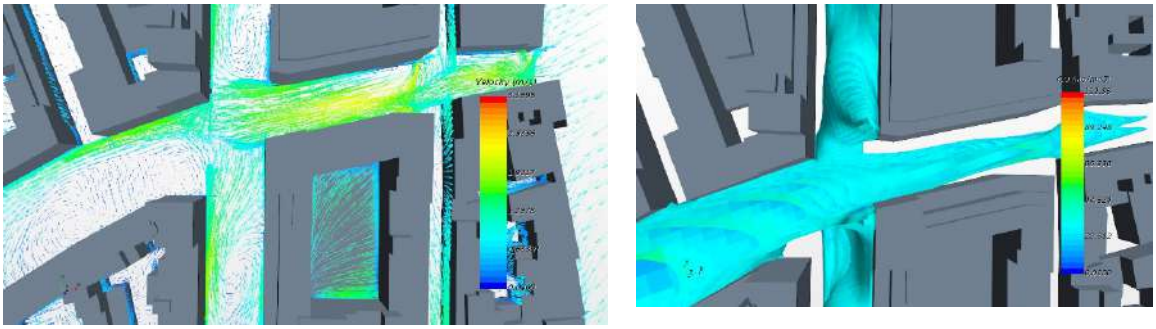

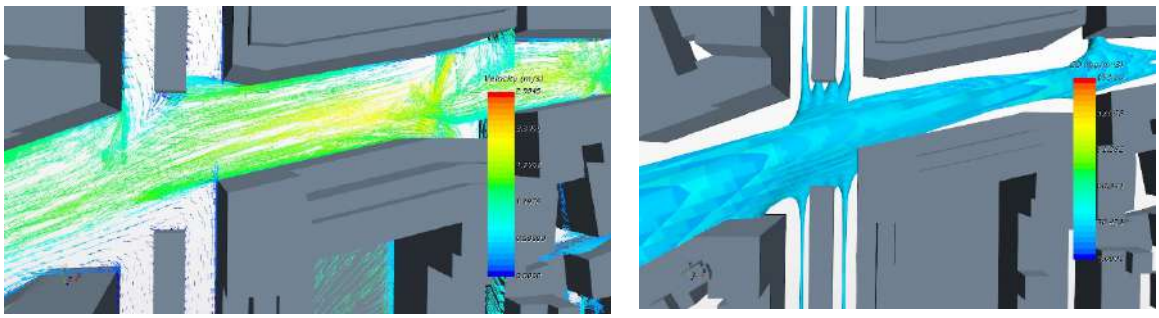

Figure 73: Marconi street, summer. Case scenario 22/08/2018 UTC 12:00. Velocity vectors obtained near the intersection (left) and CO iso-surfaces (right). Top: real case described in Figure 47. Bottom: case scenario obtained by placing a line of trees in the middle of Marconi street.

Second scenario: Laura Bassi street without trees

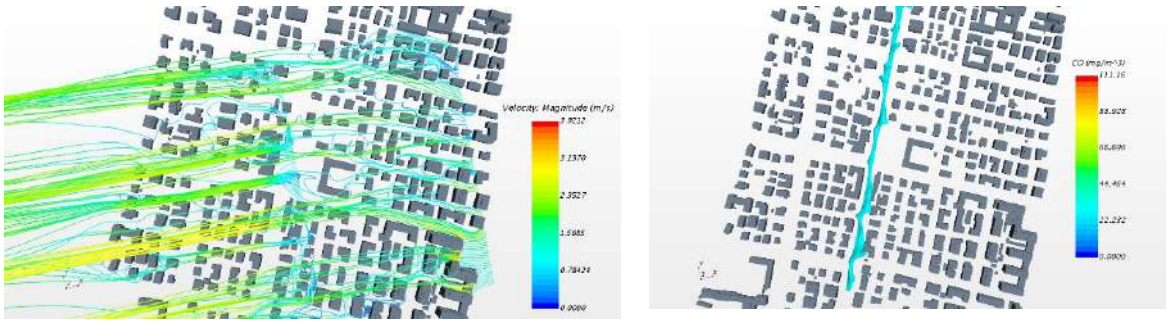

Figure 74: Laura Bassi street, summer. Case scenario 22/08/2017 UTC 12:00 obtained by removing the trees in Laura Bassi street. Streamlines (left) and CO iso-surfaces (right).

Fig. 74 shows the streamlines and CO iso-surfaces obtained for the summer case at noon, 22/08/2017 UTC 12:00. The wind direction for this case is 93°, as shown by Table 4, with the wind velocity equal to 4.4 m s^{-1}. By comparing the streamlines in Fig. 74 with the ones in Fig. 60, it can be observed a reduction in the recirculation flow for the case without trees. The presence of trees reduces the velocity at street level, enhancing a sort of under-trees recirculation flow. As a consequence, the pollutant distribution obtained for the scenario with trees is very different to that obtained without trees, as the mixing with the top layers is enhanced and the pollutant CO levels at street level are lower. These differences are shown in Fig. 75.

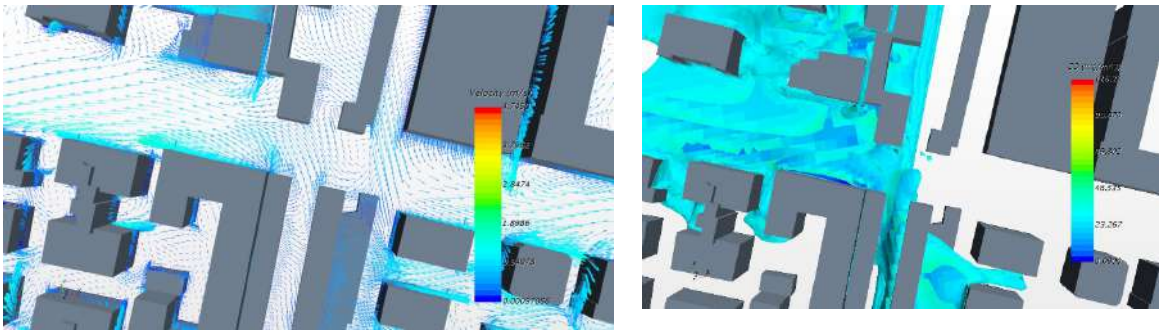

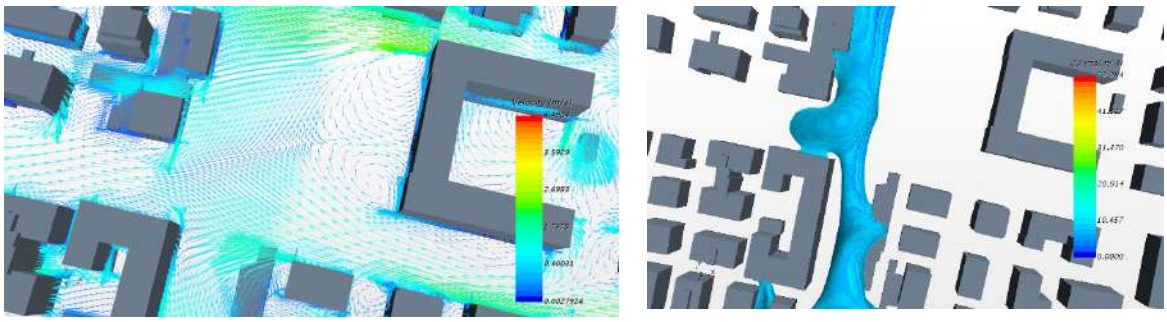

Figure 75: Laura Bassi street, summer. Case scenario 22/08/2018 UTC 12:00. Velocity vectors obtained near the intersection (left) and CO iso-surfaces (right). Top: real case described in Fig. 60. Bottom: case scenario obtained by removing trees in Laura Bassi street.

The figure shows velocity vectors and CO iso-surfaces obtained near the intersection between Laura Bassi street and Mezzofanti street for the case 22/08/2017 UTC 12:00, for the real case with trees (top) and for the scenario without trees (bottom). The vector map obtained for the case with trees shows a low velocity vectors near the crown trees, resulting in a higher pollutant diffusion through Mezzofanti street. On the contrary, in the case without trees, recirculation vortices at the sides of the intersection promote mixing which results in lower average concentrations. In summary, the average pollutant concentration obtained in Laura Bassi street is lower in the scenario without trees with respect to the real case, but in the scenario local pollutant concentration peaks (hotspots) are present near the intersections.

The effect of green roofs

Lazzaretto site with green roofs and green facades

In order to investigate the effects of green roofs on pollutant concentration within real street canyons, a third scenario has been analysed, by considering the case of Lazzaretto site entirely covered by green roofs. Two green facades have been added to the building walls within the street canyon A (as shown in Fig. 4). To model the green roofs, a sink of pollutant has been added to the mass conservation equation, according with equation 12 that takes into account of a deposition velocity as the one considered for the previous cases. Moreover, a sink of energy has been added, according with equation 15. The case considered is the 17/08/2018 UTC 14:00. The results have been compared with the ones referring to the site as it is, on the same day, i.e. without the green roofs. The results are shown as follows:

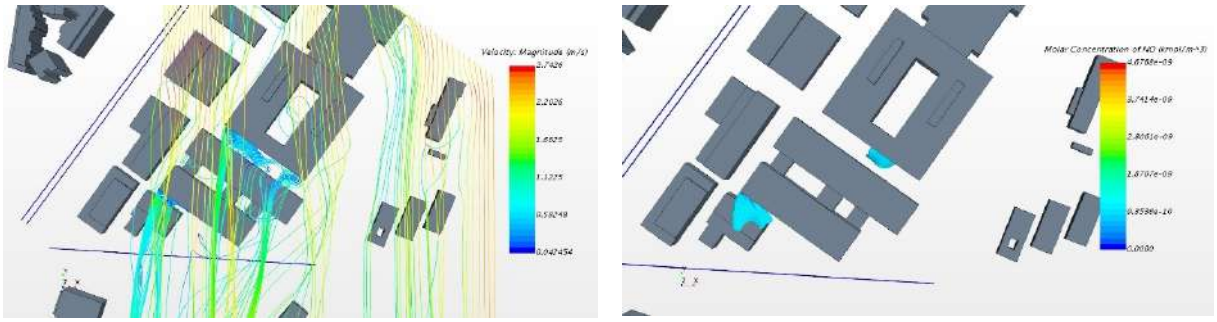

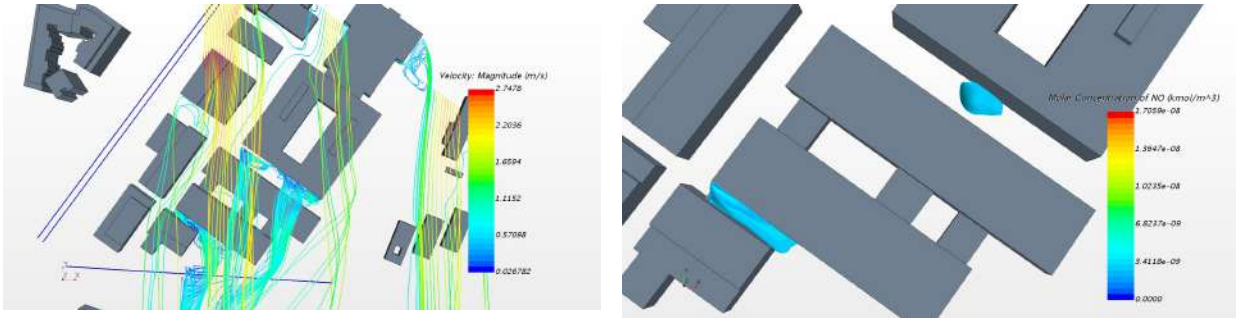

Figure 76: Lazzaretto site, summer. Case scenario 17/08/2018 UTC 14:00. Streamlines (left) and NO iso-surfaces (right). Top: real case described in D3.6. Bottom: case scenario obtained with green roofs and green facades. NO concentration are expressed in kmol/m³, (1 kmol/m³ = 30· 10⁹ µg/m³).

Fig. 76 shows the streamlines and NO iso-surfaces obtained for the summer case 17/08/2018 UTC 14:00. The wind direction for this case is 8° and the wind velocity is 2.8 m s^{-1}. By comparing the streamlines in Fig. 76 (left, top) with the ones in Fig. 76 (left, bottom), one can see that less stagnation flow is obtained within the street canyons for the case with green roofs. The presence of GIs then reduces the velocity at street level and modifies the pollutant distribution close to the walls. These differences are shown in Fig. 77.

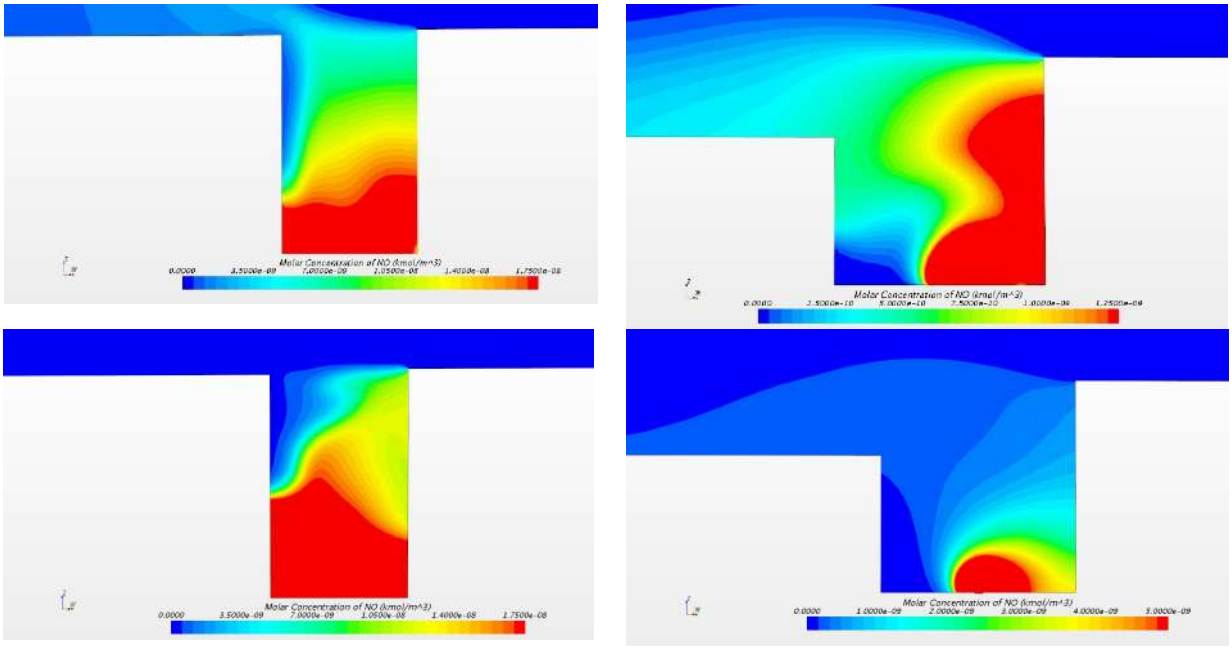

Figure 77: Lazzaretto site, summer. Case scenario 17/08/2018 UTC 14:00. NO concentrations (right). Top: real case described in D3.6. Bottom: case scenario obtained with green roofs and green facades.

The results show that the main effect of green roofs is to modify the local pollutant because of the modification of the flow field, while the effect of pollutant deposition is negligible. However, this effect could be important by considering the deposition of particles instead of a gaseous pollutant.

3.2 Guildford

The simulation study primarily aimed to understand the flow modification created by the presence of GI and compare with the experimental results obtained, in order to develop recommendations on GI design in D7.2 '*Generalised recommendation on PCS*', Parallel wind flow condition was one of the predominant wind directions at the selected monitoring site. In this wind flow condition, wind speed varied from 3.5 to 7.6 m s^{-1}, which was simulated in the model. Fig. 78 shows input velocity and the developed log wind profile in along the street as contour plots. The velocity above the street matched to the measured wind profile. Detailed wind direction and flow calibration of the model is still under progress. Experimental study conducted at this monitoring location revealed maximum reduction in pollutant concentration in parallel (to the road and hedge) wind condition followed by perpendicular wind flow (Abhijith and Kumar, 2019). We looked into the flow features created in this wind direction to understand the role of GI in reducing pollutant concentration behind the hedge.

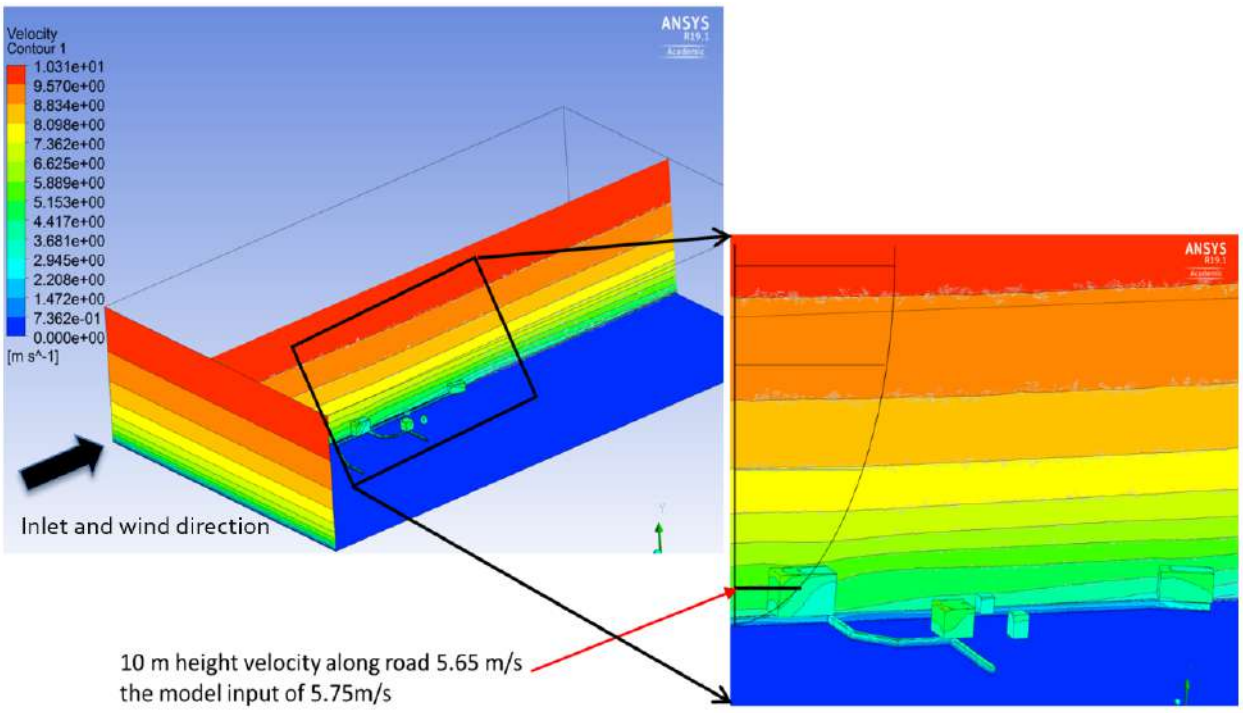

Figure 78: Contours showing velocity profiles at inlet and at a plain passing through the street. Enlarged section shows resulting wind profile and the wind velocity at 10 m height.

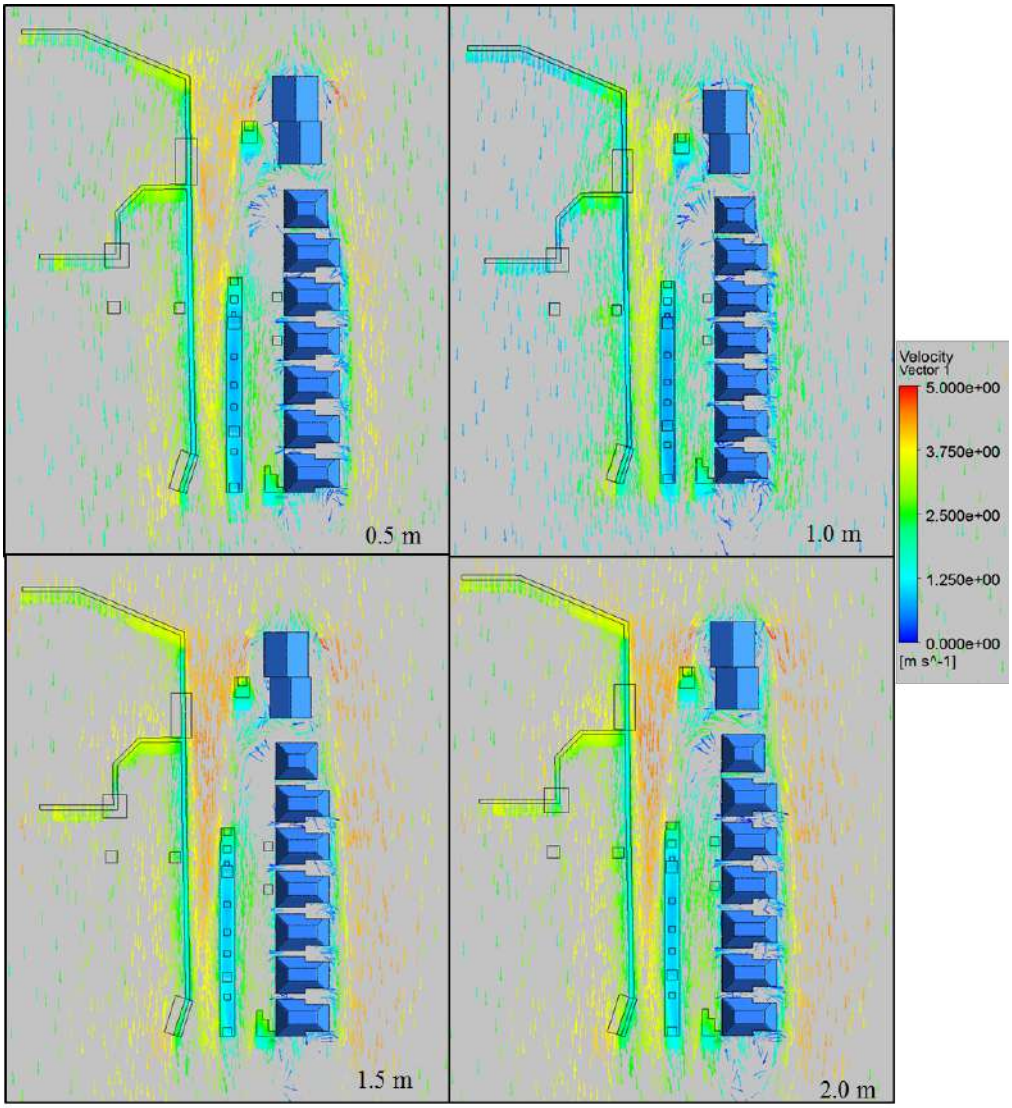

Figure 79: Velocity vectors showing longitudinal wind flow conditions at 0.5, 1, 1.5 and 2 meters height along the road.

The velocity vector profiles at different heights around the breathing level were plotted to understand the flow change near hedges. The direction of the flow as well as the velocity magnitude at that level was also provided. Four longitudinal sections with different heights such as 0.5, 1, 1.5, and 2 m were selected for analysing velocity vector profiles as shown in Fig. 79. In the figure, blue boxes show the building on the right side of the figure, the other side of the street has long hedge row along the road and in the middle there is a hedge with trees. In parallel flow, the velocity vectors displayed higher velocity magnitude along the centre of the road and a gradual decrease in the velocity magnitude towards the hedge. This trend in magnitude of the velocity was observed in the all investigated heights. As expected, the lowest height (1 m) showed least velocity magnitude compared to all studied sections at higher elevations. The GIs on the both sides, directed and aligned the wind flow towards the centre of the street, made a channel along the length of the street. This flow pattern was observed in all different studied heights. Compared to street canyon environment, there are less hindrances to the wind flow in open road

conditions and wind flow can be altered considerably by the manmade structures as well as natural objects. All vector profiles display very negligible wind flow across both hedge and combination of hedge and trees. The experimental work reported 52, 30, 31, 17 and 15% reduction in black carbon, particle number concentrations, PM_1, $PM_{2.5}$ and PM_{10}, respectively, on parallel wind conditions (Abhijith and Kumar, 2019). The reduction was higher compared to the perpendicular wind condition. The well-defined flow separation and less flow penetration across the hedge row may be the reason for improved air quality behind GI in parallel wind condition observed in field studies. Completion of simulation analysis is expected to provide more insights in this pollution reduction mechanism.

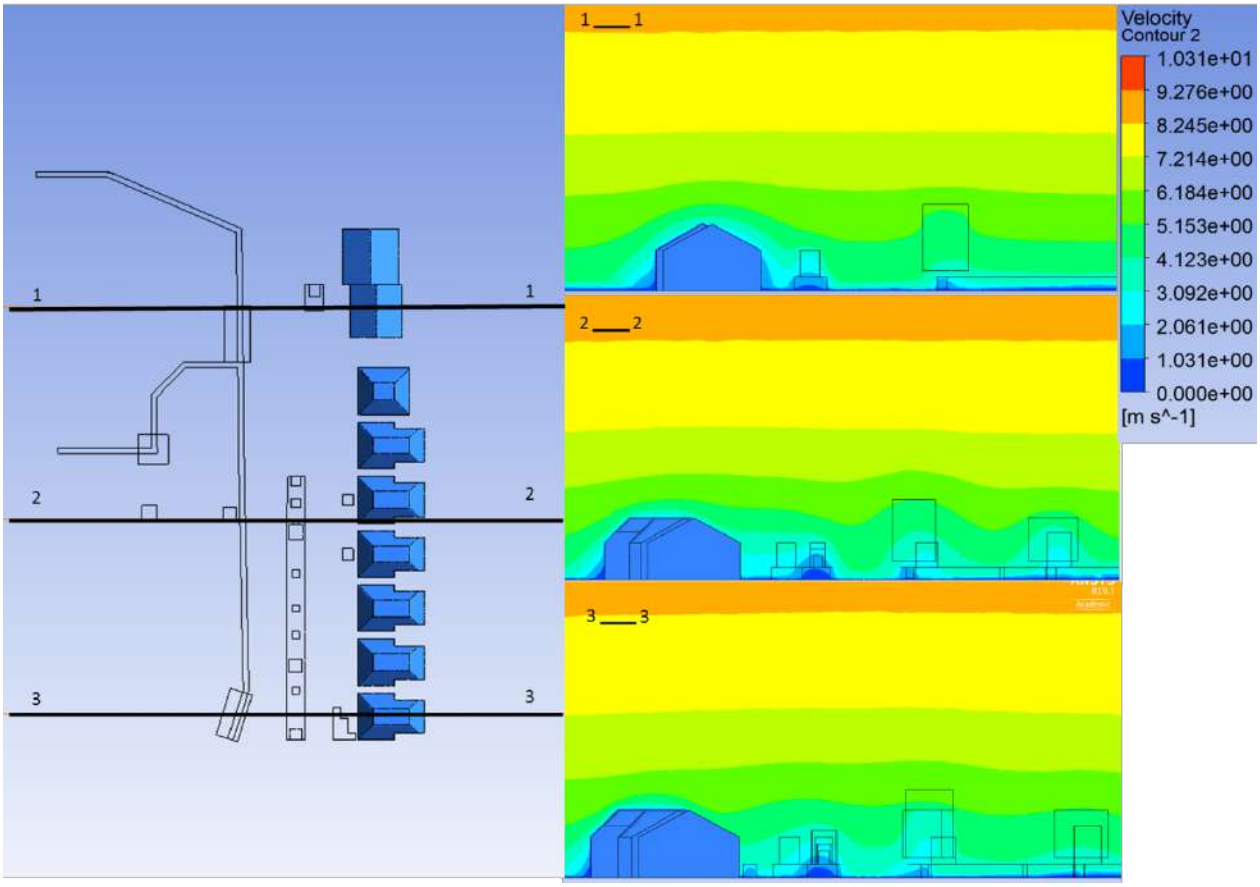

Figure 80: Velocity contour at different sections in the starting (section 1_1), towards center (section 2_2), and end of the street (section 2_2).

Similar to the velocity vectors at different plans, we analysed the velocity contours at different cross-sections locations as shown in the Fig. 80. The velocity contours displayed flow stratification around the buildings and the hedges. There is a distinct low velocity region around vegetation which suppressed the wind flow across the hedge as observed in the vector plots. A well-defined channel was observed along the street which enabled higher wind velocity at the center of the road compared to nearby areas of the hedge rows. Contour plots complement the velocity vector plots. Both velocity vectors and contours provided possible explanations for higher pollutant reduction observed in the experimental study.

Furthermore, velocity flow conditions such as perpendicular wind direction and different wind speeds are investigated in addition to proposed scenario analysis to better understanding of pollutant dispersion around GI in open road conditions. Lastly, influence of vegetation height, thickness and density are yet to be analysed and these are expected to be included in the D7.2 as generalized recommendations to be implemented by policymakers and interested citizens.

3.3 Dublin

This section outlines the Pearse Street modelling investigation to determine the effect of implementing a LBW passive control structure. Quantification of the reductions or increases in pollutant concentrations on the footpaths after the introduction of the passive control (LBW) in the Pearse Street model were provided in Table 22. The table displays the results for the percentage difference in pollutant concentrations in the LBW passive control model for Pearse Street in different wind conditions.

Predominant Wind Direction	Traffic	Footpath Monitor Location			
		North-West	South-West	North-East	South-East
Parallel	Peak	(19-20%)	5-6%	(5-6%)	(0-2%)
	Off-Peak	(21-22%)	7-8%	(8-9%)	(0-1%)
Perpendicular	Peak	2-3%	(14-21%)	16-17%	3-5%
	Off-Peak	(1-2%)	(24-25%)	18-19%	(5-6%)
Predominant	Peak	(3-5%)	6-7%	(1-3%)	31-36%
	Off-Peak	(0-1%)	4-5%	4-5%	28-31%

Note: Negative percentage differences in pollutant concentrations are indicated by values in brackets

Table 23: Percentage difference in pollutant concentration between reference and LBW's model at peak & off-peak times for different wind directions.

The results displayed both reductions and increases in pollutant concentrations on the footpaths in the parallel wind models due to the introduction of the footpath LBWs. The results of the parallel wind speed model displayed increases of up to 22% and 9% on the North-West and North-East footpaths, respectively. Only a small difference was measured of up to 4% in peak and off-peak traffic conditions. On the South side of the street canyon, a reduction of up to 8% was measured on the South-West section of the footpath and an increase of up to 2% was calculated on the South-East footpath. The results were similar on these sections of the footpath (maximum 2% difference) in both peak and off-peak traffic times.

In perpendicular wind conditions, the results showed improvements in air quality of up to 3% and a deterioration of 2% on the North-West footpath for peak and off-peak traffic conditions, respectively. Reductions ranging from 16% to 19% were calculated on the North-West footpath section in peak and off-peak traffic conditions. Increases of up to 21% and 25% were calculated in peak and off-peak traffic on the South-West footpath. A reduction of up to 5% occurred on the South-West footpath in peak traffic conditions, with up to a 6% increase occurring in off-peak traffic conditions. Similar results were observed on both footpaths (average difference of 7%) for both peak and off-peak traffic conditions.

In the predominant wind models, the results showed deteriorations in air quality of up to 5% on the North-West footpath for peak and off-peak traffic conditions. An increase in pollutant

concentrations of up to 3% was calculated on the North-West footpath section in peak traffic, yet a 5% improvement in air quality was measured in off-peak traffic conditions. Reductions of up to 7% and 36% were calculated in peak and off-peak traffic on the South-West and South-East footpaths, respectively. Similar results were observed on both sections of the southerly footpath (differences of 2% and 7%) between both peak and off-peak traffic conditions.

3.3.1 Discussion on LBW model

The LBW model included boundary walls along both sides of the canyon with gaps for road junctions and bus stops. Therefore, the results were expected to be realistic. Fig. 81 to Fig. 84 shows the dispersion of pollutants in the Pearse Street canyon model for the LBW models in different wind conditions. Fig. 81 displays the plots of the west section of the LBW model in parallel wind conditions.

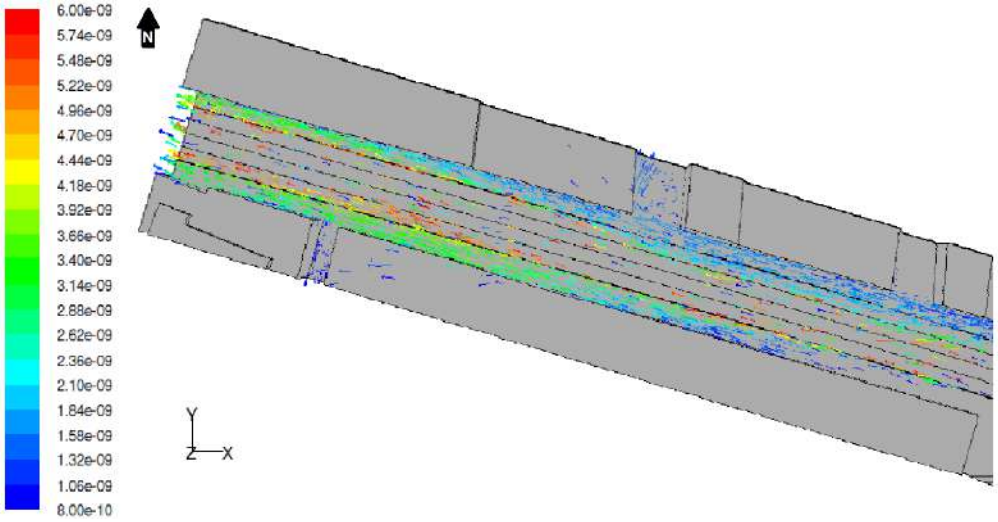

Figure 81: Plots of pollutant concentrations (kmol m^{-3}) as velocity vectors on west side of the canyon for the lbws model at a wind speed of 2.5 m s^{-1} in perpendicular wind conditions.

The 0.5 m LBW displayed improvements and deteriorations in air quality on the west sections of the North and South footpaths in parallel wind conditions. The results show no significant difference for the percentage difference in pollutant concentrations between peak and off-peak traffic distributions. The wind transported pollutants along the street canyon and increases in pollutant concentrations of between 19% and 22% was calculated on the North-West section of footpath. In contrast, an improvement in air quality of between 5% and 8% was noted on the South-West footpath as the LBW provided a baffle to pollutants from the road. The LBWs trapped air on the footpaths causing a change in the pollutant concentrations. The increase on the North-West footpath and decrease on the South-West footpath was due to the channelling of the wind towards the North-West footpath. This direction was caused by the slight change in orientation of Pearse Street at the midpoint of the street. The patterns of pollutant dispersion at street level on the East side of the street for the LBWs model are shown in Fig. 82.

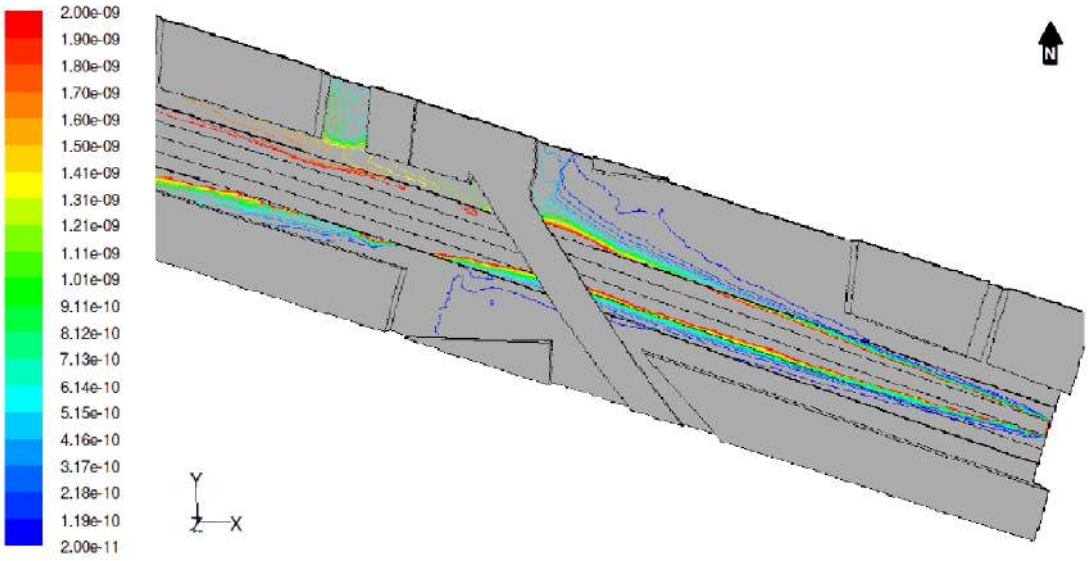

Figure 82: Plots of pollutant concentrations (kmol m^{-3}) as contours on east side of the canyon for the lbws model at a wind speed of 2.5 m s^{-1} in parallel wind conditions.

The air quality on the footpaths on the east side of the canyon showed small deteriorations in air quality with the introduction of the footpath LBWs. An increase of up to 9% and 2% was calculated on the North-East and South-East footpaths, respectively. The pollutant concentrations increased on the footpaths as pollutants were transported over the wall as air travelled along the canyon and were trapped on the footpaths. The difference between air quality in the peak and off-peak models was due to the shift of traffic between lanes, but did not display a notable influence on the performance of the LBWs. The pollutant concentration in the LBWs model with perpendicular wind conditions is displayed in Fig. 83.

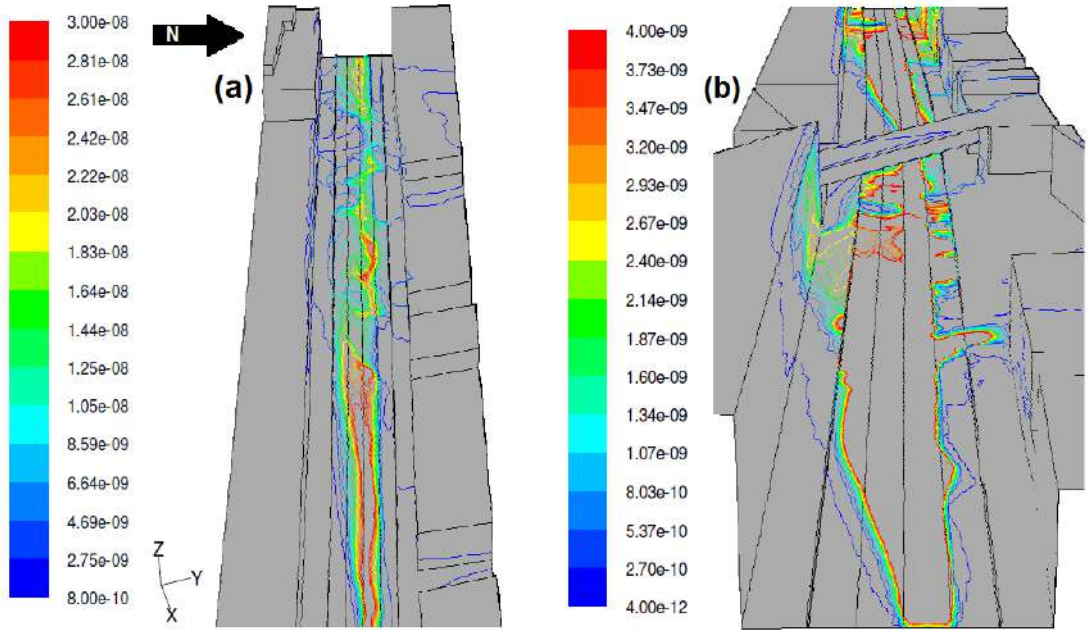

Figure 83: Plots of pollutant concentrations (kmol m^{-3}) as velocity vectors on (a) west and (b) east sides of the canyon for the lbws model at a wind speed of 2.5 m s^{-1} in perpendicular wind conditions.

On the west side of the canyon (Fig. 83), both increases and reductions were observed on the footpaths. A small reduction of up to 3% in the pollutant concentrations was measured on the North-West sections of footpath in peak traffic, with an inverse increase of 2% in off-peak traffic conditions. The South-West footpath demonstrated increases in pollutant concentrations of up to 21% and 25% in peak and off-peak traffic, respectively. The LBW does not provide an effective passive control on the South-West footpath as the North-West LBW trapped pollutants in the street and the wind brought an increased fraction towards the South-West footpath.

The air quality on the footpaths on the east side of the canyon showed improvements with the introduction of the footpath LBWs for peak traffic conditions. Reductions of up to 17% and 5% were calculated on the North-East and South-East footpaths, respectively. The LBWs channelled the polluted air along the centre of the canyon, improving air quality on the footpaths. A similar reduction of up to 19% was measured on the North-East footpath in off-peak conditions, yet a deterioration in air quality on up to 6% was noted on the South-East section of footpath in similar off-peak traffic. The shift of traffic distribution between lanes, notably the distribution of the 15% of traffic from Lane 4, allowed for more pollutant to be released closer to the southern side of the canyon and subsequently transported over the LBW. Fig. 84 displays the patterns of pollutant dispersion in the canyon for the LBW passive control model.

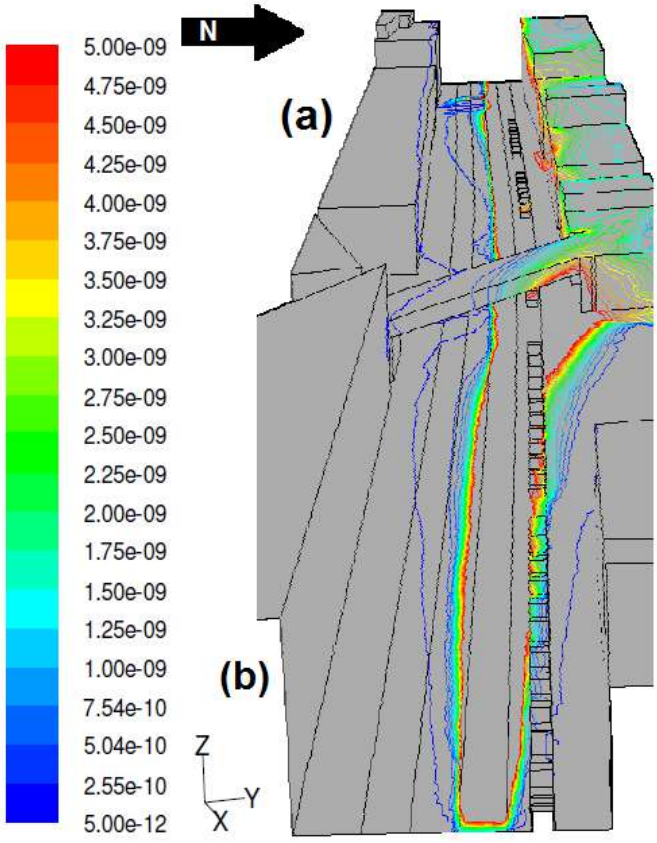

Figure 84: Plots of pollutant concentrations (kmol m^{-3}) as velocity vectors on (a) west and (b) east sides of the canyon for the lbws model at a wind speed of 2.5 m s^{-1} in predominant wind conditions.

The LBW displayed a small increase in the pollutant concentrations of up to 5% on the North-West footpath and a reduction of up to 7% on the South-West footpath. The off-peak traffic conditions did not significantly influence air quality on the footpaths as the LBWs provided similar changes in pollutant concentrations with the alternate distribution of traffic in the street. The wind direction produced lateral dispersion above the LBWs and thus no significant improvements in air quality were found for the predominant wind model in the west side of the canyon.

The air quality on the North-East section of the footpath marginally changed from a maximum 3% increase in pollutant concentrations in peak traffic to a 5% reduction in off-peak traffic. On the South-East footpath, the predominant wind direction and LBW provided an effective passive control with reductions of up to 36% and 31% in peak and off-peak traffic, respectively. The LBW trapped clean air on the South-East section of footpath creating a zone of clean air in the street. Overall, the LBWs did not provide a convincing passive control in most footpath sections, with the exception of the South-East section.

4 Conclusions

Detailed microscale CFD evaluation of PCS impacts on air quality has been studied in the deliverable. The impacts of trees, hedges, green roofs and green façades photocatalytic coatings, and low boundary walls were simulated in both open road and street canyon locations at different meteorological conditions. The effectiveness of these PCS on improving air quality was evaluated. Further analysis of obtained results as well as few additional scenario simulations are required to convert these findings into practical recommendations for policymakers as well as citizens. Finally, D7.2 generalised recommendations on PCSs implementation to improve air quality is expected to provide comprehensive guidelines incorporating this report. The further scenarios optimizing the PCS dimensions are required to improve the implementation of these measures in space constrained built up environment. Additional investigations assessing seasonal variability of PCS performance in abating is required and these are beyond scope of our studies.

4.1 Bologna

A very detailed CFD analysis has been applied to some areas of Bologna. For two zones, one around the street canyon without trees (Marconi street) and one characterized by the presence of many trees have been considered. For both the regions, two whole day cycles have been simulated, one in summer (from 22/08/2017 UTC 10:00 to 23/08/2017 UTC 10:00) and one in winter (from 08/02/2018 UTC 10:00 to 09/02/2018 UTC 10:00). The numerical results have been compared with experiments, made in the two street canyons during the two day-cycles, showing a very good agreement for some flow configurations.

The results show highly non-uniform in space pollutant concentrations distributions, especially near the intersections, within street canyons without trees. On the contrary, the pollutant distribution is more uniform in the case of street canyons with trees, but pollutant concentration levels could be higher than expected in some zones, even upstream the street canyon. Different scenarios have been considered, in order to understand if a certain tree distribution could be extended to zones traditionally without trees, as Marconi street. The results show that planting trees within street canyons like Marconi street, characterized by aspect ratio greater than 1 and traffic intersections, would change the mixing and the local concentration levels within the street, giving more uniform distribution and lower levels of pollutant concentration peaks. Finally, the application of green roofs and green façades modifies the flow field at street level and the pollutant near the building walls.

4.2 Guildford

Flow field analysis revealed the impact of GI on wind flow as well as the pollutant dispersion in open road conditions. The wind velocity vectors and the cross-sectional contours displayed the wind flow modifications developed by the hedge row. The hedges along the street channelled the wind flow along the road increasing wind speed in the center at the breathing level (1-2 meters) forcing pollutants to move along the road. This barrier effect prevented pollutants to reach behind the hedge and experimental results reported similar observations. Further analysis of wind flow conditions and pollutant concentration changes will be carried out to perform scenario analysis investigating the influence of physical properties of GIs on air quality. The finding of this ongoing study will be reported in the D7.2 as generalized recommendations on planting and placing GIs in open-road environments.

4.3 Dublin

The Pearse Street modelling investigation developed a calibrated CFD model of a real street canyon in Dublin city centre and effectively assessed the potential of passive control in a real time environment. The following conclusions summarise the findings of the results and discussion sections of the Pearse Street model.

Calibration data was collected from several sources to validate each data set prior to the model calibration process. The calibration of the CFD model was carried out using geometrical data for Pearse Street, measurement of NO_x concentration in the street, traffic counts and meteorological data. A detailed analysis was carried out for the calibration data to ensure each data set was independently validated. The CFD model was calibrated in two steps (i) wind speed and direction and (ii) NO emission dispersion.

A semi-empirical equation was developed to calibrate the CFD model for the second calibration step. The equation took into account the complexities and variability in traffic and meteorological conditions, which the CFD model simplified for the purpose of investigating the potential of the passive controls in the street canyon. The semi-empirical equation was used to calibrate the model for three different wind directions; the predominant wind direction (~300°), parallel (~286°) and perpendicular (196°) winds.

The Pearse Street model introduced a footpath LBWs model as a passive control structure. Effect of the passive control structure were investigated to identify the different percentage reductions and increases in pollutant concentrations on the footpaths. The study provided evidence that passive controls influence air flow and pollutant dispersion in a real street canyon and the results compare well with the generic modelling investigations.

5 References / Bibliography

Abhijith, K.V. and Gokhale, S., 2015. Passive control potentials of trees and on-street parked cars in reduction of air pollution exposure in urban street canyons. Environmental Pollution, 204, 99-108.

Abhijith, K.V., Kumar, P., Gallagher, J., McNabola, A., Baldauf, R., Pilla, F., Broderick, B., Di Sabatino, S. and Pulvirenti, B., 2017. Air pollution abatement performances of green infrastructure in open road and built-up street canyon environments–A review. Atmospheric Environment, 162, 71-86.

Abhijith, K.V. and Kumar, P., 2019. Field investigations for evaluating green infrastructure effects on air quality in open-road conditions. Atmospheric Environment, 201, 132-147.

Al-Dabbous, A.N. and Kumar, P., 2014. The influence of roadside vegetation barriers on airborne nanoparticles and pedestrians exposure under varying wind conditions. Atmospheric Environment, 90, 113-124.

Amorim, J.H., Rodrigues, V., Tavares, R., Valente, J. and Borrego, C., 2013. CFD modelling of the aerodynamic effect of trees on urban air pollution dispersion. Science of the Total Environment, 461, 541-551.

Baker, J., Walker, H. L. & Cai, X. (2004). A study of the dispersion and transport of reactive pollutants in and above street canyons--a large eddy simulation. Atmospheric Environment, 38, 6883-6892.

Balczó, M., Gromke, C. and Ruck, B., 2009. Numerical modeling of flow and pollutant dispersion in street canyons with tree planting. Meteorologische Zeitschrift, 18(2), 197-206.

Baldauf, R., 2016. Recommendations for Constructing Roadside Vegetation Barriers to Improve Near-Road Air Quality. National Risk Management Laboratory Office of Research and Development, Air Pollution Prevention and Control Division: Washington, DC, USA.

Broderick, B., Budd, U., Misstear, B., Jennings, G. & Ceburnis, D. (2006). Air Pollution – Validation of Air Pollution Dispersion Modelling for the Road Transport Sector under Irish Conditions. Environmental RTDI Programme 2000–2006. Wexford: Environmental Protection Agency.

Buccolieri, R., Gromke, C., Di Sabatino, S. and Ruck, B., 2009. Aerodynamic effects of trees on pollutant concentration in street canyons. Science of the Total Environment, 407(19), 5247-5256.

Buccolieri, R., Sandberg, M., Di Sabatino, S. 2010. City breathability and its link to pollutant concentration distribution within urban-like geometries. Atmospheric Environment 44, 1894-1903.

Buccolieri, R., Salim, S.M., Leo, L.S., Di Sabatino, S., Chan, A., Ielpo, P., de Gennaro, G. and Gromke, C., 2011. Analysis of local scale tree–atmosphere interaction on pollutant concentration in idealized street canyons and application to a real urban junction. Atmospheric Environment, 45(9), 1702-1713.

Buccolieri, R., Santiago, J.L., Rivas, E. and Sáanchez, B., 2018. Reprint of: Review on urban tree modelling in CFD simulations: Aerodynamic, deposition and thermal effects. Urban Forestry & Urban Greening, 31, 212-220.

Carslaw, D. C. (2005). Evidence of an increasing NO_2/NO_X emissions ratio from road traffic emissions. Atmospheric Environment, 39, 4793-4802.

Carslaw, D. C. & Beevers, S. D. (2005). Estimations of road vehicle primary NO_2 exhaust emission fractions using monitoring data in London. Atmospheric Environment, 39, 167-177.

COST. Year. Quality Assurance of Microscale Meteorological Models. In: 732., C. A., ed., July 28/29 2005 Hamburg, Germany.: COST, 141.

Council of the European Communities (CEC) (1999). Directive 1999/30/EC of 22 April 1999 relating to limit values for sulphur dioxide, nitrogen dioxide and oxides of nitrogen, particulate matter and lead in ambient air. O.J. L163, 29 June 1999.

Crowther, J. M. & Hassan, A. G. A. A. (2002). Three-Dimensional Numerical Simulation of Air Pollutant Dispersion in Street Canyons. Water, Air, & Soil Pollution: Focus, 2, 279-295.

Department for Environment Food and Rural Affairs (2007). The Air Quality Strategy for England, Scotland, Wales and Northern Ireland. In: DEPARTMENT FOR ENVIRONMENT FOOD AND RURAL AFFAIRS (ed.). Norwich: The Stationary Office.

De Paul, F. T. & Sheih, C. M. (1986). Measurements of Wind Velocities in a Street Canyon. Atmospheric Environment (1967), 20, 455-459.

Di Sabatino, S., Buccolieri, R., Pulvirenti, B. and Britter, R., 2007. Simulations of pollutant dispersion within idealised urban-type geometries with CFD and integral models. Atmospheric Environment, 41(37), 8316-8329.

Di Sabatino, S., Buccolieri, R. and Salizzoni, P., 2013. Recent advancements in numerical modelling of flow and dispersion in urban areas: a short review. International Journal of Environment and Pollution 7, 52(3-4), 172-191.

Di Sabatino, S., Buccolieri, R., Pappaccogli, G. and Leo, L.S., 2015. The effects of trees on micrometeorology in a real street canyon: consequences for local air quality. International Journal of Environment and Pollution 58, 100-111.

EEA (European Environment Agency), 2017. EMEP/EEA air pollutant emission inventory guidebook 2016. Last update June 2017.

Hofman, J., Bartholomeus, H., Janssen, S., Calders, K., Wuyts, K., Van Wittenberghe, S. and Samson, R., 2016. Influence of tree crown characteristics on the local PM10 distribution inside an urban street canyon in Antwerp (Belgium): A model and experimental approach. Urban Forestry & Urban Greening, 20, 265-276.

Franke, J., Hellsten, A., Schlünzen, H. and Carissimo, B., 2007. Best practice guideline for the CFD simulation of flows in the urban environment. COST action 732. Quality Assurance and Improvement of Meteorological Models. University of Hamburg, Meteorological Institute, Center of Marine and Atmospheric Sciences.

Gallagher, J., Gill, L.W. and McNabola, A., 2011. Optimizing the use of on-street car parking system as a passive control of air pollution exposure in street canyons by large eddy simulation. Atmospheric Environment, 45(9), 1684-1694.

Gallagher, J., Gill, L.W. and McNabola, A., 2012. Numerical modelling of the passive control of air pollution in asymmetrical urban street canyons using refined mesh discretization schemes. Building and Environment, 56, 232-240.

Gallagher, J. (2013a). An Investigation of the Passive Control of Air Pollution in the Urban Environment (Doctoral dissertation, Trinity College Dublin).

Gallagher, J., Gill, L.W. & McNabola, A. (2013b). The passive control of air pollution exposure in Dublin, Ireland: A combined measurement and modelling case study. Science of the Total Environment, 458, 331-343.

Gallagher, J., Baldauf, R., Fuller, C.H., Kumar, P., Gill, L.W. and McNabola, A., 2015. Passive methods for improving air quality in the built environment: a review of porous and solid barriers. Atmospheric Environment, 120, 61-70.

Gallagher, J. and Lago, C., 2019. How parked cars affect pollutant dispersion at street level in an urban street canyon? A CFD modelling exercise assessing geometrical detailing and pollutant decay rates. Science of the Total Environment, 651, 2410-2418.

Gao, Z., Bresson, R., Qu, Y., Milliez, M., de Munck, C. and Carissimo, B., 2018. High resolution unsteady RANS simulation of wind, thermal effects and pollution dispersion for studying urban renewal scenarios in a neighborhood of Toulouse. Urban Climate, 23, 114-130.

Garcia, J., Cerdeira, R., Tavares, N., Coelho, L.M.R., Kumar, P. and Carvalho, M.G., 2013. Influence of virtual changes in building configurations of a real street canyon on the dispersion of PM10. Urban Climate, 5, 68-81.

Ghenu, A., Rosant, J. M. & Sini, J. F. (2008). Dispersion of pollutants and estimation of emissions in a street canyon in Rouen, France. Environmental Modelling & Software, 23, 314-321.

Goel, A., Kumar, P., (2014). A review of fundamental drivers governing the emissions, dispersion and exposure to vehicle-emitted nanoparticles at signalised traffic intersections. Atmospheric Environment, 97, 316-331.

Gromke, C., Buccolieri, R., Di Sabatino, S. and Ruck, B., 2008. Dispersion study in a street canyon with tree planting by means of wind tunnel and numerical investigations–evaluation of CFD data with experimental data. Atmospheric Environment, 42(37), 8640-8650.

Gromke, C. and Ruck, B., 2009. On the impact of trees on dispersion processes of traffic emissions in street canyons. Boundary-Layer Meteorology, 131(1), 19-34.

Gromke, C. and Ruck, B., 2012. Pollutant concentrations in street canyons of different aspect ratio with avenues of trees for various wind directions. Boundary-Layer Meteorology, 144(1), 41-64.

Gromke, C., Blocken, B., Janssen, W., Merema, B., van Hooff, T. and Timmermans, H., 2015. CFD analysis of transpirational cooling by vegetation: Case study for specific meteorological conditions during a heat wave in Arnhem, Netherlands. Building and Environment, 83, 11-26.

Gromke, C., Jamarkattel, N. and Ruck, B., 2016. Influence of roadside hedgerows on air quality in urban street canyons. Atmospheric Environment, 139, 75-86.

Gualiteri, G. & Tartaglia, M. (1997). A street canyon model for estimating NOx concentrations due to road traffic. International conference on measurements and modelling in environmental pollution. Madrid: Computational Mechanics Publications, Southampton, ROYAUME-UNI.

Hoydysh, W. G. & Dabberdt, W. F. (1988). Kinematics and dispersion characteristics of flows in asymmetric street canyons. Atmospheric Environment (1967), 22, 2677-2689.

Huang, H., Ooka, R., Chen, H., Kato, S., Takahashi, T. & Watanabe, T. (2008). CFD analysis on traffic-induced air pollutant dispersion under non-isothermal condition in a complex urban area in winter. Journal of Wind Engineering and Industrial Aerodynamics, 96, 1774-1788.

Janhäll, S., 2015. Review on urban vegetation and particle air pollution–Deposition and dispersion. Atmospheric Environment, 105, 130-137.

Jeanjean, A.P., Monks, P.S. and Leigh, R.J., 2016. Modelling the effectiveness of urban trees and grass on PM2.5 reduction via dispersion and deposition at a city scale. Atmospheric Environment, 147, 1-10.

Jeanjean, A.P., Buccolieri, R., Eddy, J., Monks, P.S. and Leigh, R.J., 2017. Air quality affected by trees in real street canyons: The case of Marylebone neighbourhood in central London. Urban Forestry & Urban Greening, 22, 41-53.

Jensen, S. S., Larson, T., Deepti, K. C. & Kaufman, J. D. (2009). Modeling traffic air pollution in street canyons in New York City for intra-urban exposure assessment in the US Multi-Ethnic Study of atherosclerosis and air pollution. Atmospheric Environment, 43, 4544-4556.

Jicha, M., Pospisil, J. & Katolicky, J. (2000). Dispersion of Pollutants in Street Canyon under Traffic Induced Flow and Turbulence. Environmental Monitoring and Assessment, 65, 343-351.

Johnson, W. B., Ludwig, F. L., Dabberdt, W. F. & Allen, R. J. (1973). An Urban Diffusion Simulation Model for Carbon Monoxide. Journal of the Air Pollution Control Association, 23, 480-498.

Kelly, F. H., Anderson, R., Armstrong, B., Atkinson, R., Barratt, B., Beevers, S., Derwent, D., Green, D., Mudway, I. & Wilkinson, P. (2011). The Impact of the Congestion Charging Scheme on Air Quality in London: Environmental Research Group, MRC-HPA Centre for Environment & Health.

Klingberg, J., Konarska, J., Lindberg, F. and Thorsson, S., 2015. Measured and modelled leaf area of urban woodlands, parks and trees in Gothenburg, Sweden. ICUC9, 9th International Conference on Urban Climate jointly with 12th Symposium on the Urban Environment, 1-6.

Kumar, P., Morawska, L., Birmili, W., Paasonen, P., Hu, M., Kulmala, M., Harrison, R.M., Norford, L. and Britter, R., 2014. Ultrafine particles in cities. Environment International, 66, 1-10.

Kumar, P., Morawska, L., Martani, C., Biskos, G., Neophytou, M., Di Sabatino, S., Bell, M., Norford, L. and Britter, R., 2015. The rise of low-cost sensing for managing air pollution in cities. Environment International, 75, 199-205.

Li, J.F., Zhan, J.M., Li, Y.S. and Wai, O.W., 2013. CO2 absorption/emission and aerodynamic effects of trees on the concentrations in a street canyon in Guangzhou, China. Environmental pollution, 177,4-12.

Liu, Y. S., Cui, G. X., Wang, Z. S. & Zhang, Z. S. (2011). Large eddy simulation of wind field and pollutant dispersion in downtown Macao. Atmospheric Environment, 45, 2849-2859.

McNabola, A., Broderick, B.M. and Gill, L.W., 2009. A numerical investigation of the impact of low boundary walls on pedestrian exposure to air pollutants in urban street canyons. Science of the Total Environment, 407(2), 760-769.

McNabola, A., 2010. New Directions: Passive control of personal air pollution exposure from traffic emissions in urban street canyons. Atmospheric Environment, 24(44), 2940-2941.

Moradpour, M., Afshin, H. and Farhanieh, B., 2017. A numerical investigation of reactive air pollutant dispersion in urban street canyons with tree planting. Atmospheric Pollution Research, 8(2), 253-266.

Murena, F., Favale, G., Vardoulakis, S. & Solazzo, E. (2009). Modelling dispersion of traffic pollution in a deep street canyon: Application of CFD and operational models. Atmospheric Environment, 43, 2303-2311.

NAEI (2009). UK Emission Factor Databases. National Atmospheric Emissions Inventory. National Roads Authority (2010). ITS (Intelligent Transport Systems). In: AUTHORITY, T. N. R. (ed.).

Oke, T. R. (1988). Street design and urban canopy layer climate. Energy and Buildings, 11, 103-113.

Oke, T. R. (2006). Initial Guidance to Obtain Representative Meteorological Observation at Urban Sites. Instruments and Observing Methods Report No.81. World Meteorological Organization.

Parra, M. A., Santiago, J. L., Martín, F., Martilli, A. & Santamaría, J. M. (2010). A methodology to urban air quality assessment during large time periods of winter using computational fluid dynamic models. Atmospheric Environment, 44, 2089-2097.

Prandini, F., B. Pulvirenti, S. Di Sabatino, F. Barbano, E. Brattich, A. Drebs, P. Kumar, K. Jylhä, E. Minguzzi, M. Nardino, F. Pilla, L. Torreggiani, The effect of trees in temperature hotspots within a urban heat island: CFD analysis of the Bologna case study, AMS Conference, 8-10 January 2018, Austin, US.

Richards, P.J. and Hoxey, R.P., 1993. Appropriate boundary conditions for computational wind engineering models using the k-ε turbulence model. In Computational Wind Engineering 1, 145-153.

Rushforth, K., Trees of Britain and Europe, Harper Collins.

Sanchez, B., Santiago, J.L., Martilli, A., Martin, F., Borge, R., Quaassdorff, C. and de la Paz, D., 2017. Modelling NOx concentrations through CFD-RANS in an urban hot-spot using high resolution traffic emissions and meteorology from a mesoscale model. Atmospheric Environment, 163, 155-165.

Salim, S.M., Cheah, S.C. and Chan, A., 2011. Numerical simulation of dispersion in urban street canyons with avenue-like tree plantings: comparison between RANS and LES. Building and Environment, 46(9), 1735-1746.

Salim, S.M., Buccolieri, R., Chan, A., Di Sabatino, S. and Cheah, S.C., 2011b. Large eddy simulation of the aerodynamic effects of trees on pollutant concentrations in street canyons. Procedia Environmental Sciences, 4, 17-24.

Santese, F., Buccolieri, R., Di Sabatino, S. & Britter, R. (2007). CFD Simulations for the Study of Thermal Effects of Flow and Pollutant Dispersion in Urban Geometries. 11th International Conference on Harmonisation within Atmospheric Dispersion Modelling for Regulatory Purposes. Cambridge, UK.

Santiago, J.L., Borge, R., Martin, F., de la Paz, D., Martilli, A., Lumbreras, J. and Sanchez, B., 2017. Evaluation of a CFD-based approach to estimate pollutant distribution within a real urban canopy by means of passive samplers. Science of the Total Environment, 576, 46-58.

Solazzo, E., Cai, X. & Vardoulakis, S. (2008). Modelling wind flow and vehicle-induced turbulence in urban streets. Atmospheric Environment, 42, 4918-4931.

Solazzo, E., Cai, X. & Vardoulakis, S. (2009). Improved parameterisation for the numerical modelling of air pollution within an urban street canyon. Environmental Modelling & Software, 24, 381-388.

Surrey-i, 2015. Census key statistics (Key demographics, age, gender, ethnicity, religion, disability, health and carers), Guildford Local Authority in Surrey 25–27.

Tominaga, Y., Mochida, A., Yoshie, R., Kataoka, H., Nozu, T., Yoshikawa, M. and Shirasawa, T., 2008. AIJ guidelines for practical applications of CFD to pedestrian wind environment around buildings. Journal of Wind Engineering and Industrial Aerodynamics, 96(10-11), 1749-1761.

Wang, L., Pan, Q., Zheng, X.P. and Yang, S.S., 2017. Effects of low boundary walls under dynamic inflow on flow field and pollutant dispersion in an idealized street canyon. Atmospheric Pollution Research, 8(3), 564-575.

Wania, A., Bruse, M., Blond, N. and Weber, C., 2012. Analysing the influence of different street vegetation on traffic-induced particle dispersion using microscale simulations. Journal of Environmental Management, 94(1), 91-101.

Wehner, B., Birmili, W., Gnauk, T. & Wiedensohler, A. (2002). Particle number size distributions in a street canyon and their transformation into the urban-air background: measurements and a simple model study. Atmospheric Environment, 36, 2215-2223.

Xue, F. and Li, X., 2017. The impact of roadside trees on traffic released PM10 in urban street canyon: Aerodynamic and deposition effects. Sustainable Cities and Society, 30, 195-204.

Zhang, K., Batterman, S. & Dion, F. (2011). Vehicle emissions in congestion: Comparison of work zone, rush hour and free-flow conditions. Atmospheric Environment, 45, 1929-1939.

Zhou, X.H., Brandle, J.R., Takle, E.S. and Mize, C.W., 2002. Estimation of the three-dimensional aerodynamic structure of a green ash shelterbelt. Agricultural and Forest Meteorology, 111(2), 93-108.